HUNGARIAN UNIVERSITY OF AGRICULTURE AND LIFE SCIENCES

Utilisation of organic Rankine cycle from various heat sources

DOI: 10.54598/006290

PhD Dissertation

by

Diki Ismail Permana

Gödöllő

2025

Doctoral school	
Science:	Mechanical Engineering
Leader:	Prof. Dr. Gábor Kalácska, DSc Institute of Technology Hungarian University of Agriculture and Life Science, Gödöllő, Hungary
Supervisor:	Prof. Dr. István Farkas, DSc Institute of Technology Hungarian University of Agriculture and Life Science, Gödöllő, Hungary
Co-Supervisor:	Dr. Dani Rusirawan Department of Mechanical Engineering Institut Teknologi Nasional Bandung, Bandung, Indonesia

…………………………………………	…………………………………………
Affirmation of supervisors	Affirmation of head of school

CONTENTS

NOMENCLATURE AND ABBREVIATION

A_{sc}	Acentric area (m^2)
C_p	Specific heat at pressure constant (J/kg.K)
C	coefficient
C_{ST}	Specific heat capacity of storage
e_x	Exergy specific (kJ/kg)
$\dot{E}_D$	Rate of exergy destruction (kW)
$\dot{E}_X$	Exergy rate (kW)
$\dot{E}X_{in}^{Q}$	Rate of exergy heat input (kW)
$\dot{E}X_{out}^{Q}$	Rate of exergy heat output (kW)
g	Gravitational acceleration (9.8 m/s^2)
G_b	Solar irradiance (W/m^2)
h	Specific enthalpy (kJ/kg)
h_s	Specific enthalpy at isentropic process (kJ/kg)
H	Head pump (m)
K_θ	Incident angle modifier
ln	Logarithm natural
$\dot{m}$	Mass flow rate (kg/s)
$\dot{m}_{cw}$	Mass flow rate of cooling water (kg/s)
$\dot{m}_{bio}$	Mass flow rate of biomass (kg/s)
N	Machine speed rotation (RPM)
N_{pump}	Pump speed rotation (RPM)
N_s	Specific rotational speed (RPM)
N_{exp}	Expander speed rotation (RPM)
P	Pressure (Pa)
P_{crit}	Critical pressure (MPa)
P_0	Pressure at dead state (MPa)
P_r	Prandtl number
P_{reg}	Regenerator pressure (MPa)
$\dot{Q}$	Heat rate (W)
R	Universal gas constant (8.3154 J/mol.K)
R_e	Reynold number
s	Specific entropy (kJ/kg.K)
$\dot{S}_{gen}$	Rate of entropy generation

T	Temperature (°C)
T_0	Temperature at dead state (°C)
T_{crit}	Critical temperature (°C)
$T_{c,i}$	Cooling inlet temperature (°C)
$T_{c,o}$	Cooling outlet temperature (°C)
$T_{h,i}$	Heat-source inlet temperature (°C)
$T_{h,o}$	Heat-source outlet temperature (°C)
T_{melt}	Melting temperature (°C)
T_{reg}	Regenerator temperature (°C)
T_{TES}	TES temperature (°C)
T_w	Temperature of cooling water (°C)
$\dot{V}$	Volumetric flow rate (m^3/s)
$\dot{W}_{avg}$	Average daily power of the system (W)
$\dot{W}_{pump}$	Pump power (W)
$\dot{W}_{pw}$	Power of cooling water pump (W)
$\dot{W}_{pwt}$	Power of cooling water pump theoretical (W)
$\dot{W}_{exp}$	Power of Expander (W)
$\dot{W}_{net}$	Net power (W)
z_e	Exit elevation (m)
z_i	Inlet elevation (m)

Greek symbols

β	Influence coefficient
Δ	Difference
€	Euro currency
γ	Specific weight (N/m^3)
μ	Population mean
η	Efficiency (%)
ψ	Exergy efficiency (%)
Σ	Summation
ζ	Dimensionless parameter
τ	Charging/discharging time
ρ	Density (kg/m^3)
ν	Degree thermodynamic perfection

Abbreviations

AI	Artificial intelligence
ANN	Artificial Neural Network
ASHRAE	American Society of Heating Refrigerating and Air Conditioning Engineers
CDS	Condenser
CHP	Combine heat and power
CSP	Concentrated solar power
COP	Coefficient of performance
CV	Control volume
DHW	Domestic hot water
DSC	Differential scanning calorimetry
DVG	Direct vapor generation
EEF	Environmental effect factor
EFB	Empty fruit bunches
EFPC	Evacuated flat-plate collector
ESI	Exergy sustainability indicator
ETC	Evacuated tube collector
EU	European Union
EVA	Evaporator
EWR	Exergy waste ratio
GA	Genetic algorithms
GSI	Global solar irradiation
GPP	Geothermal power-plant
GTR	Generator
GWP	Global warming potential
HE	Heat exchanger
HHV	High Heating Value
HTF	Heat transfer fluid
HVAC	Heating Ventilating and Air Conditioning Engineers
IAM	Incident angle modifier
IC	Internal combustion
IHE	Internal heat exchanger
LCOE	Levelized Cost of Electricity
LEL	Lower explosive limit
LFC	Linear Fresnel collectors

LHV	Low Heating Value
LM	Levenberg-Marguardt
LMTD	Log mean temperature difference
MED	Multi effect desalination
MRE	Mean relative error
MSE	Mean squared error
NGL	Napier grass leaves
NGS	Napier grass stems
NGT	Napier grass steams-leaves
NIST	National of institute standard and technology
NPV	Net Present Value
ODP	Ozone depleting potential
ORC	Organic Rankine Cycle
PCM	Phase Change Material
PEC	Purchase equipment cost
PSO	Particle swarm optimization
PTC	Parabolic tube collector
PV	Photovoltaic
WHR	Waste heat recovery
SCO2	Supercritical Carbon dioxide
SIC	Specific Investment Cost
SPB	Simple Payback Period
SRC	Solar Rankine Cycle
TCI	Total capital investment
TES	Thermal energy storage
TSI	Thermo sustainability index
UEL	Upper explosive limit

1. INTRODUCTION

This chapter presents the background and the importance of the study as well as the objectives of the research.

1.1. Introduction

Renewable Energy sources are the key to reducing fossil fuel usage to generate electricity. Renewable energy like solar thermal, geothermal, biomass, and waste heat sources from industries are capable of decreasing the rate of the consumption of fossil fuels and reducing the effect that brings harm to the environment. In addition, these residual moderate or low-medium temperature heat sources cannot be efficiently converted into electricity through the conventional Steam Rankine Cycle (SRC). So, it is necessary to study another type of process, such as the Organic Rankine Cycle (ORC) that has been considered as the most feasible cycle to generating electricity while recovering various heat sources as proposed by many authors (Anastasovski et al., 2020; Lecompte et al., 2015; Diki I. Permana et al., 2023; Permana et al., 2023). ORC utilizes steam heat such as the conventional Rankine cycle but uses a low-set temperature of organic fluids rather than water. The leverages of ORC system are lower temperature and pressure of turbine inlet, more significant condensing pressure, and no deaerator, robust and environmentally safe (Quoilin et al., 2013). The main disadvantages of the ORC system are separate precaution to prevent the leakage, contamination of organic fluid and having a lower efficiency compared to SRC (Wang et al., 2019). Despite, ORC is capable of producing electricity at a low-set temperature. However, it needs another heat resource from another system.

There is a lot of heat resource that can be combined with ORC such as geothermal excess steam (Permana et al., 2021), waste heat (Somogyi et al., 2018), solid biomass (Malico et al., 2019) and from solar thermal (Permana et al., 2024). Fig. 1.1 illustrates the historical trend of installed power (Fig. 1.1a) and the number of installed plants (Fig. 1.1b) since 1975, categorized by application. Notably, installed capacity remained relatively low (below 100 MW) until 2008, after which it surged, peaking near 400 MW in 2015 before stabilizing around 300 MW. The significant increase in ORC capacity is primarily driven by geothermal applications, followed by biomass particularly in Europe between 2000 and 2012 and more recently by waste heat recovery (WHR).

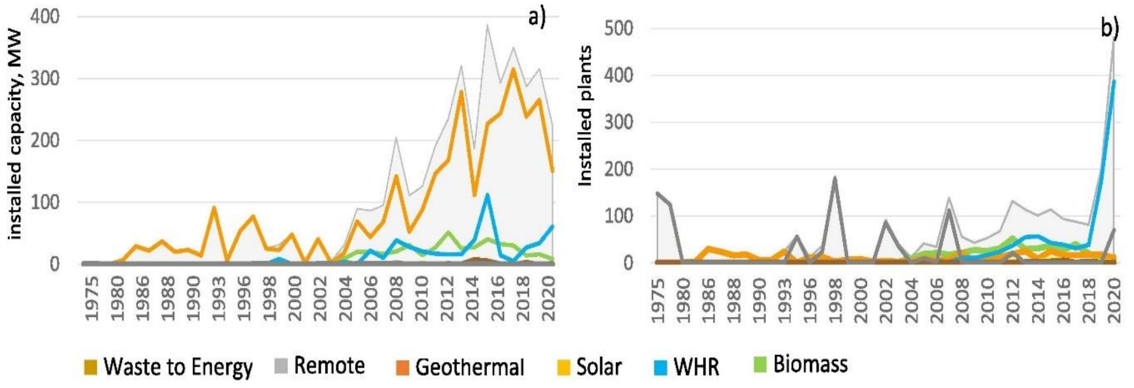

Fig. 1.1. Historical trend of ORC: a) installed capacity, b) installed plants (Wieland et al., 2023)

Fig. 1.2 presents the geographical distribution of ORC plants. The Middle East and North America lead in installed capacity due to extensive geothermal energy utilization, followed by Europe, where biomass is the dominant technology. However, Europe ranks first in the number of installed plants, as both biomass and WHR systems typically use smaller power plants (1 to 5 MW). Russia, in second place, has numerous small ORC plants along gas pipelines but a low total installed capacity. Geothermal energy is primarily used in Turkey and the USA, while biomass plants are concentrated in Europe, especially in Germany and Italy, due to favourable incentives. WHR applications are more globally distributed since they are linked to industrial processes rather than specific natural energy sources. Meanwhile, anomalies can be seen in the ASEAN region, where solar-ORC should dominate because it is located on the equator, which has a longer duration of solar heat for more than a year and is stagnant; in fact, it is very little in Indonesia, which has high geothermal and solar for ORC potential, but ORC heat utilization is still very low. Namely, around 300 MW of power and less than 20 plants have been installed. So that this report can be used as a concern for further ORC research and development at the government level.

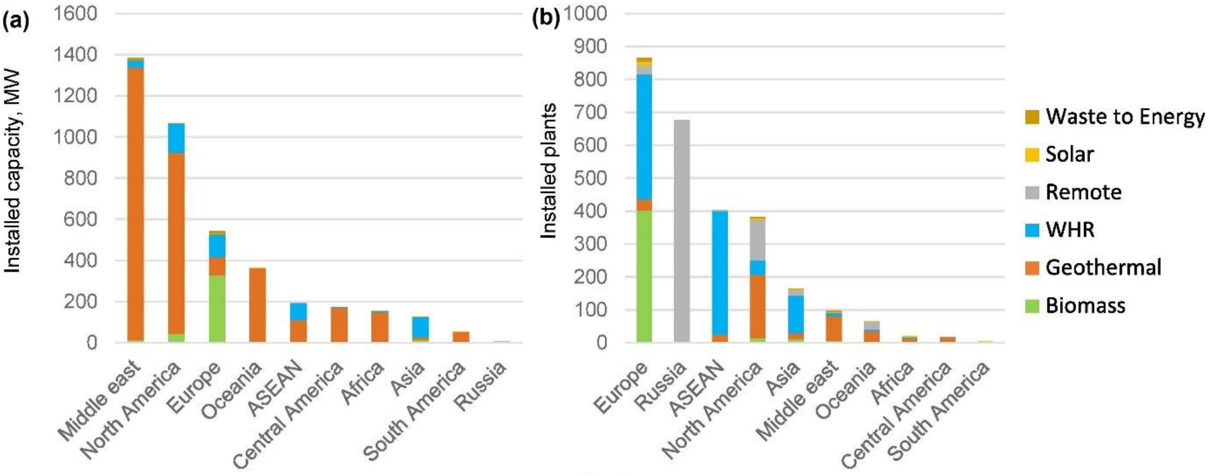

Fig. 1.2. ORC application in different macro-region worldwide: a) installed capacity, b) installed plants (Wieland et al., 2023)

Geothermal energy possesses vast global potential (Limberger et al., 2018) and ORC systems are the most widely used technology for power generation from geothermal heat sources with temperatures below 180 °C (Zarrouk and Moon, 2014). ORC technology is particularly effective for harnessing low- to medium-enthalpy, liquid-dominated geothermal heat sources or as a bottoming cycle for high-enthalpy sources. Efforts to optimize thermodynamic plant configurations and working fluids for various geothermal conditions, with the aim of improving economic performance, have a long history in both academia and industry. Subcritical ORC systems are the most commonly used in commercial large-scale geothermal applications. Two-stage ORC systems are also prevalent, as they allow for a better temperature match between the heat source and the ORC, leading to more efficient heat utilization (Braimakis and Karellas, 2018). Thermodynamically, supercritical ORC systems are often preferred due to their superior alignment with the temperature profiles of geothermal brine and the ORC system (Song et al., 2020). However, the high pressure levels required in supercritical ORC systems increase material stress, which can significantly impact investment costs. Several researches have been conducted on geothermal energy as a low-temperature heat source for ORC's from the perspective conventional energy and exergy analysis. Heberle and Brüggemann, (2010) reported an exergy analysis for working fluid selection in an ORC geothermal. They draw conclusion, working fluid with lower critical temperature, such as Isobutane and R227ea and Isobutane are more preferable for ORC power generation.

Solar is the primary source of renewable energy that sustains our earth. Around the 1.75×10^5 TW, and that is the entire solar energy received by the earth continuously and it has been weakened twice by both atmosphere (16% absorption, 6% reflection) and clouds (3% absorption, 20% reflection) (Goswami, 2022). Solar Thermal is one of many heat sources that can support ORC system. The advantage of using solar thermal as a heat source when combine with ORC system, it can provide affordable energy supplies in remote areas and is suitable in disaster territory. Despite the challenges, research on solar ORC systems continues to garner strong interest from both academia and industry (Loni et al., 2021). One key feature of solar ORC systems is the intermittency of the heat source due to fluctuating sunlight. To ensure reliable power generation, a thermal energy storage (TES) system can be incorporated. The type of storage used depends on the preferred temperature range, with options including sensible heat storage (Yu et al., 2021) or latent heat storage (Alvi et al., 2020).

Biomass accounts for 14% of the world's primary energy demand, and in some developing nations, this figure reaches up to 90% (Dong et al., 2009). Unlike other renewable sources such as wind and solar, which are influenced by changing weather conditions, biomass offers a reliable option for base-load heat and power generation. As a result, biomass could potentially replace a portion of the power generation traditionally supplied by fossil fuels like coal, natural gas, or oil in a renewable energy system. The environmental impact of biomass utilization is significantly influenced by the transportation distance to the power plant (Liu et al., 2017). As a result, biomass-fuelled power plants are typically most viable in medium- to small-scale and decentralized applications. In these cases, steam turbine cycles are often not cost-effective, but ORC provide an efficient alternative (Macchi and Astolfi, 2016.) particularly in combined heat and power (CHP) systems (Dong et al., 2009). These small-scale CHP systems are usually operated in heat-driven mode, which causes the ORC unit to frequently operate at partial load, similar to ORC units in waste heat recovery systems.

1.2. Objectives

The growing demand for sustainable energy sources has propelled interest in low- and medium-temperature power generation technologies, particularly for geothermal, biomass, and solar energy applications. ORC systems, known for their flexibility in harnessing low-grade heat, have emerged as a promising solution to convert renewable resources into electrical power efficiently. This research focuses on optimizing ORC systems by leveraging diverse energy source (geothermal, biomass, and solar) under varying environmental and geographical conditions. By conducting detailed energy, exergy, environmental, and economic analyses (4E), this study aims to address the unique challenges of each renewable source, thereby enhancing system performance and viability. The specific objectives of this research include:

- To analyse the working fluids that are suitable for use in ORC utilisation that use various heat sources (geothermal, biomass and solar) and temperatures based on suitable and environmentally friendly working fluids properties.

- To analyse the potential of geothermal energy from geothermal waste heat is carried out using simulations based on energy, exergy and environmental conditions with low-medium temperatures using Tura geothermal power-plant (GPP) data.
- To investigate biomass-ORC systems using a thermoeconomic approach for Indonesia with Napier grass as biomass feedstock, and to conduct a comprehensive 4E analysis (energy, exergy, environmental, and economic) on an existing biomass-ORC system in Italy, using wood waste as a biomass resource.
- To simulate solar-ORC systems in Hungary and Indonesia, considering the contrasting global solar irradiation potentials. This objective includes determining the optimal TES sizing and material selection to address solar energy's intermittent nature and limitations in providing continuous power throughout the day.
- To evaluate the performance of a 2 kW ORC test rig in Italy. Additionally, to carry out prediction and optimization analyses using artificial neural networks (ANN) to improve the system's efficiency and operational capabilities.

2. LITERATURE REVIEW

This chapter provides an overview of various types of solar collector, working fluids selection in ORC, and highlights their performance. Additionally, the literature review provides the various case studies sourced from journals the author has published is explained in detail. Some of them are the biomass-ORC thermodynamic modelling in Indonesia and Italy, the utilization of geothermal waste heat in Tura, and the utilization of solar heat in Indonesia and Hungary with the integration of TES. Furthermore, the literature provides the usage of ANN on experimental results and optimizing ORC performance.

2.1. The fundamental of organic Rankine cycle

The ORC differs from the classic Rankine cycle in using an organic component rather than water as the working fluid. This organic chemical is often a refrigerant, a hydrocarbon (e.g., butane, pentane, and hexane), a silicon oil, or a perfluorocarbon. Its boiling point is lower than water's, allowing heat recovery at a lower temperature than in the classic steam Rankine cycle. Its thermo-physical properties differ from waters in various ways (as detailed in section 3), with practical implications for the design of the ORC.

ORCs have been researched theoretically and practically studied since the 1980s, with reported efficiencies typically less than 10% for small-scale systems. Experimental experiments often used vane expanders and high Ozone Depleting Potential (ODP) refrigerants like R11 or R13. The first commercial applications occurred in the late 1980s and 1990s, with medium-scale power plants designed for geothermal and solar applications (Quoilin, 2011). Today, more than 200 ORC power plants have been found, with over 1800 MWe installed, and this trend is expanding faster than ever before. Most plants are installed for biomass CHP applications, followed by geothermal plants and WHR plants. However, geothermal is the first application for installed power (Enertime, 2011). ORC has a more straightforward layout than the steam Rankine cycle: there is no water-steam drum connected to the boiler, and the three evaporation steps (preheating, vaporisation, and superheating) can be performed using a single heat exchanger. The cycle architecture options are likewise more limited: reheating and turbine bleeding are generally inappropriate for the ORC cycle. However, a recuperator can be added as a recuperator between the pump outlet and the expander outlet, as shown in Fig. 2.1.

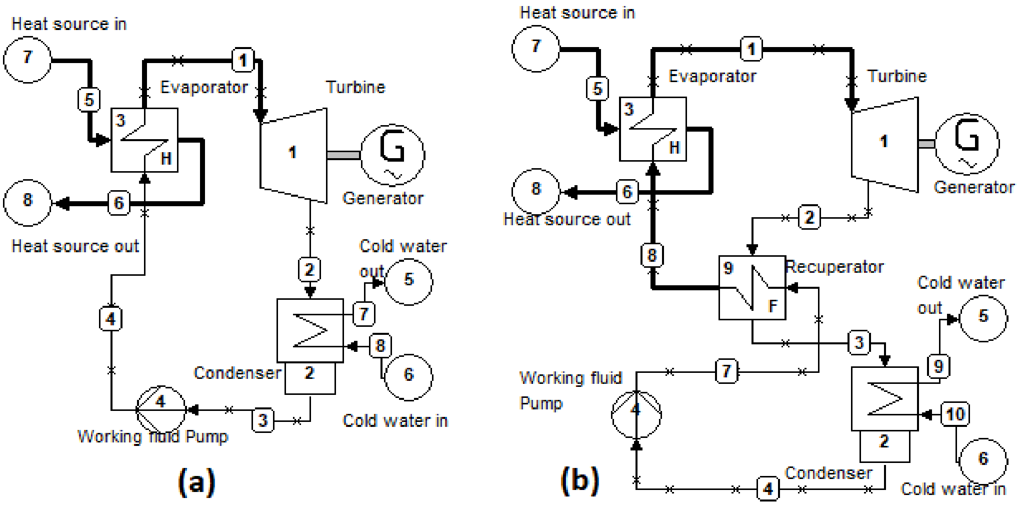

Fig. 2.1. The schematic of ORC: a) without recuperator, b) with recuperator

The basic cycle is similar to the traditional steam cycle: the organic working fluid is pumped, vaporised, expanded, and condensed. The cycle with the recuperator makes use of the leftover heat after expansion. This technique can reduce the heat required to vaporise the fluid in the evaporator.

2.1.1. Working fluids

In the Organic Rankine Cycle, the choice of working fluid will determine the phase diagram under operating conditions. The choice of working fluid also greatly influences the efficiency and costs incurred. Other influencing factors include:

- Turbine output discharge

The turbine output discharge determines the size and costs incurred for a system. Working fluids with low throughput ratios are preferred for economic reasons. The discharge in the system decreases as the temperature increases (Nouman, 2012). This is caused by changes in temperature, which results in changes in density. Therefore, the working fluid discharge in the turbine exit area will decrease.

- Mass flow rate

The enthalpy difference influences the mass flow rate in evaporation (Δh_{fg}). A large Δh_{fg} value will require a low mass flow rate to absorb the same heat in the evaporator.

- Pressure on the evaporator and condenser

In the Organic Rankine Cycle, the evaporator shows the maximum pressure of the working fluid of one cycle. On the other hand, the condenser shows the lowest pressure. The proper pressure in the working fluid ranges from 0.1-2.5 MPa with a pressure ratio of 3.5 (Tchanche et al., 2011).

- Environmental and security aspects

In this decade, the impact of a process on the environment is of particular concern. Organic working fluids, especially R23 refrigerant, can potentially damage the ozone layer and cause global warming, which can have long-term consequences. The ODP and global warming GWP values are indicators of how big the impact of the refrigerant substance as the working fluid. ODP is a relative value that shows the potential of a substance to damage ozone gas compared to the potential of chlorofluorocarbon-11 (CFC-11), which is given a reference value of 1. A substance with ODP = 2 means that the substance is twice as dangerous as CFC-11. GWP is a relative measure of how much heat greenhouse gases trap in the atmosphere. In this case, it compares the amount of heat trapped by a certain mass of a gas with the amount of heat trapped by the same carbon dioxide mass used as a standard with GWP = 1 (Coolset, 2023).

To determine the relationship between working fluid selection and operational safety, see the ASHRAE Refrigerant Safety Classification book, where the operational safety criteria for working fluids are divided into non-corrosive, non-flammable, and non-toxic. Fig. 2.2 shows ASHRAE safety classifications based on fire propagation rate and toxicity level. Fire propagation is divided into three classes: flammable, difficult to burn, and non-flammable, while toxic level is divided into two classes, namely low toxicity and high toxicity.

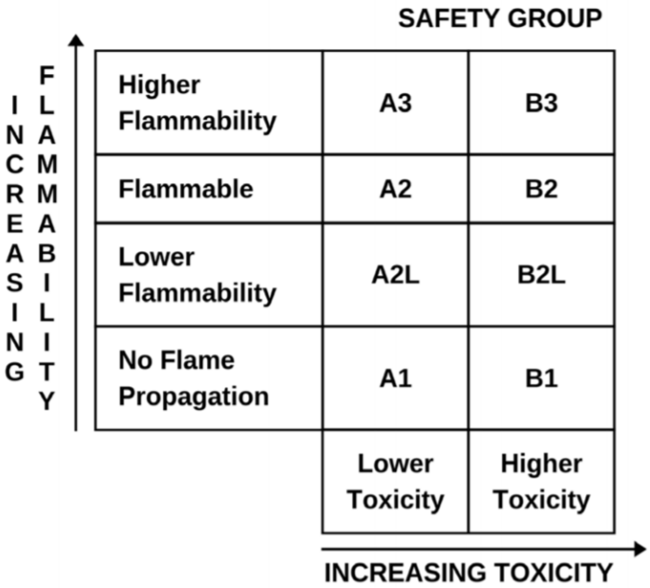

Higher Flammability	A3	B3
Flammable	A2	B2
Lower Flammability	A2L	B2L
No Flame Propagation	A1	B1
	Lower Toxicity	Higher Toxicity

Fig. 2.2. ASHRAE safety classification (ASHRAE, 2021)

Apart from that, selecting the type of working fluid must also consider its thermodynamic properties to suit the ORC application. Different from the characteristics of other thermodynamic cycles, such as the vapour compression refrigeration cycle and the Kalina cycle, the selection of working fluid in an ORC system is more complicated for the following reasons:

- The working conditions and types of heat sources from ORC are very broad, from low-temperature heat sources around 73 °C, such as geothermal and solar energy, to high-temperature heat sources of 500 °C, such as biomass (Lakew and Bolland, 2010). The greatest power for heat sources with temperatures of 80 – 160 °C, while R245fa produces the greatest power for heat sources at 160 °C. According to (Wang et al., 2013), the optimal selection of working fluid based on the temperature of the heat source is shown in Fig. 2.3.

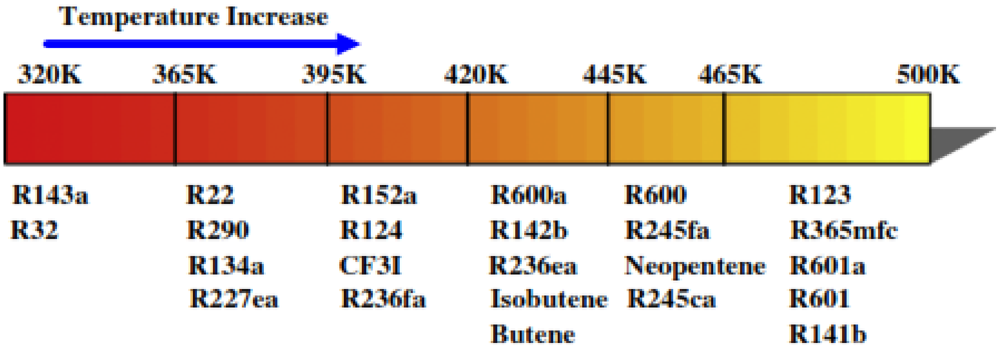

Fig. 2.3. Classification of working fluid based on operating temperature (Wang et al., 2013)

- for a few substances that have critical temperatures that are too high or too low, hundreds of substances can be used as candidates for ORC system working fluids, including hydrocarbons, ethers, perfluorocarbons, cfcs, alcohols, siloxane, and inorganics.

- Until now, no organic fluid has been identified as the most optimal working fluid for ORC applications; this is due to the large variety of working fluid candidates (Chen et al., 2010) researched 35 pure working fluids, finding that the recommended working fluid based on thermal efficiency and exergy analysis are R123, R600, R245fa, R245ca, and R600a.

Thermal stability and materials compatibility

Thermal stability and compatibility of the working fluid with materials and lubricants are critical factors for the efficiency and longevity of a GPP. The fluid must possess high thermal stability to ensure a long operational lifespan and cost-effective maintenance. Careful attention should be given to selecting a fluid, lubricant, and material combination that ensures the plant's durability over time. Although the lubricant can be either miscible or immiscible with the working fluid, a miscible lubricant is preferable to reduce system complexity. Chemical decomposition of the fluid not only diminishes plant efficiency but also necessitates fluid replacement and can generate non-condensable gases, which may have corrosive effects on system components. To evaluate fluid decomposition, two methods are commonly used: dynamic loop tests and static capsule tests. Table 2.1 provides data on the maximum stability temperatures for various fluids. Finally, Table 2.2 shows the detail of selected working fluids that will be used in this study.

Table 2.1. Working fluids classification based on suitable materials (Chen et al., 2010)

Working fluids	**MST (°C)**	**Materials**
R227ea	425	Stainless steel (AISI 316)
R23	400	Stainless steel (AISI 316)
R236fa	400	Stainless steel (AISI 316)
R143a	350	Stainless steel (AISI 316)
R245fa	300	Stainless steel (AISI 316)
R134a	368	Stainless steel
R141b	90	Stainless steel
R1311	102	Stainless steel
R7146	204	Stainless steel
R125	396	Stainless steel
Methanol	175-230	#
Toluene	400-425	#
R113	175-230	#

Table 2.2. The selected of working fluids in this research (Lemmon et al., 2013)

Working fluids	ρ_{crit} (kg/m^3)	T_{crit} (°C)	P_{crit} (MPa)	ODP	GWP	ASHRAE Class	Molar mass (g/mol)
R134a	511.9	101.06	4.0593	0	1300	A1	102.032
R410a	459.53	71.35	4.902	0	2088	A1	72.58
R22	523.842	96.14	4.99	0.04	1790	A1	86.47
R32	424	78.105	5.782	0	675	A2	52.024
Propane	220.478	96.74	4.251	0	3	A3	44.1
R245fa	519.436	154.01	3.651	0	1030	B1	134.04
R143a	431	72.71	3.77	0	n.a.	A2	84.04
R125	574.58	66.23	3.62	0	2740	A1	120.02
R123	550.004	154.01	3.662	0.012	76	B1	152.93

2.1.2. Expansion component

The performance of an ORC system is closely linked to the efficiency of the expander. The type of expander selected depends on the operating conditions and the system's size. There are two primary types of machines: turbo expanders and positive displacement expanders. Similar to refrigeration systems, positive displacement machines are more suitable for small-scale ORC units because they are designed for lower flow rates, higher pressure ratios, and significantly lower rotational speeds compared to turbo-machines (Persson and Sohlenius, 2008). Fig. 2.4 shows the different type of expander according to the heat sources and power can be produce.

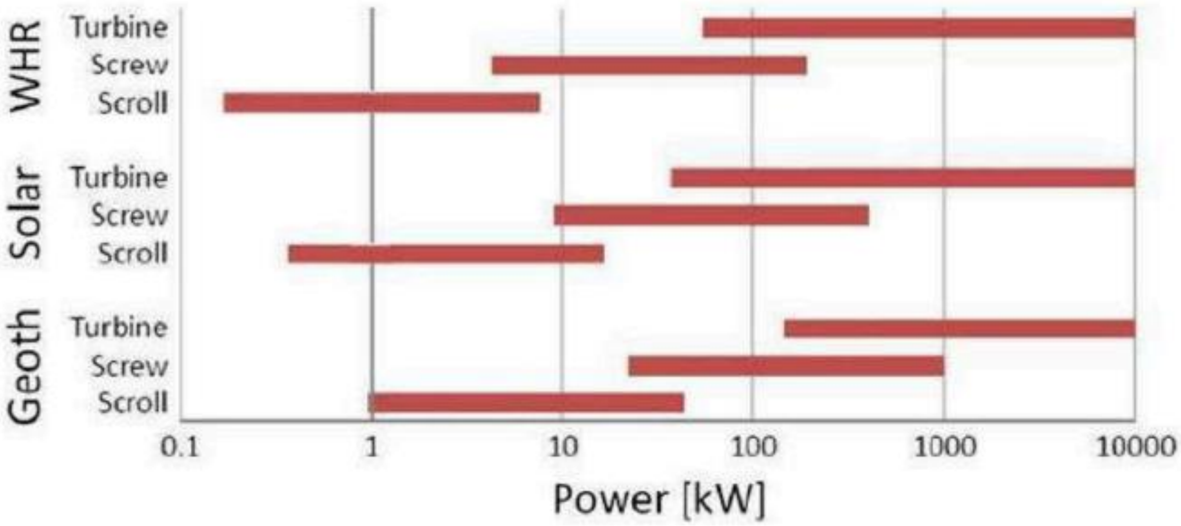

Fig. 2.4. Turbine/Expander classification based on power generation and heat source

The expander represents the system's crucial element as it converts the energy contained in the working fluid into mechanical energy. The main characteristics that the component must have can be summarized in the following points:

- Conversion efficiency
- Compactness
- Simplicity and ease of maintenance
- Optimization of the component for the application
- Possibility of use in different working conditions
- Easy availability and use
- Low cost and noise

Regarding usable expanders, the first distinction can be made between turbomachines and volumetric machines. For small-scale applications, the volumetric machines are more appropriate because low flow rates, and high flow ratios lower expansion and rotation speed than turbomachines characterize them. While turbomachinery represents a mature technology for large ORC plants, almost all volumetric machines used in small applications are prototypes or even derived from different applications such as compressors.

2.1.3. Volumetric expander

The expanders volumetric has the advantages of a limited number of revolutions, conversion efficiency thermodynamics, reliability and tolerance to the formation of liquid drops during the phase of expansion. From an analysis of the scientific literature, graphically summarized in Fig. 2.5, it emerged that, with the boundary conditions and for the objectives set, the ideal expander to use is the Scroll-type. This machine is a compressor for air conditioning systems in the automotive sector. It is practically the only device used in ORC applications for low-temperature heat recovery, and it has system sizes of up to 10 kW electric.

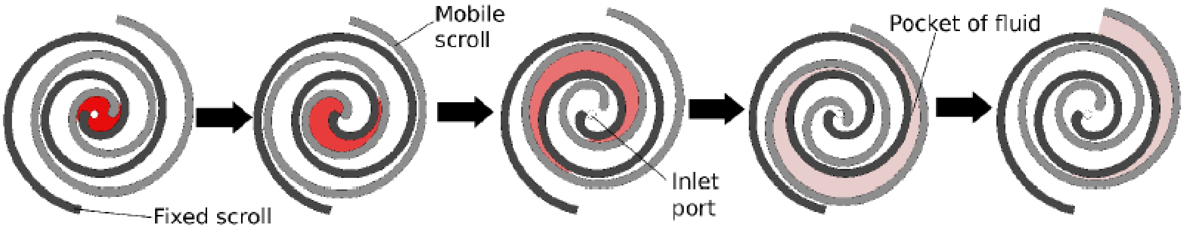

Fig. 2.5. Expansion process in scroll expander (Quoilin et al., 2013)

The scientific literature is attentive to developing and optimizing Scroll machines for small ORC applications. Some fundamental aspects of studying this machine will be discussed in this paragraph. The operating principle of scroll-type expanders is based on the displacement reciprocal of the stator and rotor, both in the shape of a spiral, obtained through an element orbiter created with an eccentric element on the crankshaft. The expansion process is illustrated in Fig. 2.6, the working fluid enters the scroll from the centre, trapped and guided in a volume that progressively increases, moving towards the radial periphery of the machine where the fluid is discharged from the discharge port.

The ratio between the volumes of the inlet and outlet chamber is defined as a design volumetric expansion rate due to the construction geometry of the machine. Based on this consideration, two types of loss can be identified:

- Under-expansion occurs when the geometric ratio value of machine expansion is less than the system expansion ratio achieved between evaporation and condensation temperatures. This situation is represented in the graph (Fig. 2.6a), and the loss associated with this condition consists of the lack of exploitation of the expansion of the fluid, resulting in a reduced extraction of work.

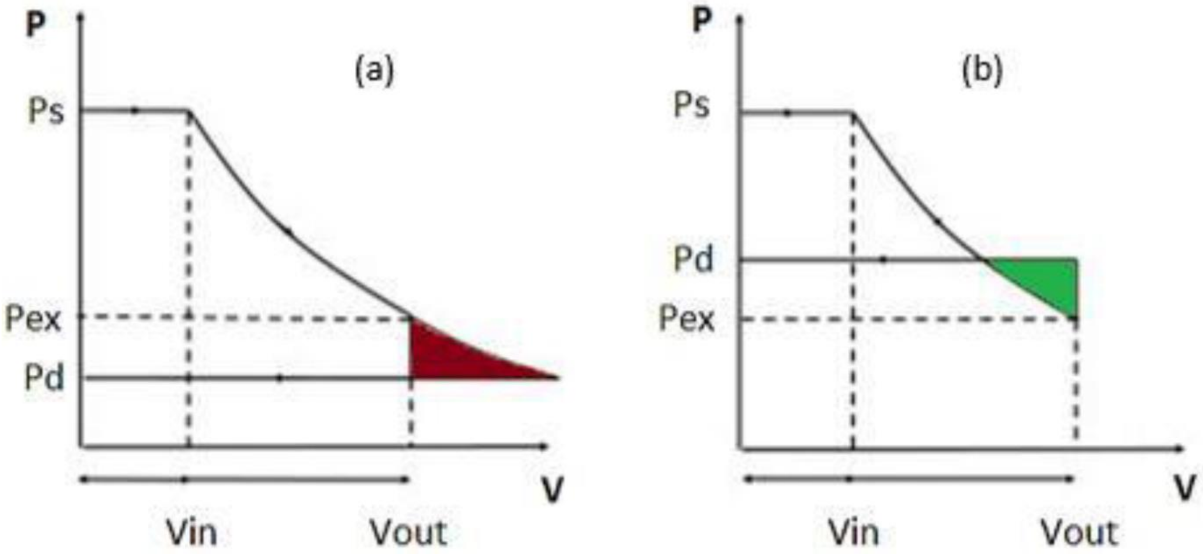

Fig. 2.6. PV graph of scroll expander: a) under expansion, b) over expansion (Campana et al., 2019)

- Over-expansion its contrasts with the previous phenomenon (Fig. 2.6b), in which the fluid exiting the expander encounters a pressure higher than that determined by the geometric expansion ratio of the machine that reduces the expansion of the fluid and, consequently, the work extract.

These two effects can considerably reduce the performance of the expansion process. Other sources of inefficiencies are represented by friction and fluid lamination from the seals of the moving parts, heat loss with the external environment and losses of pressure concentrated in the expander inlet port. Some efficiency loss types are represented in Fig. 2.7a and Fig. 2.7b. In the first one, it can be observed how, during a part of the aspiration process, the opening area of the supply duct is partly blocked by the expander rotor. The filling process will, therefore, lead to a loss of pressure of the working fluid in the input expander. Moreover, it's possible to observe that the sealing gasket placed at the end of the stator and rotor values does not cover the entire radial development of themselves. This allows fluid to seep to the ends of the spirals and will result in a loss of work extracted from the fluid and flowrate value higher than that allowed by the volume of the expander. Another important parameter for evaluating the working conditions of the scroll expander is the isentropic efficiency (ratio between the actual enthalpy change and the theoretical enthalpy change).

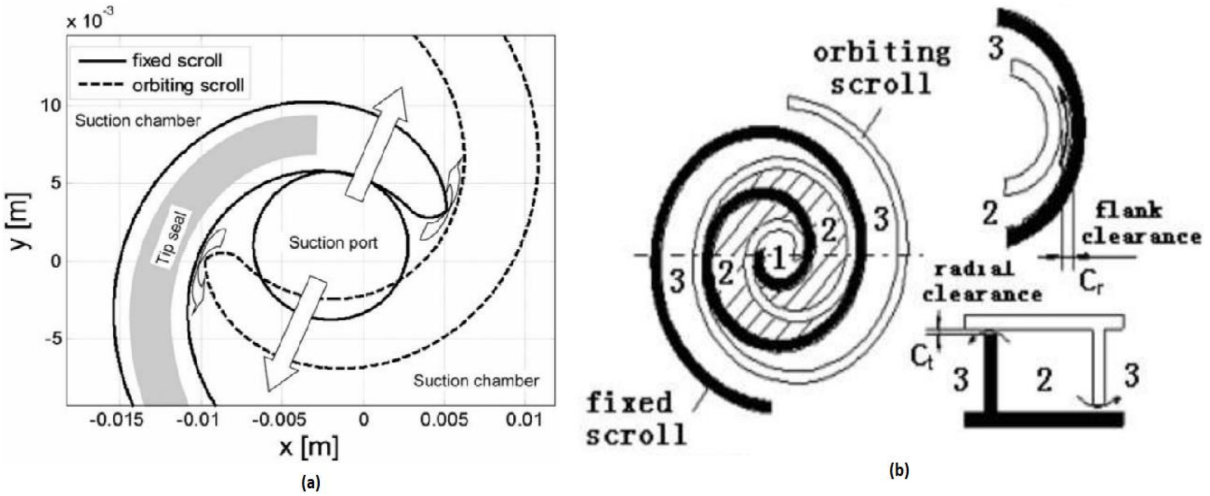

Fig. 2.7. Expansion detail process in scroll expander a) geometrically, b) passages (Xiaojun et al., 2004)

This parameter can measure the extent of the irreversibilities of the expansion process and is an index of comparison between different machines and construction technologies. Different definitions of these parameters are found in scientific literature and experimental fields. Generally, encounters the difficulty of directly evaluating the conditions of the exiting fluid flowing the expander due to:

- Difficult to access on compact machines
- Uncertainty and complication of the measurement system to be used
- Heat losses to the external environment, which affect the measured values
- Thermal inertia of some components

The listed complications can lead to experimental identification of completely erroneous quantities; for example, due to over or under-expansion phenomena and heat losses to the external environment, it is possible to identify values of entropy of the outgoing fluid lower than those of the incoming fluid. For the reasons listed, the isentropic efficiency is conventionally defined as the ratio between power generated by the expander and the ideal enthalpy change multiplied by the flow rate of the working fluid. The isentropic efficiency, defined, brings with it information not only of a thermodynamic nature but also includes the coefficient of filling, the conversion efficiency into mechanical energy, and, for some types of expanders with an integrated electric generator, the energy conversion efficiency. This parameter, not exactly rigorous in its definition, is widely used in scientific literature and is easy to use for making immediate comparisons on the performance of machines built with different technologies.

The model selected for the application, Fig. 2.8 is a commercial product of Sanden. It is part of the category of hermetic compressors; beyond the suction of the delivery and electrical contacts, it has no access to the inside of the casing of the car. The device is equipped with a three-phase asynchronous electric motor with a permanent magnet with four pole pairs, which will be used as an electric generator in the specific application. The displacement of the scroll, when used as an expander, has a value of 33 cm^3 and a geometric compression ratio of 4. Before being mounted on the prototype system, the device was tested in an open circuit with compressed air to determine the electrical characteristics of the generator. The tests were necessary to create the control system through variation of the electric charge.

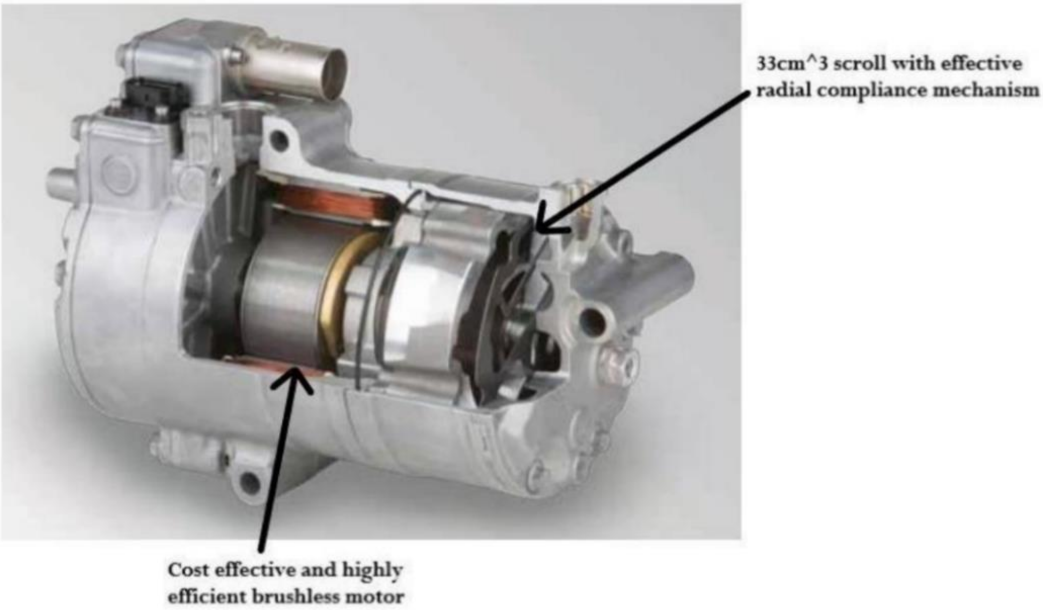

Fig. 2.8. Automotive scroll drive from Sanden (De Lucia et al., 2024)

2.1.4. Turboexpander

Currently, there are two main types of turbines used in Organic Rankine Cycle (ORC) systems: axial turbines and radial inflow turbines.

- **Axial turboexpander** have a distinct design when used with high molecular weight working fluids. A key difference between organic fluids and steam lies in the enthalpy drop during expansion, which is much greater for steam. As a result, fewer stages are required for organic fluids, and single-stage turbines can even be used for low- or medium-temperature ORC cycles. Another characteristic of organic fluids is their low speed of sound, which is reached more quickly in ORC systems than in steam cycles. This can limit turbine performance, as high Mach numbers can lead to increased irreversibilities and reduced turbine efficiency.
- **Radial inflow turboexpander**, on the other hand, are designed for high pressure ratios and low flow rates of working fluids. Their geometry supports higher peripheral speeds compared to axial turbines, allowing for a larger enthalpy drop per stage. Radial turbines also maintain good efficiency over a wide range of part-load conditions. However, unlike axial turbines, it is difficult to assemble multiple stages in series for radial inflow turboexpander.

Fig. 2.9 presents a typical maximum efficiency curve as a function of the specific speed for a radial turbine and Eq. (2.1) is represented the specific speed is defined as a dimensionless parameter that relates the rotational speed, flow rate, and enthalpy drop of the turbine.

$$N_s = \frac{2\,\pi\,N\,\sqrt{\dot{V}_{ex}}}{\Delta h_s^{0.75}} \tag{2.1}$$

It provides a way to compare turbines of different sizes and types based on their performance under varying conditions. Typically, the specific speed helps in optimizing the design of the turbine to ensure that it operates at its maximum efficiency within the desired operating range. Therefore, turbomachines are not well-suited for very small-scale units, primarily because their rotational speed increases significantly as the turbine's output power decreases.

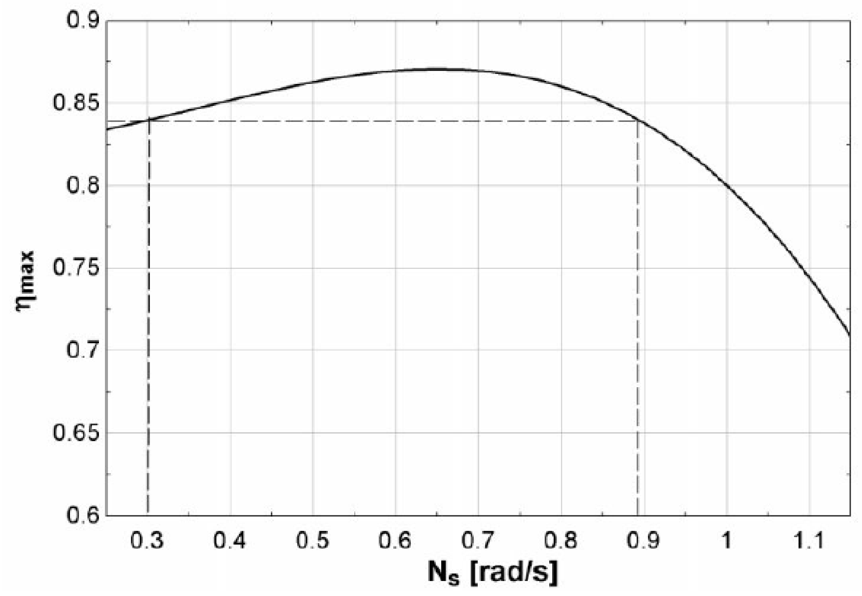

Fig. 2.9. Performance graph of turboexpander based on N_s vs η_{max}

2.2. Geothermal waste heat

Geothermal energy is heat (thermal) energy from the Earth (geo). This heat energy is contained in rocks and fluids (which fill fractures and pores in rocks) in the Earth's crust. The average temperature gradient for planet Earth is around 20 °C/km, as shown in Fig. 2.10. However, there are many areas throughout the world where the temperature gradient is higher; the deeper one accesses, the higher the temperature.

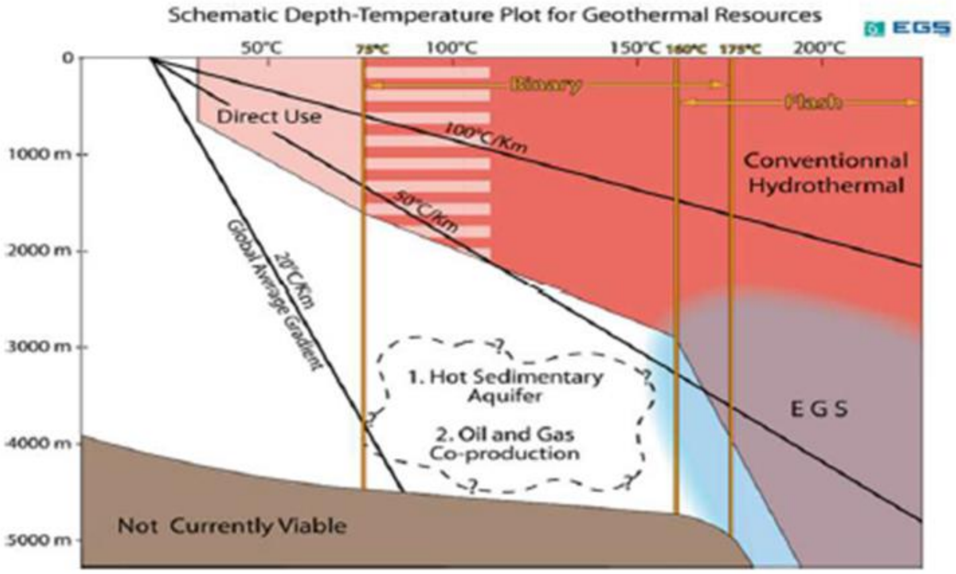

Fig. 2.10. The gradient average temperature of geothermal (Dickson and Fanelli, 2024)

With a temperature gradient between 50 and 100 ℃, geothermal sources are more easily accessible (Dickson and Fanelli, 2024):

- Temperature 20 °C, geothermal heat can be used directly for greenhouses, pond heating and area heating.
- Temperature 75 °C, geothermal heat can be used as an electricity generator using binary cycle technology.
- A temperature of 160 °C for flash-steam generators can be used for the GPP.

Geothermal energy does not depend on weather changes. It is suitable for base load operation compared to other renewable energies, which provide clean energy and a reliable source and are available in various world regions. In Indonesia, a nation with abundant resource of geothermal, only a fraction of its vast potential has been harnessed, making innovations in this field critical. This study focuses on the Darajat GPP, a vapor-dominated system contributing significantly to Indonesia's energy grid. Sukra et al., (2022) developed a simplified analysis tool using Microsoft Excel, integrated with thermodynamic properties, to model key plant components, including turbines, condensers, cooling towers, and gas removal systems. The tool’s ability to simulate varying conditions, such as changes in environmental humidity, condenser efficiency, and cooling tower performance, offers operators an accessible means to predict and mitigate performance losses.

The advantages of this paper lie in its practical approach to addressing the complexities of GPP operation. The validated model not only reflects real-world conditions but also demonstrates the direct impact of environmental and operational changes on turbine performance. For instance, it shows how increased relative humidity or reduced cooling efficiency can lead to significant power losses, offering valuable insights for improving system reliability. By empowering operators with a user-friendly tool for quick decision-making, the study bridges a gap in the availability of practical, comprehensive simulation tools for GPPs, paving the way for enhanced efficiency and resilience in geothermal energy systems.

Geothermal energy can be the right solution to reduce the effects of global warming because the availability of geothermal energy in Indonesia is very high. Interest in developing geothermal energy is increasing due to rising world oil prices. Geothermal energy can be used for electricity generation, and direct use depends on a source's potential temperature and chemistry. Electricity production is the most important geothermal energy utilisation from high-temperature geothermal sources. In contrast, geothermal heat sources with higher temperatures (>150 °C) allow for combined heat and power (CHP) generation. Here, the condensing temperature is set higher (e.g., 60 °C), enabling the use of cooling water for district heating. While, this approach improves overall energy recovery efficiency, it comes at the cost of reduced electrical efficiency.

In a binary plant (Fig. 2.11), the thermal energy from the geofluid is transferred to a secondary working fluid through a heat exchanger, enabling its use in a conventional Rankine cycle. The organic working fluid (such as butane or pentane), selected for its suitable thermodynamic properties, absorbs heat from the geothermal fluid, evaporates, and powers the turbine. Afterward, it is condensed and pumped back to the evaporator by the feed pump. The cooling system is provided through various methods, including air coolers, surface water cooling systems, wet-type cooling towers, or dry-type cooling towers.

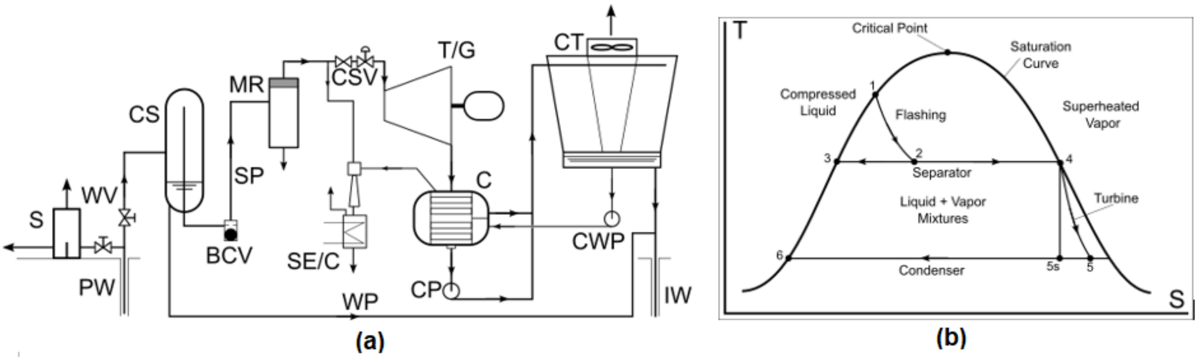

Fig. 2.11. Binary cycle of GPP: a) schematic, b) T-s diagram (DiPippo, 2012)

A crucial element in binary geothermal systems is the selection of the working fluid. The fluid must be carefully chosen to minimize exergy destruction in heat exchangers by better matching with the brine, reduce the size of heat exchangers and turbines, and maximize power output. Additionally, the health, safety, and environmental characteristics of the fluid must not be overlooked. Research by DiPippo, (2012), Permana et al., (2021) identified ammonia, butanes, pentanes, and synthetic fluids like R-245fa and R-227ea as suitable candidates for ORC binary plants.

The low-temperature binary geothermal plant is known for relatively high auxiliary power consumption, with pumps using between 30% and over 50% of the gross output power (Frick, 2009). The largest energy consumer is the brine pump, which needs to circulate brine over long distances and at a high flow rate. Additionally, the working fluid pump consumes more energy compared to higher-temperature cycles, as the "back work ratio"—the ratio of pump consumption to turbine output power increases as the evaporating temperature decreases. Geothermal heat sources with temperatures exceeding 150 °C can support CHP generation. In such systems, the condensing temperature is raised (e.g., to 60 °C), enabling the use of cooling water for district heating. This approach enhances the overall energy recovery efficiency but results in a reduction in electrical efficiency.

New designs have been proposed to optimize the use of geothermal resources, such as dual-pressure and dual-fluid binary cycles, as well as combined and integrated flash-binary plants. Dual-pressure systems utilize two turbines or two-stage pressure turbines, while dual-fluid systems integrate two cycles using the same resource. Combined and integrated flash-binary plants combine the benefits of flash and binary systems. With growing concerns over climate change, many governments are seeking clean electricity generation technologies. Geothermal binary systems, offering nearly zero harmful emissions and backed by a well-established industry, could play a significant role in regions where conditions are favourable.

2.3. Solar energy integration with ORC

Solar-ORC is considered the most feasible and competitive power generation similar to the Rankine cycle but uses organic working fluid from the solar heat sources (Tzivanidis et al., 2016). Therefore, when discussing solar energy as the heat source for an ORC, it is crucial to use precise terms to avoid confusion. According to the terminology, solar radiation is a general term that encompasses all forms of solar energy reaching the Earth's surface, including both direct and diffuse components. It is often used as an umbrella term but lacks specificity (Smith et al., 2019). So, there are two general terms to describing solar heat sources:

- **Direct Solar Irradiation (DNI)**: The portion of solar radiation that travels directly from the sun to a specific surface without atmospheric scattering. DNI is essential for concentrating solar power (CSP) systems, such as parabolic troughs or solar towers, which are often paired with ORC systems to achieve the high temperatures required for efficient operation (Jones et al., 2020).
- **Global Solar Irradiation (GHI)**: The total solar radiation received on a horizontal surface, comprising both direct and diffuse components. GHI is applicable to non-concentrating solar collectors, such as flat-plate or evacuated tube collectors, which are typically used in lower-temperature ORC applications (Lee et al., 2021).

Using specific terms like DNI and GHI ensures clarity in technical communication and facilitates accurate system design and analysis. Furthermore, it highlights the suitability of ORC systems for regions with varying solar resource profiles, emphasizing their adaptability and potential for integration with solar energy technologies (Zhao et al., 2023). In conclusion, the choice of solar input DNI or GHI directly influences the design and efficiency of solar-driven ORC systems. Properly aligning the collector type with the solar resource ensures optimal energy utilization, making ORC systems a promising solution for sustainable energy conversion, particularly in regions with abundant solar energy.

The primary system of solar-ORC has been touched from the previous paragraph. They are as follows: 1) a solar thermal collector, 2) a TES system, 3) an ORC’s system. The essential part of solar-ORC is the evaporator, which stands for evaporation of the organic fluids or refrigerants, the condenser is a component to condense a working fluid from vapour phase into fluid phase, the pump which is to pressurize a fluid phase of the working fluid, and the turbine is the component that expands the working fluid and converts to electricity. The solar-ORC-based may bear a low efficiency and energy output when the heating temperature of the heat source is low.

2.3.1. Solar-ORC by heat medium

A method to increase the thermal efficiency of ORC can be performed through working fluid selection, as it is an influent factor as it depends on the heat characteristic. Tchanche et al., (2010) conducted a thermodynamic analysis of the performance and characteristics of different working fluids in a low-temperature solar-ORC. In comparison, Rayegan and Tao (2011) simulated of 117 organic fluid selections based on the T-s diagram, fluid effects and molecular components. The result is about improving thermal efficiency and choosing the suitable working fluids. In solar-ORC applications, there are two ways to utilize solar thermal energy. These are using an evaporator to heat working fluids directly, namely direct vapour generation (DVG) and indirectly by using heat transfer fluid (HTF). Fig. 2.12a shows a solar-ORC scheme using DVG technology, while Fig. 2.12b is a solar-ORC scheme using HTF technology.

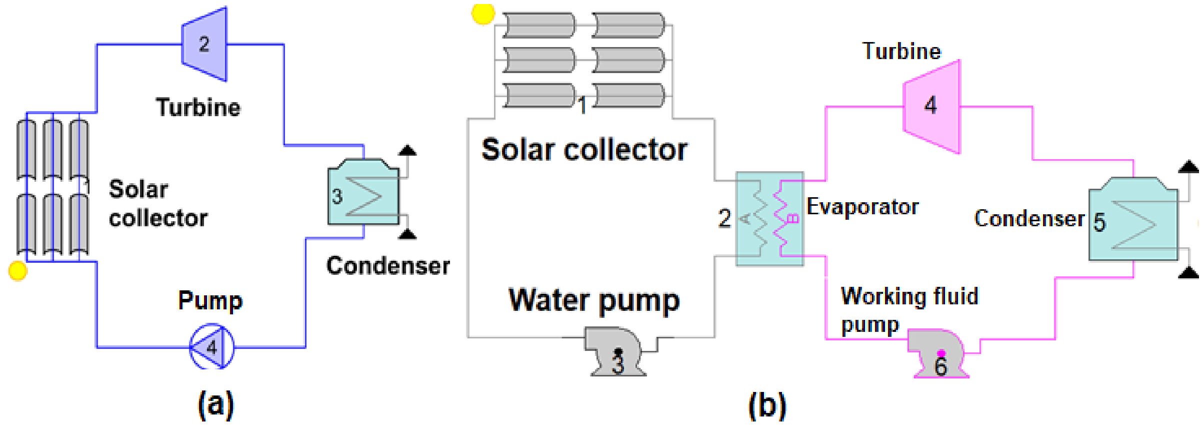

Fig. 2.12. Solar-ORC: a) DVG system, b) HTF system (Permana et al., 2022)

One of the advantages of using DVG technology is the absence of heat exchanger components to evaporate the working fluid as presented. Some projects using the DVG system have been demonstrated by Alguacil et al., (2014) with a plant of 2.67 MWe and which has been built by Abengoa Solar. Another solar-ORC plant using DVG technology has been operated and generated 5 MWe with around 410 °C temperature and 78 bar pressure, respectively (Ktistis et al., 2021). Finally, the biggest solar-ORC plant has been built by Solar One Company with a capacity of 10 MWe and a temperature of around 425 °C in Barstow, USA (Feldhof, 2012). Another advantages of DVG technology are (1) the high evaporation temperature that increases high efficiencies, (2) low thermal inertia, (3) a fast ignition system as compared with HTF technology. However, the DVG technology has also disadvantages including the immense environmental sensitiveness where the intensity of sun-ray, and cloudy periods can vary the temperature of evaporation that can lead to the vapour flow rate that enters the turbine and resulting in low power output and efficiencies (Marion et al., 2014).

2.3.2. Solar-ORC by temperature ranges

The solar collector is the component that converts solar irradiation energy to thermal energy through working fluid in solar thermal applications. Solar collectors can be classified based on the transport medium (heat transfer fluid or working fluid) heated to low, medium and high-temperature ranges. The low temperature of solar collector can heat the working fluid between 30-200 °C, the medium temperature of solar collector can heat the working fluid between 200-400 °C, while the high temperature of solar collector's usage is above 450 °C. Fig. 2.13 depicts the several types of solar collector technologies that are regularly uses (Tchanche et al., 2011). The types of solar collectors that do not concentrate solar irradiance at one focal point include evacuated tube collector (ETC), compound parabolic collector (CPC), flat plate collector (FPC), and advance FPC, which can heat the working fluid at a low temperature of less than 200 °C. Nonetheless, solar collectors that concentrate solar irradiation at one focal point, such as parabolic through collector (PTC) and linier Fresnel collector (LFC), can heat the working fluid in the medium temperature range from 100-400 °C. Meanwhile, at very high temperatures around >450 °C, the type of solar collector used are a dish concentrator and a heliostat+ central receiver.

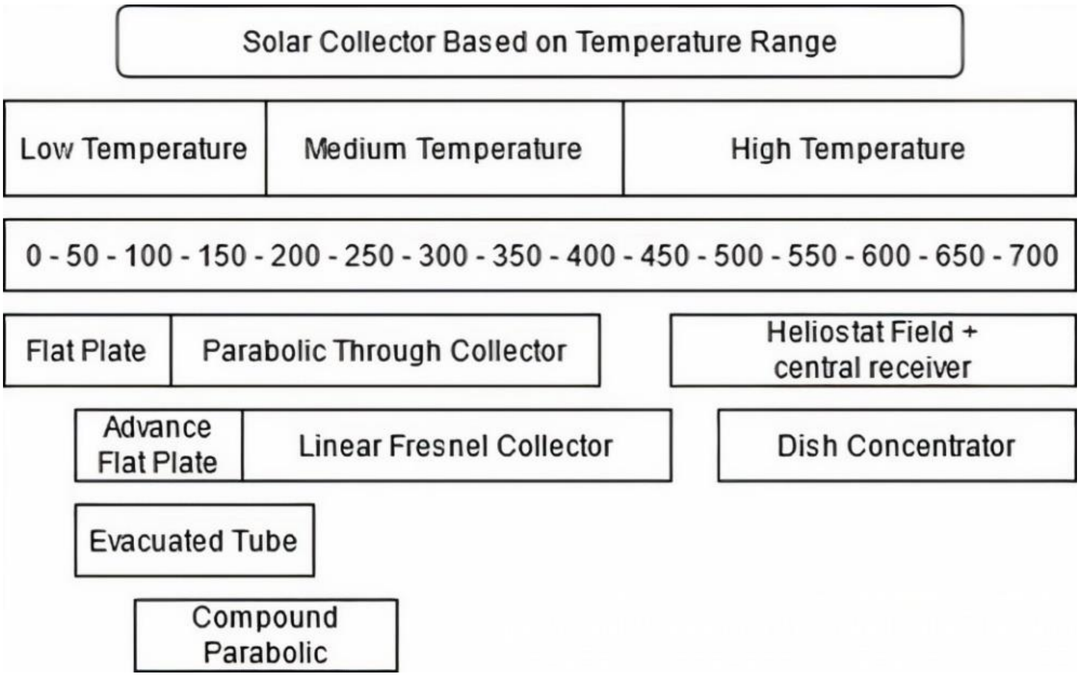

Fig. 2.13. Solar collector classification based on temperature range

2.4. Thermal energy storage application for ORC

TES is increasingly used in ORC systems to enhance efficiency and flexibility in both small-scale and industrial applications. TES allows ORC systems to store excess thermal energy when heat is abundant and release it during periods of low heat availability, ensuring a more stable and continuous power generation.

In small-scale ORC systems, TES is often used to improve system efficiency in renewable energy applications, such as solar-ORC or biomass-ORC systems. By storing thermal energy during periods of high solar radiation or biomass availability, the stored energy can be used later when heat input is lower. Phase Change Materials (PCM) and sensible heat storage are common TES technologies in small-scale ORC systems. These systems can help manage fluctuating energy inputs and ensure smoother operation with less reliance on continuous heat sources. In industrial applications, TES is typically used in conjunction with larger ORC plants to improve performance, particularly in waste heat recovery and geothermal ORC systems. Large-scale TES systems allow industries to capture waste heat from processes during peak production and store it for later use, helping to maximize the overall efficiency of the ORC plant. **Molten salts** and **pressurized water systems** are common TES methods in industrial ORC setups. These systems enable industries to optimize the use of waste heat and renewable energy, extending operational hours and ensuring a more reliable energy output, even when heat sources are intermittent.

2.4.1. TES-ORC configuration

A study by Kolasiński (2020) identified six potential TES configurations for ORC systems, which can be used to capture heat from various low- and medium-temperature renewable and waste heat sources. This review also highlights additional possible TES configurations for a basic ORC system, as illustrated in Fig. 2.14(a)–(f). Hot TES devices can be integrated into ORC systems as depicted in Fig. 2.14(a) and Fig. 2.14(b), with the system design in Fig. 2.14(a) resembling a solar-powered ORC system (see Fig. 2.14(a)). Fig. 2.14(c) presents a design where the TES device is used to preheat the organic working fluid. Fig. 2.14(d) shows a layout where cold TES is employed in an ORC system, potentially storing cold energy (such as the energy from liquefied natural gas at around −160 °C) to condense the organic working fluid. Several studies have reviewed, researched, and modelled the use of this cold energy to generate electricity (Bao et al., 2017; Daniarta and Imre, 2020; He et al., 2019). It is also possible to combine hot and cold TES in a system, which can be beneficial when heating and cooling sources are limited or variable. This combination allows for stabilizing system performance by maintaining a controlled operating temperature range. Additionally, in combined systems such as an ORC with a direct expansion process, TES can be used to store thermal energy from other heat sources before entering the direct expander, as shown in Fig. 2.14(e) and Fig. 2.14(f).

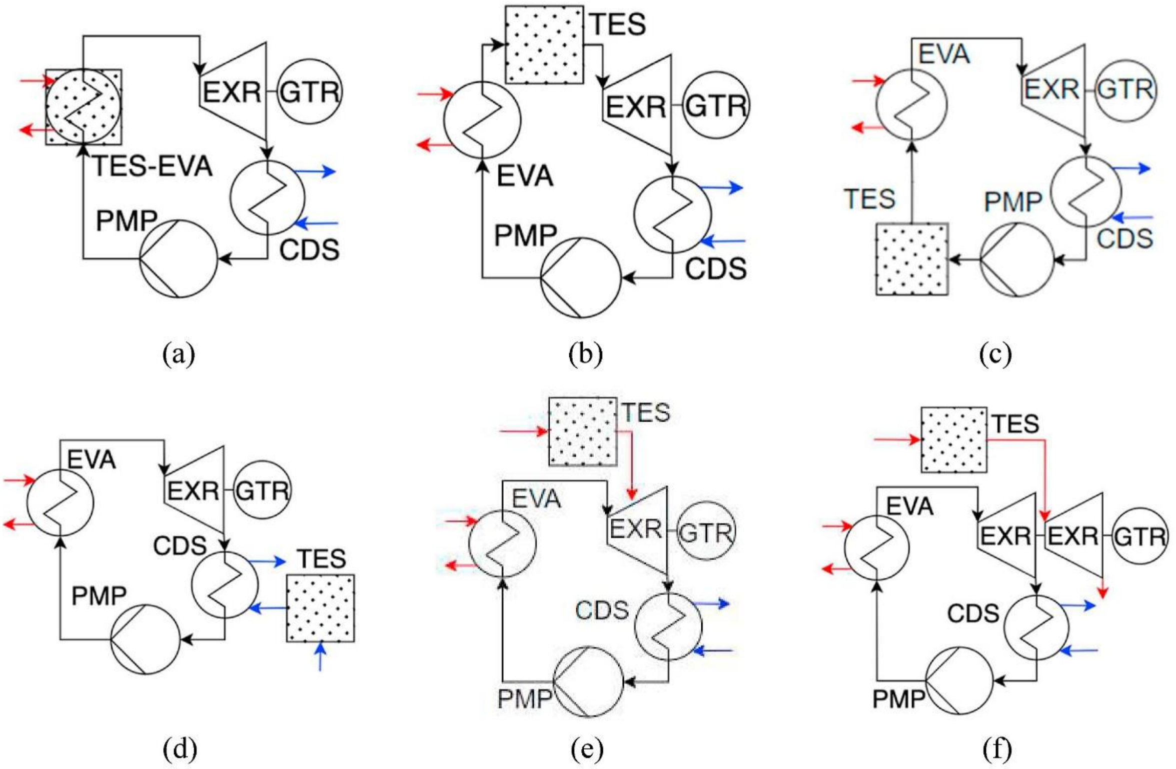

(a) (b) (c)

(d) (e) (f)

Fig. 2.14. TES-ORC configuration (Daniarta et al., 2023)

2.4.2. TES materials selection

Different types of TES materials are classified based on the physical phenomena responsible for their TES capabilities, such as thermal or chemical (Sharma et al., 2009; Su et al., 2015). The graphical interpretation of these phenomena for various TES materials is illustrated in Fig. 2.15. Thermal TES materials are further divided into two main categories: sensible heat materials (e.g., liquids and solids) and latent heat materials (e.g., solid-solid, solid-liquid, liquid-gas, and solid-gas). A review article (Su et al., 2015) provides a detailed classification of solid-liquid materials, which are further grouped into organic, inorganic, and eutectic materials, as depicted in Fig. 2.16.

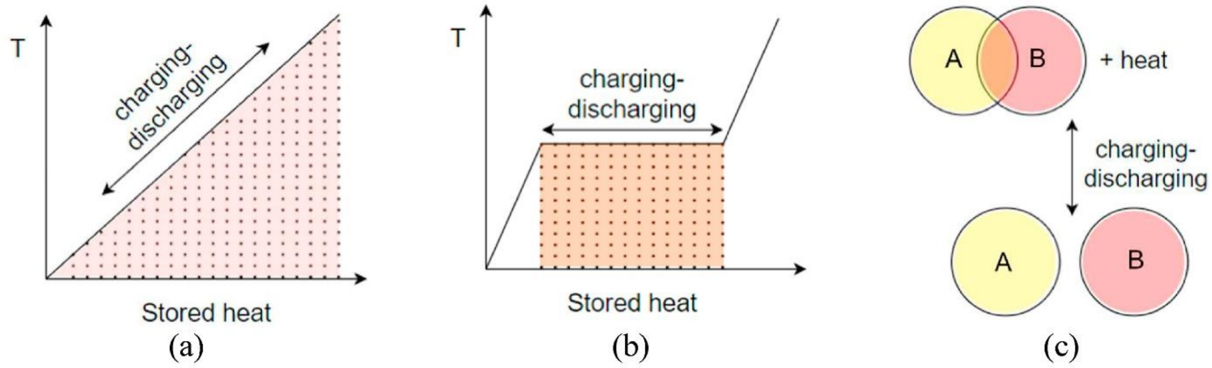

Fig. 2.15. The graphical of TES physical phenomena: a) sensible heat, b) latent heat/phase change, c) thermochemical storages (Daniarta et al., 2023)

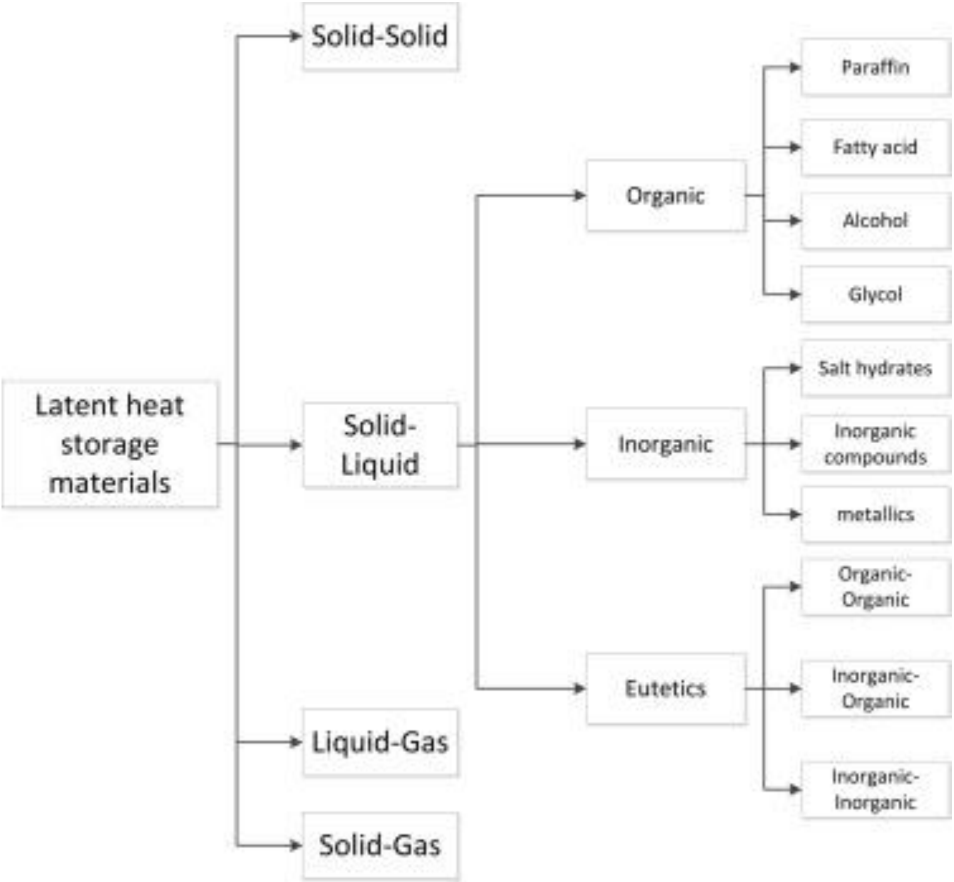

Fig. 2.16. Classification of PCMs (Su et al., 2015)

2.5. Biomass and ORC

2.5.1. Biomass-ORC system

Biomass is defined by the Energy Security Act (PL 96-294 1980) as organic substances available in renewable form, crops including agricultural waste and residues, wood and wood waste, animal waste, municipal waste, and aquatic plants (Bracmort, 2019). When biomass is burned, the CO_2 produced will be recycled by living plants through photosynthesis and released again when burned. Thus, the process of burning biomass does not cause a greenhouse effect, unlike burning fossil fuels. The heat from burning biomass is generally used for heating and drying. The required temperature for this process ranges from 50-100 °C, far below the biomass burning temperature (1000 °C). This temperature difference shows the potential for heat from burning biomass to be converted into electrical energy. However, due to the character of flue gas, which is low pressure and contains ash, it cannot be directly used to produce electrical energy like turbine gas. Other processes must be taken to convert this heat into electricity, including the organic Rankine cycle. Systems that use heat from burning biomass for drying and heating and to generate electricity are called CHP Plants.

Apart from direct combustion, the technology being developed to convert energy from biomass is the gasification process. In this process, biomass is converted into synthetic gas, the main composition of which consists of H_2, CO, CO_2, and CH_4. Synthetic gas containing particulates will be filtered before being burned in an internal combustion engine or gas turbine, as in Fig. 2.17.

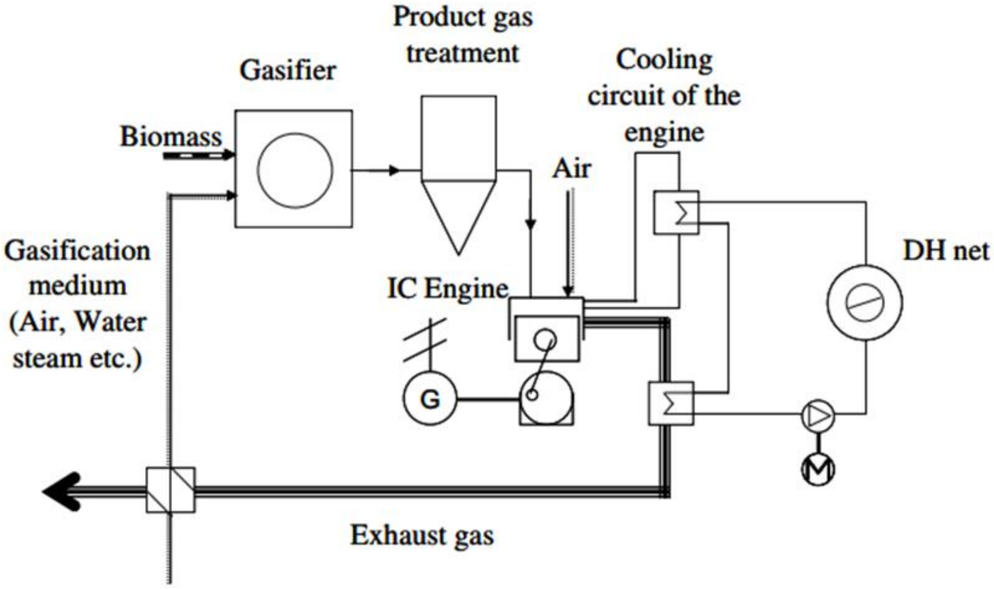

Fig. 2.17. Biomass combustion process schematic

Rentizelas et al., (2009) compared the technology and costs of biomass conversion with gasification and direct burning; they showed that gasified biomass requires higher investment and maintenance costs of 75% and 200% compared to direct burning biomass. On the other hand, the biomass conversion process with gasification produces higher thermal efficiency. Normally, ORC converts low-temperature heat sources, while the heat produced from burning biomass is high-temperature. Because, in general, the working fluid used for ORC tends to be unstable if used at high temperatures, a secondary system needs to be created so that heat transfer from the exhaust gas to the working fluid can take place properly, one of which is by using a closed loop thermal oil or ordinary pressurized water. It is called heat transfer fluid (HTF), as seen in Fig. 2.18. A system like this requires a heat exchanger and additional power for the pump.

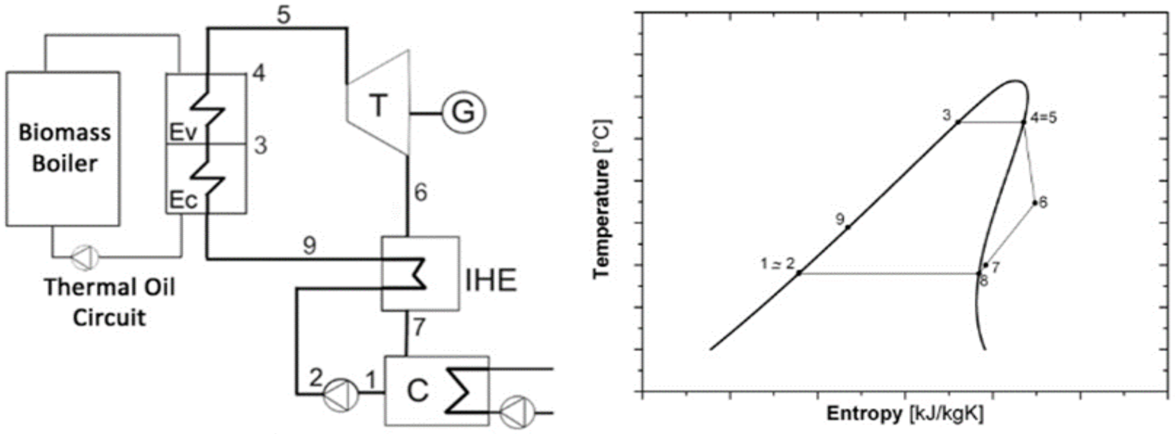

Fig. 2.18. Biomass-ORC in HTF process

Another method is direct evaporation, in which the working fluid is directly heated by the heat from the exhaust gas resulting from burning biomass, as in Fig. 2.19. This method requires more attention to the safety aspects of the operation. Still, it can increase the thermal efficiency of the system. The direct evaporation system requires cleaning the evaporator while operating because the exhaust gas contains around 1,000-10,000 mg/Nm^3 of ash (Ganassin and van Buijtenen, 2015). Although cooling the flue gas to reduce the ash content before entering the evaporator can reduce the ash content to 200 mg/Nm^3, the formation of deposits in the evaporator cannot be avoided. Hence, a cleaning system is required during operation (Ganassin and van Buijtenen, 2015). This adds to the complexity of ORC system operations and increases initial costs and maintenance costs.

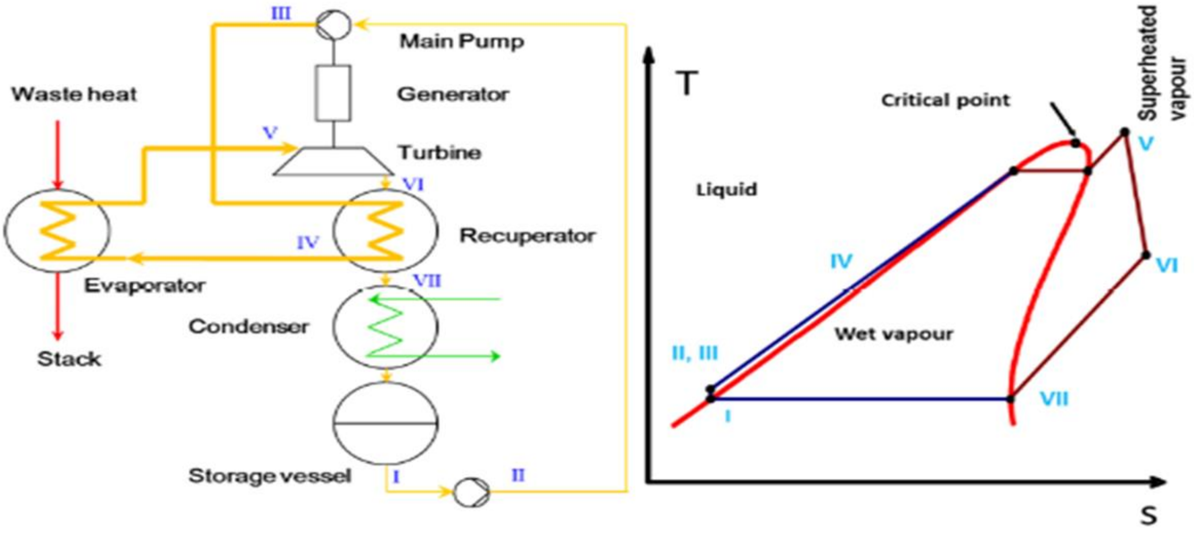

Fig. 2.19. Direct evaporation of biomass-ORC (Rentizelas et al., 2009)

2.5.2. *Biomass-ORC in Italy*

Biomass plays a crucial role in Italy's renewable energy sector. In 2016, energy production from biomass and waste sources reached 19.38 TWh, a significant increase from 10.832 TWh in 2011. By 2018, energy output remained steady at 19.23 GWh, reflecting a consistent trend over the previous three years. Italy's biofuel demand is projected to reach 2.8 million tonnes of oil equivalent by 2025 and is expected to remain stable until 2040 (Pessina and Facchinetti, 2006).

According to ORC map.org, 430 biomass-ORC projects, with a combined capacity of 330 GW, have been installed worldwide over the past 15 years. Europe hosts the majority of these projects, with Italy leading in the number of installations at 23, while Germany ranks first in installed capacity with 125 GWe (Tartière and Astolfi, 2017). Despite the extensive use of biomass-ORC systems, few studies have examined the recovery of heat from biomass combustion waste at low to mid temperatures. One such study by Oyekale et al., (2019) analyzed the cost-effectiveness of retrofitting biomass in hybrid concentrated solar power (CSP)-Biomass ORC power plants, both in constant and modular modes.

Italian biomass-ORC plants often integrate with other renewable technologies, such as CSP, to improve efficiency and flexibility. A notable example is the hybrid CSP-biomass ORC power plant in Ottana, Sardinia, which combines linear Fresnel solar collectors, thermal oil storage tanks, and a 630 kW ORC unit (Petrollese et al., 2017). Studies have shown that retrofitting biomass into existing CSP-ORC systems can enhance electrical efficiency by up to 5% and extend operational hours to as much as 3,500 annually. The economic performance is also favourable, with a payback period of 1.4 years and a competitive levelized cost of electricity (LCOE) of 109 GBP/MWh (Oyekale et al., 2019). Moreover, Italy has made significant strides in biomass-ORC technology, challenges remain, particularly in optimizing heat recovery and improving system efficiencies. Research is ongoing to explore better integration of biomass and waste heat recovery, aiming to reduce exergy destruction and minimize heat exchanger and turbine sizes. Future innovations may focus on improving performance through advanced controls, hybrid systems, and incorporating other renewable sources, positioning Italy as a leader in biomass-ORC technology within Europe and globally.

2.5.3. Biomass-ORC in Indonesia

In developing environmentally friendly combustion fuel technology other than biomass, Indonesia has also applied a biodiesel fuel mixture of up to 30% derived from palm oil. However, some disadvantages that need to be considered when using biodiesel are poor viscosity and atomization, leading to higher NO emissions and lower efficiency. Many authors agree to reduce exhaust emissions without reducing engine performance by varying the mixture of diesel fuel with biodiesel. Kristiyadi et al. (2022) have conducted experimental tests on three biodiesel mixtures (B30, Dexlite, Pertadex) on the market with ordinary fossil fuels regarding performance, fuel consumption and emissions. As a result, Pertadex produces the highest performance and lowest fuel consumption, while B30 is the biodiesel that produces the lowest emissions.

Indonesia, with its vast agricultural resources, has significant potential for utilizing biomass as a renewable energy source. The country produces large quantities of agricultural waste from palm oil, rice, sugarcane, and forestry industries, making biomass a promising feedstock for energy generation. ORC technology, which is suitable for low- and medium-temperature heat sources, is gaining attention in Indonesia as a means of converting biomass energy into electricity, especially in remote or off-grid areas. Indonesia generates a substantial amount of biomass waste from its agricultural and forestry sectors. Some of the key biomass resources include:

- **Palm Oil Residue**: As one of the world's largest palm oil producers, Indonesia generates a significant amount of palm oil residues, such as empty fruit bunches (EFB), palm kernel shells, and fibre, which can be used as fuel for biomass-ORC systems.
- **Rice Husk and Straw**: With vast rice production, Indonesia has a large supply of rice husk and straw, which are often underutilized but have potential for biomass-ORC power generation.
- **Sugarcane Bagasse**: Indonesia’s sugar industry produces bagasse, a by-product that can be used as a biomass feedstock in ORC plants.
- **Wood and Forestry Waste**: Indonesia’s forestry sector provides sawdust, wood chips, and other forms of biomass that are viable for ORC-based energy production.
- **Elephant grass or Napierr grass** (*Pennisetum purpureum* Schum), commonly grown for livestock feed, is a high-yield biomass crop, producing between 30 and 80 tons per hectare annually. Despite its rapid growth and significant residue production, its use for energy purposes is limited. Farmers and business owners often express concerns about the large volume of residues, challenges with storage, and limited practical applications (FAO, 2017).

The Indonesian government has set ambitious renewable energy targets, aiming to increase the share of renewables in the energy mix to 23% by 2025 (Setyawati and Setiawan, 2024). Biomass, including biomass-ORC, plays a critical role in achieving these targets. Government incentives, such as feed-in tariffs for biomass energy, have been introduced to encourage investment. According to orc-word-map.org, Indonesia only have one biomass-ORC plant with capacity 1150 kWe (Tartière and Astolfi, 2017).

The main challenges include high initial capital costs, lack of awareness of ORC technology, and logistical issues related to transporting biomass in remote areas. Despite these barriers, the potential for scaling up biomass-ORC is high due to the abundant biomass resources and growing demand for renewable energy. With increased investment, government support, and technological advancements, biomass-ORC could become a key player in Indonesia’s renewable energy landscape. In addition to providing clean electricity, biomass-ORC systems can help manage agricultural waste and reduce greenhouse gas emissions, aligning with Indonesia’s commitment to sustainable development and climate change mitigation. The implementation of biomass-ORC technology could significantly benefit rural electrification efforts, provide energy security, and contribute to the country’s renewable energy goals.

2.6. Performance optimisation techniques

ANN have been increasingly applied in performance optimization of ORC systems utilizing geothermal, biomass, and solar heat sources. ANNs are effective in modelling and predicting the complex, nonlinear relationships within ORC systems, making them ideal for optimization tasks. ANN is computational models inspired by the human brain's neural structure. They consist of interconnected layers of nodes (neurons) that process input data to produce output predictions. ANN's flexibility in learning from data without explicit programming makes them ideal for optimizing ORC systems, where multiple variables interact in complex ways. Below is a detailed review of the various performance optimization methods in ORC systems using ANN models:

- ANN-based performance prediction

The objective is to predict ORC system performance metrics such as efficiency, power output, and heat recovery based on different operating parameters. The approach of this method is trained the ANN models using historical data from ORC systems, including variables like heat source temperature, working fluid properties, mass flow rates, and ambient conditions. The advantage of this method is once trained, ANNs can quickly predict performance across a range of operating conditions. ANN models are highly adaptable and can accommodate the complex, non-linear relationships between input parameters and ORC system performance. A study may train an ANN model on data from an ORC system that uses biomass as a heat source, optimizing turbine inlet pressure and evaporator temperature to maximize thermal efficiency (Parnian Gharamaleki et al., 2024, 2024; Zhou et al., 2023).

- Optimisation of thermodynamic parameters

The objective is to optimize key thermodynamic parameters of the ORC, such as evaporator and condenser temperatures, pressure ratios, and mass flow rates, to enhance system efficiency. The approach is employed the ANN models to optimize these parameters based on training data from simulation or experimental results. They learn the best parameter configurations that maximize the performance metrics (e.g., thermal efficiency or exergy efficiency). The advantages of using method is faster than conventional optimization techniques such as genetic algorithms (GA) or particle swarm optimization (PSO) when a large amount of data is available. They can handle multi-objective optimization problems, improving not just efficiency but also minimizing operating costs and environmental impacts. The application is an ORC using geothermal energy, an ANN model might suggest optimal working fluid selection, cycle configuration, and operating pressures that balance high efficiency with lower operational costs (Valencia Ochoa et al., 2023; Wang et al., 2013; Zhao et al., 2018).

- Working fluid selection and optimisation

The objective is to Identify and optimize the best working fluid for a specific ORC application (e.g., waste heat recovery, geothermal energy, biomass, solar energy). The ANN model analyses the performance of various working fluids (e.g., R245fa, R123, Butane, Pentane) across a range of operating conditions, considering factors such as thermal stability, environmental impact, and compatibility with system components. The advantages of using this method are the ANN can efficiently navigate through large datasets of working fluid properties and system configurations to recommend the optimal fluid for maximizing performance. It can factor in environmental criteria (e.g., GWP and ODP of working fluids) alongside efficiency and cost. A study may train an ANN to predict the performance of several working fluids under different heat source temperatures. The model can then identify the fluid that offers the highest thermal efficiency while maintaining safe operating conditions (Chitgar et al., 2023; Mohan et al., 2022; Peng et al., 2021).

- ANN-driven exergy analysis

The objective using this method is Maximize the exergy efficiency of the ORC system by reducing irreversibilities in components like the heat exchangers, turbine, and condenser. ANNs are trained to model the exergy destruction in each ORC component based on operating data. The trained ANN can predict which configurations, and operating conditions minimize these losses, leading to higher exergy efficiency. The advantage of this method is Exergy-based ANN models provide deeper insights into where and how energy losses occur, allowing for targeted optimization by focusing on minimizing irreversibilities, these methods help in identifying optimal design configurations, both for new systems and retrofit applications. An ANN model could analyse a biomass-ORC system and predict the exergy destruction in the evaporator and turbine, helping engineers design a system that minimizes these losses for higher overall efficiency (Chitgar et al., 2023; Utlu et al., 2021).

ANN have proven to be a valuable tool for performance optimization in ORC systems. Their ability to model complex, non-linear relationships and handle large datasets makes them well-suited for optimizing various aspects of ORC performance, from parameter selection to real-time control and fault detection. While ANN offers significant advantages over traditional optimization methods, challenges such as data dependency and model transparency must be addressed to fully harness their potential. Future research should focus on integrating ANN with advanced AI techniques, improving data acquisition, and developing more transparent and interpretable models. By doing so, ANN can continue to enhance the efficiency, reliability, and sustainability of ORC systems, contributing to the broader adoption of renewable energy technologies.

2.7. Summary of literature review

The literature provides a comprehensive framework for addressing the objectives of this thesis, which focuses on optimizing ORC systems across geothermal, biomass, and solar energy applications. For geothermal energy, studies have shown that ORC systems are ideal for low- to medium-temperature heat sources below 180°C, with advancements in thermodynamic configurations and working fluid selection enhancing both efficiency and economic viability. This aligns with the thesis objective of utilizing geothermal energy from the GPP excess steam using energy, exergy, and environmental simulations to optimize performance. Biomass-ORC systems, particularly in countries like Italy, play a significant role in renewable energy generation, especially utilizing heat source from woodwaste. Meanwhile, in Indonesia, several heat sources from biomass derivatives can be used as ORC system, and this realized is from palm oil mills due to the large amount of residue remaining from palm plantations. Alternatively, Biomass from Napier grass is an option for generating Biomass-ORC from a thermoeconomic perspective. This comprehensive approach will provide valuable insights into the performance, sustainability, and economic viability of biomass-based ORC systems, with a focus on optimizing both operational and environmental outcomes.

In solar-ORC systems, literature emphasizes the challenges posed by fluctuating solar irradiation, which can be mitigated through the integration of TES systems. TES, whether based on sensible or latent heat storage materials, is crucial for ensuring reliable power generation, especially in regions with varying solar potential like Hungary and Indonesia. This directly supports the thesis objective of simulating solar-ORC systems in these two locations, focusing on TES sizing and material selection. Finally, performance evaluation and optimization of ORC systems are key areas of interest in the literature, particularly the use of ANN to predict and enhance system efficiency. ANN has been applied to optimize ORC performance by identifying the best operating conditions, a technique that will be employed in the thesis for evaluating a 2 kW ORC test rig in Italy. By integrating insights from these research areas, the thesis aims to advance the understanding and application of ORC technology in renewable energy systems through detailed simulations, exergy analysis, and data-driven optimization.

3. MATERIALS AND METHODS

In Chapter 3, the methodology of various case studies sourced from journals the author has published is explained in detail. Some of them are the biomass-ORC thermodynamic modelling methodology in Indonesia and Italy, the utilization of geothermal waste heat in Tura, and the utilization of solar heat in Indonesia and Hungary with the integration of TES. Furthermore, the method of using ANN on experimental results and optimizing ORC performance.

3.1. Thermodynamic modelling

3.1.1. Mass, energy, entropy, and exergy balance

The conservation of mass principle is a key concept in the analysis of any thermodynamic system. Where the net change in mass flow rate is equal to total mass flow rate entering the control volume reduced by the total mass flow rate exiting the control volume. When applied to a control volume, as illustrated in Fig. 3.1, it can be expressed as follows:

$$\sum_k \dot{m}_i - \sum_k \dot{m}_e = \frac{dm_{cv}}{dt}, \tag{3.1}$$

here, m represents the mass, and $\dot{m}$ denotes the mass flow rate. The subscripts i and e correspond to the inlet and exit of the control volume, respectively, while the subscript cv refers to the control volume itself.

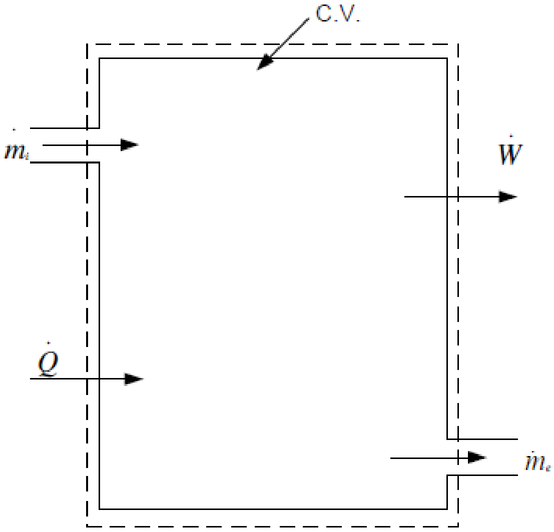

Fig. 3.1. Control volume of mass balance

The energy principle for a control volume addresses all energy components within a selected control volume. The conservation of energy principle, also known as the first law of thermodynamics, where the net rate of energy transferred by heat reduce by the net rate of energy transferred out by work with the addition of net rate of energy transfer into the control volume accompanying mass flow equal with time rate of change of energy contained within control volume or can be stated as follows:

$$\dot{Q} - \dot{W} + \sum_i \dot{m}_i \left(h_i + \frac{V_i^2}{2} + gz_i\right) - \sum_e \dot{m}_e \left(h_e + \frac{V_e^2}{2} + gz_e\right) = \frac{dE_{cv}}{dt} \tag{3.2}$$

In this context, E represents the energy, $\dot{Q}$ is the heat transfer rate, $\dot{W}$ refers to power, and t is time. The additional symbols include h for specific enthalpy, V for velocity, g for gravitational acceleration, and z for elevation.

Entropy generation is related to the inefficiencies or losses within a system. The entropy generated during a process is referred to as entropy generation, denoted by $\dot{S}_{gen}$. The entropy generation rate for control volumes can be defined as:

$$\sum_k \dot{m}_e s_e - \sum_k \dot{m}_i s_i - \sum_k \frac{\dot{Q}_k}{T_k} + \frac{dS_{cv}}{dt} = \dot{S}_{gen,} \tag{3.3}$$

where S is the entropy and s is the specific entropy (J/kg.K).

Unlike energy, exergy is not conserved. Exergy is defined as the maximum amount of useful work that can be extracted from a system at a given state. To understand exergy, it is essential to first define reversible work, which is the maximum useful work obtainable when a system undergoes a process between two specific states. Another key concept in exergy analysis is exergy destruction, which refers to the potential work lost due to irreversibilities in the process. The exergy balance for a control volume system can be expressed as follows:

$$\sum_j \dot{Q}_j \left(1 - \frac{T_0}{T_J}\right) - \left(\dot{W}_{cv} - p_0 \frac{dV_{cv}}{dt}\right) + \sum_e \dot{m}_e ex_e - \sum_e \dot{m}_e ex_e - \dot{Ex}_d = \frac{dEx_{cv}}{dt}, \tag{3.4}$$

where T, p, V, ex and $\dot{Ex}_d$ are, temperature, pressure, volume, specific exergy, and rate of exergy destruction, respectively. The subscript j is the property value at state j and the subscript 0 is the value of a property at the surrounding. The physical exergy, ex^{ph}, at a given state is defined as:

$$ex^{ph} = (h - h_0) - T_0(s - s_0) + \frac{V^2 - V_0^2}{2} + g(z - z_0). \tag{3.5}$$

3.1.2. Energy and exergy efficiency

Energy efficiency is a measure of the useful energy output of a system relative to the input energy supplied to it. The energy efficiencies of various systems are defined in the following sections. Specifically, the thermal efficiency of a thermal cycle is defined as:

$$\eta_{cycle} = \frac{\dot{W}_{cycle}}{\dot{Q}_i} = 1 - \frac{\dot{Q}_e}{\dot{Q}_i} \tag{3.6}$$

The isentropic thermal efficiency of work-producing devices is defined as:

$$\eta_{is} = \frac{\dot{W}_{ac}}{\dot{W}_{is}} \tag{3.7}$$

On the other hand, the isentropic thermal efficiency of work-consuming devices is defined as:

$$\eta_{is} = \frac{\dot{W}_{is}}{\dot{W}_{ac}} \tag{3.8}$$

The performance of refrigerators is known as the coefficient of performance (COP). It is defined as:

$$COP_R = \frac{desired\ output}{required\ input} = \frac{Q_L}{Q_H - Q_L} = \frac{1}{\frac{Q_H}{Q_L} - 1}, \tag{3.9}$$

where the subscripts *is*, *ac*, *R*, *H*, and *L* indicate isentropic, actual, refrigerator, high temperature reservoir, and low temperature reservoir, respectively.

Exergy efficiency is defined as the ratio of the actual thermal efficiency of a system to the maximum possible (reversible) thermal efficiency under the same conditions. More broadly, exergy efficiency can be expressed as:

$$\psi = \frac{exergy\ recovered}{exergy\ supplied} = 1 - \frac{exergy\ destroyed}{exergy\ supplied} \tag{3.10}$$

The exergetic efficiencies of different systems are defined as follows. For heat engines the exergetic efficiency is defined as:

$$\psi = \frac{\eta_{thermal}}{\eta_{rev}} \tag{3.11}$$

The exergetic efficiency of work-producing devices is defined as:

$$\psi = \frac{\dot{W}_{cv}}{\dot{W}_{rev}} = \frac{\dot{W}_{cv}}{\dot{E}x_i - \dot{E}x_e} \tag{3.12}$$

For heat exchanger, the exergetic efficiency is defined as:

$$\psi = \frac{\dot{E}x_{cold,e} - \dot{E}x_{cold,i}}{\dot{E}x_{hot,i} - \dot{E}x_{hot,e}} \tag{3.14}$$

In this study, Exergy analysis in power-based units (kW) is essential for evaluating ORC systems in geothermal, solar, and biomass applications. Geothermal ORC utilizes medium-temperature heat (90–250°C) with exergy destruction mainly in the evaporator (~40-50%), achieving an efficiency of 25–40% (Bhao and Zhao, 2013). Solar ORC, powered by concentrated or flat-plate collectors (80–300°C), suffers high exergy losses (~50-60%) in the collector, leading to lower efficiency (10–35%) due to intermittent heat supply (Thanche et al., 2011). Biomass ORC, operating at 150–600°C, has significant combustion losses (~40-50%) but offers flexibility, with 15–35% efficiency (Orosz et al., 2010). Among these, geothermal ORC provides continuous power, solar ORC is best for daytime operation, and biomass ORC is suited for standalone or hybrid applications.

3.2. ORC utilization from excess steam Tura GPP

In Hungary itself, geothermal utilization for electricity utilization has been implemented in Tura region (30 km east of Budapest) and it is become the first geothermal plant in Hungary that producing electricity. The design temperature of power plant is about 123-126 °C with 86 kg/s (reservoir temperature) with outflow temperature 122-125 °C total production capacity is 2.7 MW, and the excess hot water of the field is around 75-78 °C (Boda, 2016). The low-medium temperature of excess hot water from the field is still have a high amount of enthalpy that can be utilised for generating electricity. However, these moderate and low-medium temperature heat sources cannot be efficiently converted into electricity through the conventional steam Rankine cycle. The ORC has been considered as most feasible cycle to generating electricity while recovering various heat sources. The ORC is same as the conventional Steam but uses low boiling temperature of organic fluids or refrigerants instead of water. In this sub-chapter, evaluation of thermodynamic performance from the exhaust heat of the Tura geothermal power plant will be performed using ORC application in term of energy, exergy, and exergy sustainability aspect.

Fig. 3.2a shows a simple schematic of an ORC consisting of an evaporator, turbine, condenser and pump. The heat source used for the ORC process comes from the heat of the Tura geothermal plant injection. This heat is extracted by a heat exchanger and heat transfer occurs with the working fluid which depends on its thermo-physical properties and usually have a low boiling temperature. The first and second laws of thermodynamics can be used to determine the performance of the ORC. The amount of work generated and the heat required by the ORC can be determined by the energy equilibrium equation. The equations in each component are shown in Table 3.1.

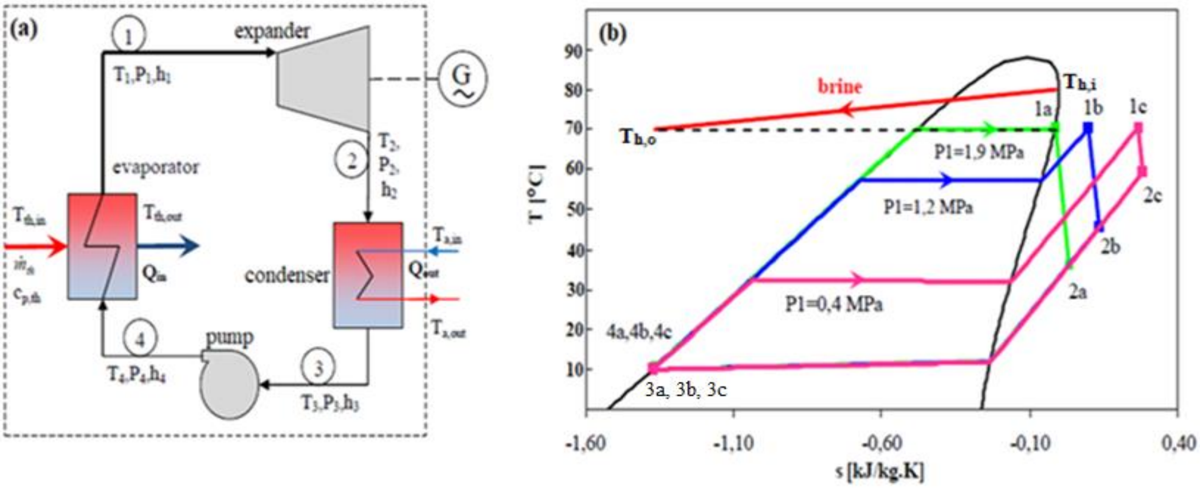

Fig. 3.2. The ORC based on excess steam geothermal: a) schematic, b) T-s diagram

Table 3.1. Governing equations for energy and exergy balance in ORC components

Components	Energy balance	Exergy balance
Pump	$\dot{W}_{pump} = \frac{\dot{m}(h_4 - h_3)}{\eta_{pump}},$	$\dot{E}_{X3} + \dot{W}_{pump} = \dot{E}_{X4} + \dot{E}_{Dpump}$
Evaporator	$\dot{Q}_{evap} = \dot{m}(h_1 - h_4),$	$\left(1 - \frac{T_0}{T_{in}}\right) + Q_{in} + \dot{E}_{X4} = \dot{E}_{X1} + \dot{E}_{Devap},$
Expander	$\dot{W}_{exp} = \dot{m}(h_1 - h_2)\,\eta_{exp},$	$\dot{E}_{X1} = \dot{E}_{X2} + \dot{W}_{exp} + \dot{E}_{Dexp},$
Condenser	$\dot{Q}_{cond} = \dot{m}(h_2 - h_3),$	$\dot{E}_{X2} = \dot{E}_{X3} + \dot{E}_{Dcondenser}$
Efficiency	$\eta_{thermal} = \frac{\dot{W}_{net}}{\dot{Q}_{evap}}$	$\psi_{system} = \frac{\sum \dot{W}_{ORC}}{\dot{E}_{Xin}}$

where, $\dot{W}_{exp}, \dot{W}_{pump}$ are power of expander and pump respectively, while $\dot{m}$ is mass flow rate (kg/s), h is specific enthalpy (kJ/kg), and $\dot{Q}_{in}$, $\dot{Q}_{out}$ are the heat enters and exit from the system. The equations inside Table 3.1 are valid in the ideal condition, where all losses arisen are ignore. In actual conditions many losses occur including an increasing entropy in the compression and expansion process. In this study, the isentropic efficiency for expander (η_{exp}) is set up at 80% and for pump (η_{pump}) is 90%.

The isentropic efficiency for expander is defined as:

$$\eta_{exp} = \frac{h_1 - h_2}{h_1 - h_{2s}}, \tag{3.15}$$

The isentropic efficiency for pump is defined as:

$$\eta_{pump} = \frac{h_{4s} - h_3}{h_4 - h_3}, \tag{3.16}$$

where h_1 and h_2 is the specific enthalpy of the fluids at inlet and outlet expander, respectively. while h_{2s} is the specific enthalpy of the fluids at exit expander for isentropic proses. For the calculation of work pump that delivered cooling water to the heat exchanger is initialize by Eq. (3.17), where γ is specific weight (N/m^3), $\dot{V}$ is volumetric flow rate (m^3/s), g is the acceleration of gravity (9.8 m/s^2) and H is the pump head.

$$\dot{V}H = \dot{m}_w \, g \, H, \tag{3.17}$$

The Eq. (3.17) is known as the theoretical pump performance ($\dot{W}_{pwt}$) or it can be written in Eq. (3.18):

$$\dot{W}_{pwt} = \dot{m}_w \, g \, H. \tag{3.18}$$

Meanwhile, for the efficiency of the cooling water pump can be written in Eq (3.19):

$$\eta_{pw} = \frac{\dot{W}_{pwt}}{\dot{W}_{pw}}. \tag{3.19}$$

To get the actual work of the water-cooling pump, it is obtained by using the equation of:

$$\dot{W}_{pw} = \frac{\dot{m}_w \, g \, H}{\eta_{pw}}, \tag{3.20}$$

and for the mass flow rate of cooling water is shown by the Eq. (3.21):

$$\dot{m}_w = \frac{\dot{m} \, (h_2 - h_3)}{c_p (T_{w7} - T_{w6})}. \tag{3.21}$$

Optimum conditions are crucial in ORC analysis, in case of generally ORC has a low efficiency. According to Wei et al., (2007) maximum output power will be obtained by utilization the remaining heat as much as possible. The excess steam temperatures and cooling water temperatures are standard value for cutting edge of medium-enthalpy geothermal applications (Nusiaputra et al., 2015).

Exergy analysis is not only to measure how much energy is available in a system but can be used to improve the performance of both the economic and environmental aspect. Furthermore, in this study the role of exergy as a method to measure the sustainability of a process and system is used. Some researchers call it the exergy sustainability index (ESI) or the thermo-sustainability index (TSI). ESI is also a powerful parameter among other indicators. It accesses the degree of sustainability, and it can be derived from the respective exergy balanced equations for each cycle and investigated of ESI are presented by Eqs. (3.22-3.24) (Aydin, 2013).

Exergy waste ratio:

$$EWR = \frac{Overall\ exergy\ waste}{overall\ exergy\ input}, \tag{3.22}$$

Overall exergy efficiency:

$$\psi_{overall} = \frac{\dot{E}_{Xout}}{\dot{E}_{Xin}}, \tag{3.23}$$

Environmental effect factor (EEF):

$$EEF = \frac{Waste\ exergy\ ratio}{Exergy\ efficiency}, \tag{3.23}$$

Exergy sustainability index (ESI):

$$ESI = \frac{1}{Environmental\ effect\ factor}. \tag{3.24}$$

In Fig. 3.2b, it can be seen the upper limit and the lower limit of the cycle is at temperature 68 °C and 10 °C respectively. However, in this study, the national of institute standard and technology (NIST) Refprop database are used determine properties of each working fluids (see Table 2.2). The inlet turbine temperature of ORC is kept constant at 68 °C, which is the temperature limit is still below the limit of injection temperature to the reservoir (70 °C), to avoid cross temperature in the evaporator. The evaporator pressure is varied as we can see at Fig. 3.2b, with the purpose is to discover the optimum condition of the cycle that produce the highest power and efficiency. The summary of the parameters, constraints and assumptions that will be used in this ORC analysis, is presented in Table 3.2.

Table 3.2. Parameter setting

ORC process parameters	**Unit**	**Set- value**
Evaporator temperature (T_{evap})	°C	68
Condenser temperature (T_{cond})	°C	10
Pump efficiency (η_{pump})	%	90
Expander efficiency (η_{exp})	%	80
Temperature difference (ΔT_{evap})	°C	10
Mass flow rate ($\dot{m}$)	kg/s	1
Geothermal fluid parameters		
Excess temperature ($T_{h,i}$)	°C	80
Injection temperature ($T_{h,o}$)	°C	70
Evaporator pressure (P_{evap})	MPa	2-3
Temperature at dead state (T_0)	°C	5
Pressure at dead state (P_0)	MPa	0.101325

3.3. Solar ORC systems

3.3.1. The theoretical approach of the solar ORC integrated with PCM

In terms of solar energy resource potential, Central-European such as Hungary has a daily total of around 3.2 to 3.6 kW.h/m^2 and a yearly total is about 1168 to 1314 kW.h/m^2, and can be seen in Fig. 3.3. These numbers distinguish Hungary as having a relatively high potential for solar energy use. This makes it a suitable location for installing solar thermal collectors with an ORC system. In solar thermal applications, the two main subsystem components are solar collectors and heat storage. In solar thermal applications, a solar collector is the component that transforms solar irradiation energy to heat energy via a working fluid, a strong optical performance is essential to absorb as much heat as possible. The heat transported by the working fluid can be used to TES systems or to provide residential hot water (Hossain et al., 2011; Tian and Zhao, 2013).

It was mentioned before that the Solar-ORC is unable to operate all day long, TES can support the system by storing excess heat during the day hours and using it during the night time or low solar irradiation (Habibi et al., 2021; Pourmoghadam et al., 2021). TES systems are classified into sensible, latent, and thermochemical storage. Latent storage is known as PCM storage (Tiari et al., 2021). We propose evaluating the variety of TES media used in a domestic solar-ORC system, focusing only on the prediction of sizing PCMs as storage media. The selection of optimum storage temperatures that maximise the solar-ORC system's total to solar-to-electric conversion efficiency is being examined in Gödöllő, Hungary, where research for solar-ORC still needs to be improved. It is essential. To ensure the optimum fit between the systems' electrical outputs and the residential seasonal load profiles in the individual locales, the needed TES volumes and system operational methods are also examined.

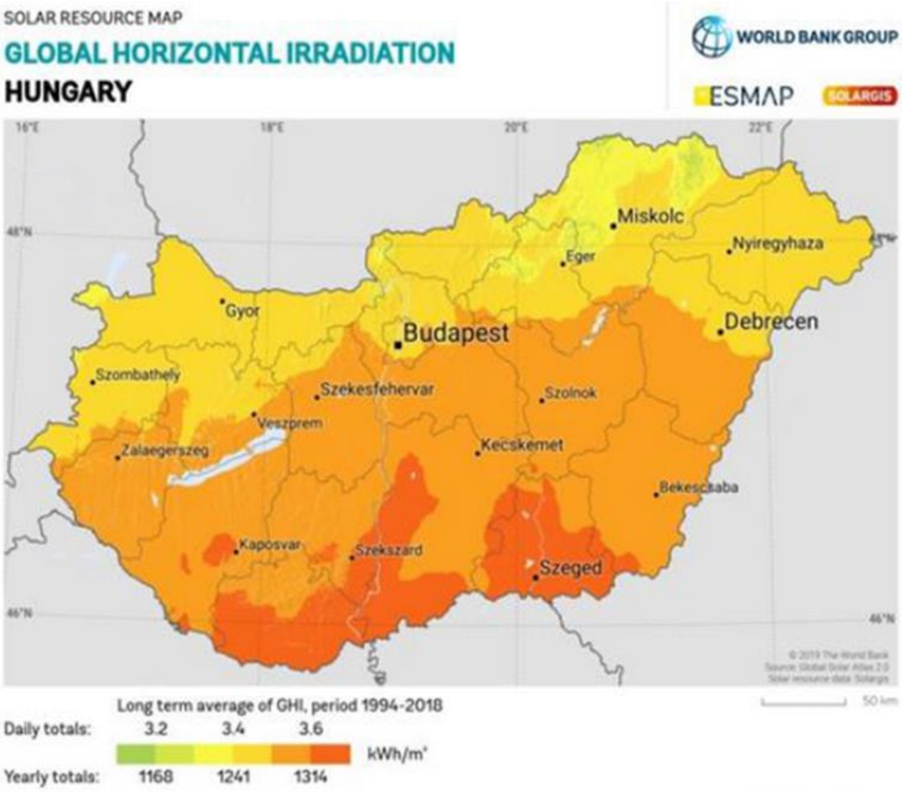

Fig. 3.3. Global solar irradiation (GSI) in Hungary (Solargis, 2021a)

Fig. 3.4a shows the solar irradiation on average and peak days in Gödöllő for each month of the year. It can be seen that the average solar irradiation is more plentiful and varies less on a daily and seasonal timeframe than maximum one. It can be seen also that August is the peak for both the maximum and the average of global solar irradiation, with around 507 and 316.9 W.h/m^2, respectively. Therefore, this study chose June as the month to use as simulation data.

Fig. 3.4b shows the characteristics of the daily average of global solar irradiation and the ambient temperature. The plot confirms that both characteristics (Gb and T_{amb}) have different peak values of the time. For solar irradiation, the maximum value happens around 9-10 o'clock, around 447 W.h/m^2, while the highest ambient temperature happens around 16-17 o'clock with a temperature of around 304 K. It happens due to the accumulation that occurs during solar irradiation at the last time to make the ambient temperature rise at the end of daylight. Therefore, for the solar collector, the current research looks at two types of non-concentrating collectors: (1) a new generation of high-performance evacuated flat-plate collector (EFPC) explicitly designed for medium-temperature process-heating applications (including ORC systems), and (2) a standard, lower-cost evacuated-tube heat-pipe collector (ETC) designed for low-temperature domestic hot water (DHW) heating applications, and (3) parabolic tube collector (PTC).

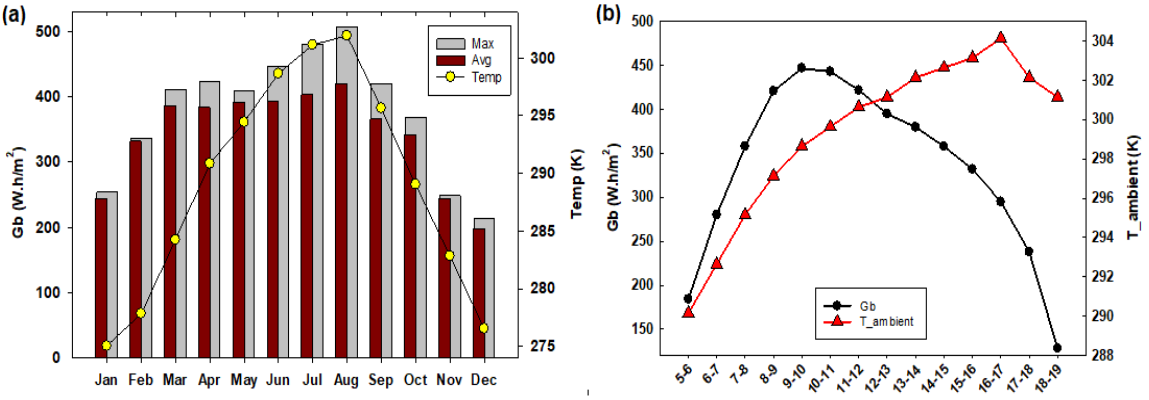

Fig. 3.4. Characteristic solar irradiation in Gödöllő: a) annually, b) daily

According to an experiment by Alshibil et al., (2022), the collector array is designed to be south-facing, with a 30° inclination angle facing south for maximum thermal power and electrical output. The solar-collector array is modelled as functioning under quasi-steady state circumstances, with the collectors' thermal capacity ignored. The sizing calculations assume that the collector sub-system is only active during the hours when the solar incidence angle on the solar collector plane is 30°.

The solar-collector array's performance is predicted using hourly climatic data for Gödöllő in June 2021. A steady-state efficiency equation is used simulation (Freeman et al., 2017):

$$\frac{\dot{Q}_u}{A_{sc}} = \eta_0 K_\theta G_b - C_1(T_h - T_a) - C_2(T_h - T_a)^2, \tag{3.25}$$

where is η_0 the zero-loss optical efficiency, C_1 and C_2 are heat loss coefficients, and K_θ are incident angle modifier (IAM) factors applied to the zero-loss efficiency for the beam and diffuse components of the solar irradiance (G_b), respectively. By assuming that the outlet fluid temperature ($T_{h,o}$) is equal to the temperature of the lumped/uniform TES temperature (T_{TES}) and its expressed by Eq. (3.26):

$$T_{h,o} = T_{TES}. \tag{3.26}$$

In Table 3.3, the values of the parameters are given. The solar collector useful heating product (Q_u) is found by using the following equation:

$$\dot{Q}_u = \dot{m}_{col}\, c_p\left(T_{h,o} - T_{h,i}\right), \tag{3.27}$$

where the collector mass flow rate ($\dot{m}_{col}$), the specific heat capacity of the fluid (c_p) and the temperature levels of the solar collector, inlet ($T_{h,i}$) and outlet ($T_{h,o}$) are used in Eq. (3.27) for the useful heat production calculation.

Table 3.3. Curve parameters of different solar collectors related to efficiency (Bellos and Tzivanidis, 2019; Freeman et al., 2017)

	EFPC	**ETC**	**PTC**
Model	TVP Solar HT-Power	Thermomax HP-200	PTC-1000
η_0	0.774	0.556	0.761
c_1 (W/m^2.K)	0.376	0.888	0.22
c_2 (W/m^2.K^2)	0.006	0.006	0.000503
A_{sc} (m^2)	1.84	2	1.8

Fig. 3.5a depicts the Solar-ORC cycle consisting of a solar collector, water pump, evaporator, turbine, condenser, and pump. Heat transfer occurs in the boiler between hot steam and working fluid or organic fluid with a low boiling temperature, causing the working fluid to change phase into steam vapour, which has sufficient temperature and pressure to turn the turbine and the rotation to be converted into electricity by the generator. Meanwhile, A and B represent the ORC and the water circuits, respectively. The cycle model and parameters used for the thermodynamic analysis of the ORC system are shows in Fig. 3.5c. R245fa and R123 were chosen as working fluids according to their properties and the low value of ODP and GWP, and the details are shown in Table 2.2. The first and second law of thermodynamics should be applied to determine the performance of the ORC. The energy equilibrium equation may be used to calculate the quantity of work generated and the heat required by the ORC.

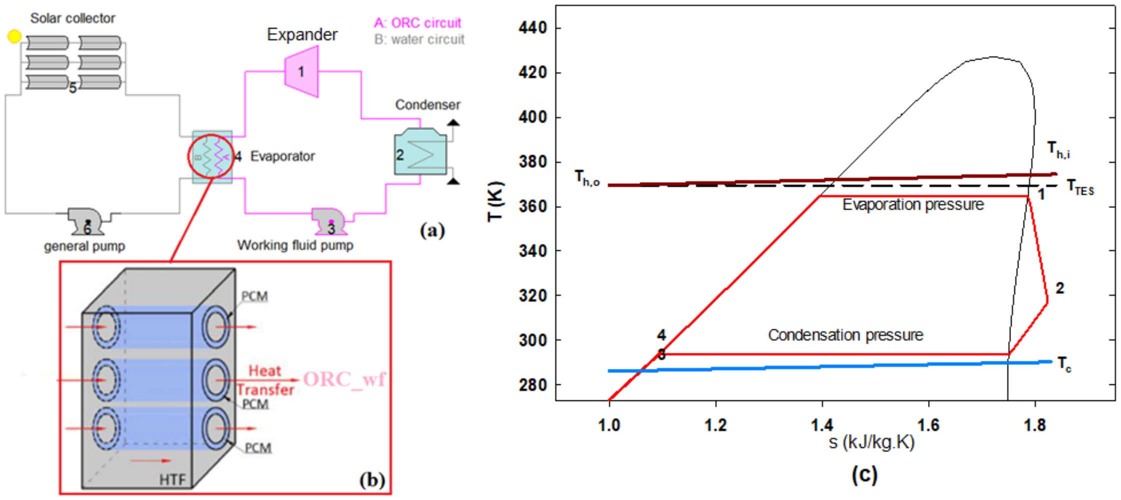

Fig. 3.5. Solar-ORC: a) schematic, b) TES location, c) T-s diagram

The formulas for each component are as follows in Table 3.4. Where ψ_{system} is the exergy efficiency of the whole system (see Table 3.4). $\dot{E}x_{in}$ is the inlet exergy to the system, $\dot{E}x_{Solar}$ is the maximum useful exergy gained by the solar radiation, which T_{su} is the solar surface temperature, which is assumed 5800 K. Therefore, the exergy destruction for each ORC's component is shown also in Table 3.4.

Table 3.4. Solar-ORC governing equations

Components	**Energy balance**	**Exergy balance**
Pump	$\dot{W}_{pump} = \frac{\dot{m}(h_1 - h_2)}{\eta_{pump}},$	$\dot{W}_{pump} = \dot{E}_{X1} - \dot{E}_{X2} + \dot{E}_{D\_pump}$
Evaporator	$\dot{Q}_{evap} = \dot{m}(h_4 - h_3),$	$\dot{E}_{D\_evap} = \left(1 - \frac{T_0}{T_{in}}\right)Q_{in} + \dot{E}_{X3} - \dot{E}_{X4},$
Expander	$\dot{W}_{exp} = \dot{m}(h_4 - h_5)\,\eta_{exp},$	$\dot{E}_{D\_exp} = \dot{E}_{X4} - \dot{E}_{X5} - \dot{W}_{exp},$
Condenser	$\dot{Q}_{cond} = \dot{m}(h_6 - h_1),$	$\dot{E}_{D\_cond} = \dot{E}_{X6} - \dot{E}_{X1} - \dot{Q}_{cond},$
Solar collector	$\frac{\dot{Q}_u}{A_{sc}} = \eta_0 K_\theta G_b - C_1(T_h - T_a) - C_2(T_h - T_a)^2$	$\dot{E}x_{Solar} = A_{ap}G_b\left[1 + \frac{1}{3}\left(\frac{T_0}{T_{su}}\right)^4 - \frac{4}{3}\left(\frac{T_0}{T_{su}}\right)\right]$
Efficiency	$\eta_{thermal} = \frac{\dot{W}_{net}}{\dot{Q}_{evap}}$	$\psi_{system} = \frac{\sum \dot{W}_{ORC}}{\dot{E}_{Xin}}$

In the Table 3.4 $\dot{E}_{Dturbine}, \dot{E}_{Dcondenser}, \dot{E}_{Devap}, \dot{E}_{Dpump}$ denote as the destruction of exergy in turbine, condenser, pump and evaporator, respectively. After determining the exergy flows, the energy input, exergy output, consumed energy, available exergy, and exergy destruction may be estimated using the definitions in Table 3.4. The performance of the components and systems may then be assessed using the parameters specified below. The exergy efficiency is thus defined as $\psi_{total} = {Ex_{use}^{total}}/{Ex_{avai}^{total}}$. Additional indicators of interest include (1) the degree of thermodynamic perfection, $v_{total} = {Ex_{in}^{total}}/{Ex_{out}^{total}}$; and (2) the influence coefficient $\beta = {Ex_{ava}}/{Ex_{ava,sys}}$, which represents the proportion of exergy that is not destroyed and the fraction of the entire system's available exergy that is associated with a specific component, respectively.

All calculations in this work employ a lumped model for the TES vessel, assuming constant temperature and ignoring thermal losses to the environment. When PCMs are used as storage medium, the thermal store is programmed to start each day in a completely discharged (solidified) condition. Therefore, Physical phenomena (e.g., thermal or chemical phenomena), heat kinds (e.g., sensible, latent, etc.), and a storage medium describe the many types of TES materials (e.g., liquid, solid, solid–gas, liquid–gas, solid-liquid, etc.). Table 3.5 shows that the material's specific heat capacity, which fluctuates with temperature, determines the TES feature. Differential scanning calorimetry (DSC) may be used to determine TES material's specific heat capacity.

Table 3.5. The properties of selected TES materials (Douglas and Dever, 1955; Pan et al., 2016; Pcmproduct, 2013)

TES materials	**T (K)**	**C_0 (J/kg.K)**	**C_1 (J/kg.K)**	**References**
Monel metal	273.15 – 573.15	422.867	0.1842	Douglas & Dever.,1955
SS 446	273.15 – 773.15	451.337	0.4497	Douglas & Dever.,1955
Chrome brick	293.15 – 1973.15	800	0.3	Kostowski, E. 2010
Concrete	300 – 600	957.55	0.3403	Pan et al., 2017
Chamote brick	293.15 – 1623.15	880	0.23	Kostowski, E. 2010
Magnesite brick	293.15 – 1923.25	1050	0.3	Kostowski, E. 2010
Organic PCM	273.15 - 440.15	2270	-	Pcmproduct, 2013

Eq. (3.28) is the generic polynomial equation for the specific heat capacity of materials, which is used to calculate the stored thermal energy in equation is expressed by eq (3.28) (Daniarta et al., 2022):

$$C_{ST} = C_0 + C_1 T_1 + C_2 T_2 + \cdots + C_n T_n, \tag{3.28}$$

$$Q_{ST} = V_{ST} \rho C_{ST} \Delta T_{1-4}, \tag{3.29}$$

where C, T, Q, V, ρ, and T indicate, specific heat capacity, temperature, heat, volume, density, and temperature difference. Meanwhile, subscript $_{ST}$ represents the storage.

Assuming that the heat transfer rate during TES device discharging was the same as that of the TES-evaporator (Eq. (3.30)), the efficiency of the stored thermal energy and the charging-discharging period may be computed using by Eqs. (3.31-3.34) as follows:

$$\dot{Q}_{DC} = \dot{Q}_{HE}, \tag{3.30}$$

$$\eta_{ST} = \eta_{CH}\eta_{DC}\frac{Q_{ST}}{\int \dot{Q}_{CH}dt}\frac{\int \dot{Q}_{DC}dt}{Q_{ST}}, \tag{3.31}$$

$$\tau_{CH} = \frac{Q_{ST}}{\dot{Q}_{CH}}, \tag{3.32}$$

$$\tau_{DC} = \frac{Q_{ST}}{\dot{Q}_{DC}}, \tag{3.33}$$

$$\zeta(T) = \frac{m_{ST}}{m_{wf}} = \frac{(h_1 - h_4)}{c_{ST}(T_{ST})|_{T_{ST2}}^{T_{ST1}}(T_{ST1} - T_{ST2})}, \tag{3.34}$$

where τ is the charging/discharging times, m_{ST} is the storage mass (kg), the *CH* and *DC* subscripts reflect charging and discharging operations. As an evaluation parameter, the dimensionless mass parameter (ζ(T)) of TES material may be utilised for sizing the TES employed for solar thermal. Notably, the organic PCM attributes provided for PCMs represent a typical spectrum of commercially accessible organic aliphatic molecules and inorganic hydrated salt products.

Table 3.6 shows the selected organic PCM materials for this study based on the material's melting temperature and solid-liquid phase according to the T_{in} and T_{out} of evaporator. Mostly, paraffin is a saturated hydrocarbon family, and the longer the length of the hydrocarbon chains, the higher the melting temperature (Su et al., 2015). Paraffin is a relatively safe, dependable, low-cost, non-corrosive substance with a low vapour pressure. Nonetheless, some paraffin compounds have unfavourable thermal and chemical characteristics, such as low heat conductivity, flammability, and a significant volume change during the phase shift (solid-liquid) and are incompatible with plastic. Alcohol, fatty acids, and glycols are examples of non-paraffin PCMs. In comparison to paraffin, several non-paraffin compounds are readily synthesised from vegetable and animal oils (Romdhane et al., 2020) and have higher melting, crystallisation, and heat of fusion temperatures (Pielichowska and Pielichowski, 2014).

Table 3.6. The selection of solid-liquid of organic (Lingayat and Suple, 2013; Sharma et al., 2009; Su et al., 2015)

No	**PCM name**	**Classification**	**T_m (K)**	**h_m (kJ/kg)**	**k (W/m K)**	**ρ (kg/m³)**	**c_p (kJ/kg K)**
1	N-Hexacone	Paraffin	329.45	255	n.a	n.a	2.37 (Liquid) 1.80 (solid)
2	Heptadecanoic acid	Non-paraffin	333.75	189	n.a.	853 (298.15 K)	1.76 (solid, 298.15 K)
3	N-Octacosane	Non-paraffin	334.15	134	n.a.	n.a.	2.37 (liquid, 353 K)
4	P-Bromophenol	Non-paraffin	336.65	86	n.a.	1840 (298.15 K)	1.11 (solid, 300 K)
5	n-Triacontane	Paraffin	339.15	-	n.a.	n.a.	1.32 (solid, 300 K)

No	PCM name	Classification	T_m (K)	h_m (kJ/kg)	k (W/m K)	ρ (kg/m^3)	c_p (kJ/kg K)
6	Durene	Non-paraffin	352.45	156	n.a.	838	2.05 (liquid, 353 K), 1.52 (solid, 298.15 K)
7	Acetamide	Fatty acids	354.15	241	n.a.	1159	1.47 (solid, 298.15 K)
8	D-sorbitol	Sugar alcohols	370.15	185	n.a.	1520 (solid)	1.32 (solid, 298.15 K)

3.3.2. Utilization of ORC integrated with PCMs in equator country condition

The average climatic conditions in equator country such as Indonesia especially in Bandung throughout the year reveal that its average solar irradiation is more consistent and abundant on both daily and monthly scales compared to the maximum solar irradiation. August stands out as the peak month for both maximum and average global solar irradiation, with values of approximately 150 kWh/m^2 and 70 kWh/m^2, respectively (Fig. 3.6a). Additionally, the sunshine duration in August exceeds 6 hours, contributing to a higher temperature increase compared to other months, with a maximum temperature of 26 °C and a daily average of 23 °C (Fig. 3.6b). For this study, data from January, April, and June 2021 will be utilized.

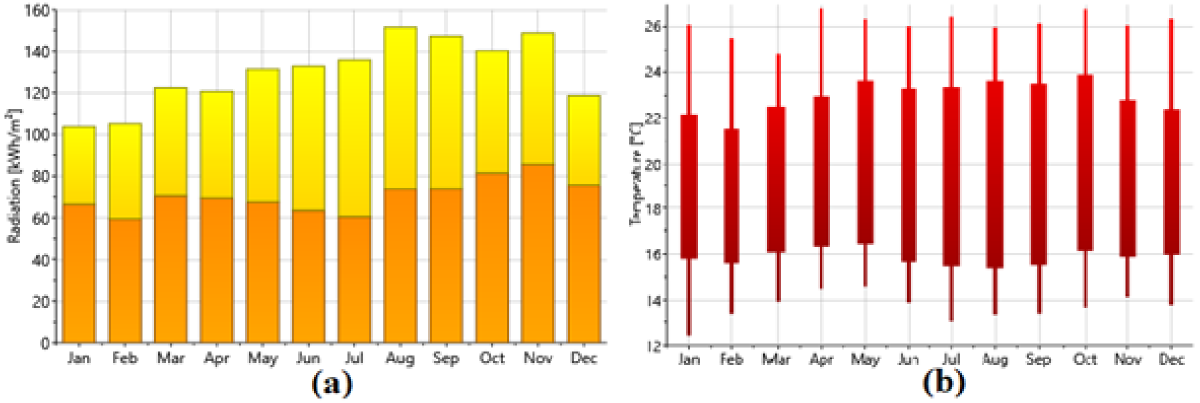

Fig. 3.6. The weather condition in Bandung (Indonesia) in 2021 (Solargis, 2021b)

In the solar thermal system, according to the previous subsection (see Fig. 3.5), the PTC designed for low/medium-temperature DHW heating utilization. According to an experiment done by Setiawan et al. (2017), where according their theoretical analysis results, Indonesia has low decent solar arrays both solar-PV and collector tilt intersection with values of 11°-15°. The solar collector line-up is assumed to operate in a quasi-steady state, with the collectors' thermal capacity neglected. In the volume-sizing calculations, it is assumed that the solar collector subsystem is only operational during the day-hours when the solar incidence angle on the collecting array is 15°.

The solar-collector array's performance is predicted using hourly climatic data for Bandung in June 2021. A steady-state efficiency equation is used to simulate the collectors (Freeman et al., 2017):

$$\frac{\dot{Q}_u}{A_{sc}} = \eta_0 K_\theta G_b - C_1(T_h - T_a) - C_2(T_h - T_a)^2, \qquad (3.35)$$

where is η_0 the zero-loss optical efficiency, C_1 and C_2 are heat loss coefficients and K_θ are incident angle modifier (IAM) factors applied to the zero-loss efficiency for the beam and diffuse components of the solar irradiance (G_b), respectively.

Eq. (3.35) applies to both steady and transient assumptions. When a steady state is assumed for the problem, average values for time-varying parameters are investigated (Arkar and Medved, 2015). A numerical approach is frequently used to determine the transient rate of solar thermal energy collection for computations that rely on a transitory assumption (Calise et al., 2019; Hertel et al., 2020). In this way, the entire modelling period is broken into short time periods. Momentary values are then produced for time-dependent parameters such solar irradiance, incidence angle, and ambient temperature (Buonomano et al., 2013). As a consequence, a time-dependent profile for the solar thermal energy collection rate will be constructed, allowing the total amount of collected solar thermal energy to be determined in the next phase. While, according to experimental analysis done by (Bellos et al., 2020), they are using ETC with Thermomax HP-200 with the acentric area (A_{sc}) of ETC is 1.85 m^2 and they got the value of each the parameter of η_0, c_1 and c_2 are 0.556, 0.888 ($W/m^2.K$), and 0.006 ($W/m^2.K$), respectively. In this study, the authors use three ETC setup (~5.5 m^2) with the assumption the solar collector will be produce high enough of value heating product (Qu) that can produce the electricity around 500 Watt.

The HTF temperature ($T_{h,o}$) is equal to the melting TES tank temperature(T_{TES}), Eq. (3.36) is presented by:

$$T_{h,o} = T_{TES} \tag{3.36}$$

From the ETC equations and parameters that have been given, the next equation is to calculate the solar collector useful heating product (Q_u):

$$\dot{Q}_u = \dot{m} C_p \left(T_{h,o} - T_{h,i}\right) \tag{3.37}$$

The ORC's performance should be determined using the first and second laws of thermodynamics. The energy equilibrium equation may be used to compute the amount of work produced and heat required by the ORC. The formula for each component is as follows (Table 3.7):

Table 3.7. Solar-ORC governing equations

Components	**Energy balance**	**Exergy balance**
Pump	$\dot{W}_{pump} = \frac{\dot{m}(h_1 - h_2\ )}{\eta_{pump}},$	$\dot{W}_{pump} = \dot{E}_{X1} - \dot{E}_{X2} + \dot{E}_{D\_pump}$
Evaporator	$\dot{Q}_{evap} = \dot{m}(h_4 - h_3),$	$\dot{E}_{D\_evap} = \left(1 - \frac{T_0}{T_{in}}\right) Q_{in} + \dot{E}_{X3} - \dot{E}_{X4},$
Expander	$\dot{W}_{exp} = \dot{m}(h_4 - h_5)\, \eta_{exp},$	$\dot{E}_{D\_exp} = \dot{E}_{X4} - \dot{E}_{X5} - \dot{W}_{exp},$
Condenser	$\dot{Q}_{cond} = \dot{m}(h_6 - h_1),$	$\dot{E}_{D\_cond} = \dot{E}_{X6} - \dot{E}_{X1} - \dot{Q}_{cond},$
Solar collector	$\frac{\dot{Q}_u}{A_{sc}} = \eta_0 K_\theta G_b - C_1(T_h - T_a) - C_2(T_h - T_a)^2$	$\dot{E}x_{Solar} = A_{ap} G_b \left[1 + \frac{1}{3}\left(\frac{T_0}{T_{su}}\right)^4 - \frac{4}{3}\left(\frac{T_0}{T_{su}}\right)\right]$
Efficiency	$\eta_{thermal} = \frac{\dot{W}_{net}}{\dot{Q}_{evap}}$	$\psi_{system} = \frac{\sum \dot{W}_{ORC}}{\dot{E}_{Xin}}$

The approach temperature differences of 5 K at the working-fluid output and a heat source temperature equal to that of the TES tank temperature:

$$T_1 = T_{TES} - 5\ K, \tag{3.38}$$

and a cold-reservoir temperature equal to the maximum feasible ambient air temperature:

$$T_3 = T_{c,i} + 5\ K, \tag{3.39}$$

where, the evaporator gets at least 5 K of superheating, whilst the condenser assumes the working fluid leaves in a saturated liquid state (subcooling state). Both the ORC isentropic efficiency pump (η_{pump}) and isentropic efficiency expander (η_{exp}) are 65% and 70%, respectively.

This section will look at two scaling alternatives for the solar-ORC and the TES, both of which use PCMs as storage medium. First strategy is based on a partial-storage which TES is used to reservoir fluctuations in solar irradiation, so the ORC system may operate at its design point for a longer period of time, escaping in periodic and part-load conditions induced by variations in heat input. The ORC engine will be assumed to run during the day-hours, which are defined as the hours when the solar incidence angle on the slanted collector plane is 15° (between 06:00 and 17:00). The ORC system is therefore scaled for the average solar-heat input throughout the core day-hours, whilst the required volume of PCM is calculated as the distinction between the average solar-thermal gain ($Q_{u,avg\ day}$) and the peak solar day ($Q_{u,peak\ day}$) for each periodical (Freeman et al., 2017):

$$\dot{m}_{r,ps} = \frac{Q_{u,avg\ day}}{h_1 - h_4} \tag{3.40}$$

$$V_{TES,ps} = \frac{Q_{u,peak\ day} - Q_{u,avg\ day}}{\rho.\Delta h_{pcPCM}} \tag{3.41}$$

The second option is a strategy using full-storage, in which the TES shifts the ORC engine's operation period away from the primary day-hours to correspond with the evening spike in power usage. Because of this technology, the ORC engine has shorter operating durations and may thus be designed for higher urgent electricity outputs. The evening peak power consumption is projected to occur for four hours in the night-time by default, and the PCM capacity is estimated to collect all of the solar energy received during daylight hours on a normal sunny day (Freeman et al., 2017):

$$\dot{m}_{r,fs} = \frac{Q_{u,avg\ day}}{(h_1 - h_4).\Delta t_{peak}}, \tag{3.42}$$

$$V_{TES,fs} = \frac{Q_{u,avg\ day}}{\rho.\Delta h_{pcPCM}}, \tag{3.43}$$

where $\Delta t_{peak} = 4\ h$ represents the peak time of electricity demand. Finally, the system's overall solar-to-power transformation efficiency is computed by dividing the network output of the ORC system by the total irradiation collected by the collector line-up:

$$\eta_{OV} = \frac{\sum \dot{m}_r (h_1 - h_2)}{\sum GA_{SC}}. \tag{3.44}$$

Table 3.8 lists the various sensible and latent TES materials and their characteristics. The physical parameters of the PCMs were chosen to broadly represent a variety of organic and inorganic (hydrated-salt-based) materials.

Table 3.9 shows the details of selected organic and inorganic PCMs used in this study.

Table 3.8. The properties of selected TES materials (Freeman et al., 2017; Pcmproduct, 2013)

TES materials	**ρ (kg/m^3)**	**Δh$_{sl}$ (kJ/kg)**	**c (J/kg.K)**
Inorganic PCM	1560	154	2.00
Organic PCM	825	171	2.27
Water (liquid)	940	n.a	4.25
Thermal oil	940	n.a	1.92
Quartzite	2500	n.a	0.83
Granite	2640	n.a	1.02

Table 3.9 the detail properties of selected organic and inorganic PCMs (Daniarta et al., 2023)

Organic				**Inorganic**			
PCM name	**T$_{melt}$ (K)**	**ρ (kg/m^3)**	**h$_{sl}$ (kJ/kg)**	**PCM name**	**T$_{melt}$ (K)**	**ρ (kg/m^3)**	**h$_{sl}$ (kJ/kg)**
Dymethyl sebacate	294.15	988	125	$KF \cdot 3H_2O$	291.65	1447	231
n-octadane	301.15	814	200.2	$Mn(NO_3)_2 \cdot 6H_2O$	298.65	1728	148
Trimyristin	313.15	862	208	$CaCl_2 \cdot 6H_2O$	302.15	1802	192
Elaidic acid	320.15	851	218	$CaBr_2 \cdot 6H_2O$	307.15	1956	138
Choloroacetic acid	329.15	1580	130	$Zn(NO_3)_2 \cdot 6H_2O$	309.15	1937	147
Azobenzene	340.15	1203	121	$Na_2HPO_4 \cdot 12H_2O$	313.15	1522	256
Benzylamine	351.15	982	174	$Na_2S_2O_3 \cdot 5H_2O$	321.15	1670	209
Acetamide	354.15	1159	241	$CH_3COONa \cdot 3H_2O$	331.15	1450	170

3.4. Biomass-ORC

3.4.1. Thermoeconomic analysis of ORC from Napier grass biomass

According to a projection of growth in electricity demand in Indonesia with the optimistic assumption of economic growth for 10 years with an average of 5.2% per year and moving from the realization of electricity demand in 2019, it will reach 379 TWh or undergo an average growth of 4.57% in 2029 as estimated. In that report, the government has set a target for the energy mix of the power plant by the end of 2025 for coal at 54.4%, renewable energy at 23%, oil and gas at 22.2% and 0.4%, respectively (Indonesia's State Electricity Company, 2020). Until 2020, a renewable energy power plant installed capacity in Indonesia was 63.3 GW, with the contribution of hydropower plants at 8%, the geothermal power plant at 4%, and other renewable energy resources power plants at 1%. The total share of renewable energy power plants was 11% *(Direktorat Perencanaan Korporat,* 2021). From existing renewable energy sources, not all of them can be directly converted to electricity but require other systems, namely ORC application.

In this study, the type of biomass used is Napier grass. Napier grass was chosen because it is one of the bioenergy that is suitable for cultivation in almost all climates and soil conditions in Indonesia, with a high heating value (HHV) reaching 16.56–18.11 MJ/kg (Md Said et al., 2019). The objective of this study is to evaluate the thermoeconomic performance of Napier grass as a biomass heat source that will be performed using the ORC analysis. Fig. 3.7a shows the scheme of the main ORC, including the evaporator, expander, condenser, and feed pump. The main ORC components such as the expander, condenser, pump, and evaporator are calculated in more detail to determine the cycle performance obtained and will affect the thermoeconomic result.

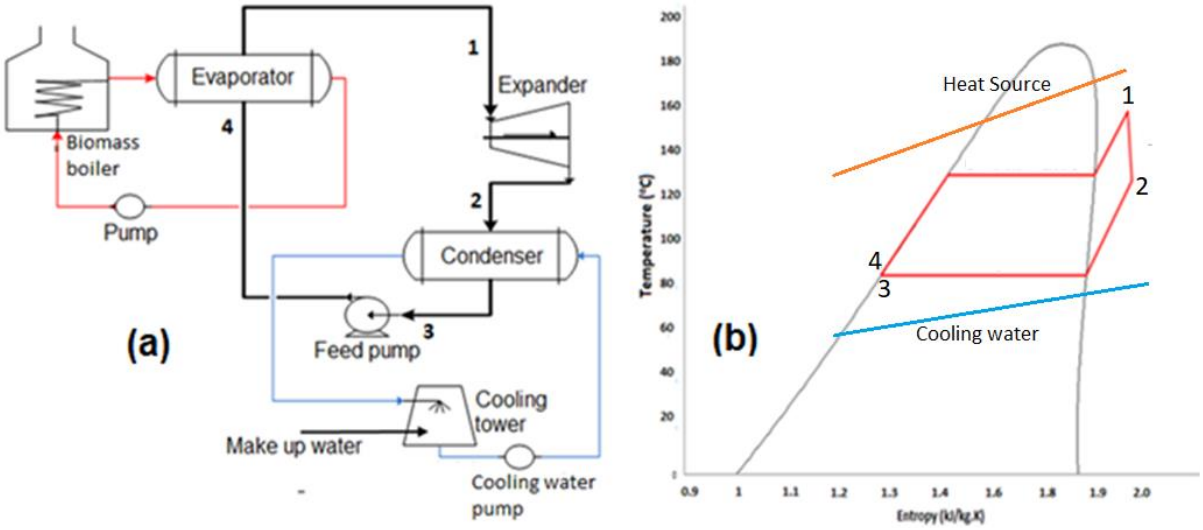

Fig. 3.7. Biomass ORC: a) schematic b) R245fa T-s diagram

To calculate the mass flow rate of the working fluid through the expander when operating, the Stodola Steam Cone rule is shown by Eq. (3.45):

$$\dot{m} = \mu_T . C_T \sqrt{p_{in} . \rho_{in}} \sqrt{1 - \frac{1}{\pi}}, \tag{3.45}$$

where: $\pi = p_{in}/p_{out}$ is the pressure ratio; μ_T is the expander nozzle position; and C_T is the expander constant value (1.41, 1.65, 1.90, 2.14, and 2.38) derived from the centrifugal chiller compressor with capacities of 300, 350, 400, 450, and 500 TR, respectively.

The amount of heat that occurs in the heat exchanger is calculated by the LMTD method using Eqs. (3.46)–(3.52):

$$Q = U\ A\ LMTD, \tag{3.46}$$

where: Q is the amount of heat needed by the evaporator and condenser (kJ); U is heat transfer coefficient in the evaporator; A is the cross-sectional area (m^2); and LMTD is log mean temperature difference (°C):

$$LMTD = \frac{(Th_{in} - Tc_{out}) - (Th_{out} - Tc_{in})}{ln\frac{(Th_{in} - Tc_{out})}{(Th_{out} - Tc_{in})}}, \tag{3.47}$$

$$U = \frac{1}{\frac{2}{\alpha_e} + R_{fo} + \frac{\Delta xw}{k_w} + R_{ft}\frac{\alpha_i}{\alpha_e}}, \tag{3.48}$$

$$\alpha_e = 0.36\frac{\lambda}{D_e}Re^{0.55}Pr^{1/3}, \tag{3.49}$$

$$\alpha_i = C_{if}\frac{\lambda}{D_i}Re^{0.8}Pr^{\frac{1}{3}}, \tag{3.50}$$

$$Re = \frac{4\dot{m}_{wf}n_p}{\pi\mu D_i n_t}, \tag{3.51}$$

$$P_r = \frac{C_p\,\mu}{k}. \tag{3.52}$$

The LMTD can be evaluated using Eq. (3.47), where $T_{h,i}$ and $T_{h,o}$ is the hot temperature of the fluid that enters and leaves the heat exchanger from biomass heat source (°C), respectively, and $T_{c,i}$ and $T_{c,o}$ is the cold temperature of the fluid that enters and leaves the heat exchanger (°C). *U* is the total of heat transfer coefficient in the heat exchanger that can be calculated using Eq. (3.48). α_e and α_i is heat transfer coefficient from the shell side and tube side shown by Eqs. (3.49–3.50), respectively. C_{if} is the constant of internal helical fin tube with a value of 0.06–0.061 and with a diameter around 1.9–2.54 cm, respectively. Reynold number (R_e) and Prandtl number (Pr) is shown by Eqs. (3.51) and (3.52), where: $\dot{m}_{wf}$, μ, D_i, C_p, k are the mass flow rate of working fluid (kg/s), dynamic viscosity (N·s/m^2), inlet diameter of tube (m), specific heat (J/kg·K), and thermal conductivity (W/m·K), respectively. Then, Eq. (3.53) was used to calculate the $\dot{m}_{bio}$ in the biomass boiler:

$$\dot{m}_{bio} = \frac{Q_{evap}}{\eta_{global}\,LHV_{bio}}, \tag{3.53}$$

where: $\dot{m}_{bio}$ is the mass flow rate in the boiler (kg/s); Q_{evap} is the heat of evaporator (kW); η_{global} is the global efficiency of the boiler (%); and LHV_{bio} is the low heating value of biomass (kJ/kg).

In a new or existing power plant system, the optimization process is used to find the system's operating conditions that can produce the highest thermal efficiency. However, it is also necessary to study the investment costs incurred compared to the final result to determine the feasibility of investing, better known as thermoeconomic analysis. In this study, the analysis is limited to the study of investment costs or purchase equipment costs (PEC) for several components of the ORC power plant using the following equations (Bejan et al., 1995):

For feed pump:

$$PEC_{FP} = 900\left({}^{W_{FP}}/_{300}\right)^{0.25} \tag{3.54}$$

Cooling tower:

$$PEC_{CTP} = 500({}^{W_{CTP}}/_{300})^{0.25} \tag{3.55}$$

HTF pump:

$$PEC_{HTFP} = 500({}^{W_{HTFP}}/_{300})^{0.25}, \tag{3.56}$$

where: W_{FP} is the work by feed pump (kWe); W_{CTP} is the work by cooling tower pump (kWe); and W_{HTF} is the work by HTF pump (kWe). Therefore, Eq. (3.57) is the cooling tower investment cost (PEC_{CT}) according to (Carberry et al., 1991):

$$PEC_{CT} = x_1\dot{m}_{cw}^{x_2}10^{x_3AR+x_4A+x_5R+x_6}, \tag{3.57}$$

where: $\dot{m}_{cw}$ is the mass flow of cooling water (kg/s); A is the difference of $T_{cw\text{-}in}$ and $T_{wb\text{-}ambient}$; while R is the difference of $T_{cw\text{-}out}$ and $T_{cw\text{-}in}$. The main component of the ORC power plant consists of the evaporator, condenser, and expander. The investment costs for these three components will be assumed to be one component with information about the investment costs from the catalogue. To find out the current price, the present value formula is used according to Eq. (3.58), with the assumption that the annual interest rate (i) is 6%, and the past value is the price of centrifugal chiller in 2012, as follows:

$$Present\ Value = Past\ Value(1 + i)^n. \tag{3.58}$$

According to (Tereschenko, 2016), investment costs for the heat boiler for biomass-fired ORC generation applications represent 600–800 USD/kWe.

In the direct combustion process of the biomass boiler, the biomass used is Napier grass (*Pennisetum purpuerum*) with the proximate data and the ultimate analysis for stems (NGS), leaves (NGL), and mixed between stems-leaves (NGT), as shown in Table 3.10. In this study, the combustion calculation in the biomass boiler uses data from the high heating value (HHV) of the mixed between stems-leaves (NGT), in order to obtain the low heating value (LHV_{dry}) using Eq. (3.59):

$$LHV_{dry} = HHV_{dry} - 2.442\ x\ 8.396\ x\ \frac{H}{100}\ , \tag{3.59}$$

where H is the fraction of hydrogen (Tariq et al., 1994).

Table 3.10. Proximity and analysis of Napier grass

Proximity analysis (wt. %)	**Value**	**Ultimate analysis (wt. %)**	**Value**
Water content	74.22 ± 0.17	Carbon (C)	45.19 ± 0.70
Volatile matter	85.17 ± 0.21	Hydrogen (H)	5.93 ± 0.15
Ash content	6.34 ± 0.01	Nitrogen (N)	1.45 ± 0.04
Fixed carbon	8.49 ± 0.02	Sulphur (S)	0.35 ± 0.01
HHV (MJ/kg)	16.58 ± 0.10	Oxygen (O)	47.17 ± 0.71
O/H (atomic ratio)	0.131	O/C (atomic ratio)	1.05

3.4.2. 4E analysis of existing biomass-ORC with capacity 150 kWe

The biomass-ORC system is located in Baricella, a region situated approximately 15 kilometres from the city of Bologna, Italy that shown by Fig. 3.8. This plant has a production capacity of 150 kWe and operates using R134a as the working fluid. The energy generation process involves wood waste combustion, producing temperatures in the range of 160–180 °C and pressures between 11–12 bar. For the purpose of this study, a combination of tools was utilized to conduct detailed calculations. Microsoft Excel was employed in conjunction with NIST Refprop to analyse thermodynamic properties, while Unisim software served as a comparative application to validate and enhance the accuracy of the results.

Fig. 3.9a and Fig. 3.9b are diagrams of the ORC cycle using a regenerator and T-s diagram of the biomass-ORC process represented by R134a working fluid, respectively. The ORC system uses medium-to-high-temperature of steam from biomass combustion to preheat and vaporize a R134a in the evaporator (4>5). The organic fluid vapor rotates the turbine (5>6), which is directly coupled to the electric generator, resulting in clean, reliable electric power. The exhaust vapor flows through the regenerator (6>7), where it heats the R134a (2>3) and is then condensed in the condenser and cooled by the cooling circuit represented by blue colour (7>8>1). The R134a is then pumped (1>2) into the regenerator and evaporator, thus completing the closed-cycle operation. The pump is a plunger piston type, capable of increasing the working fluid pressure to 4-5 MPa. It enters the regenerator to obtain initial heat from the expansion, which results in the expander.

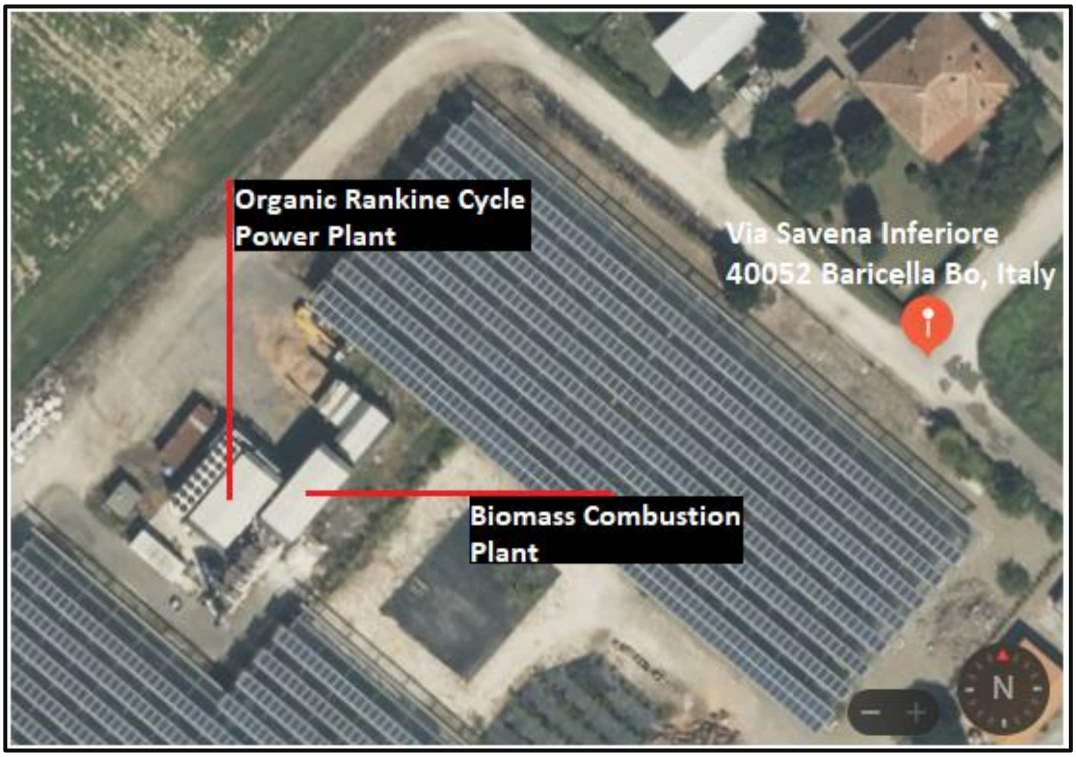

Fig. 3.8. The site location of biomass-ORC

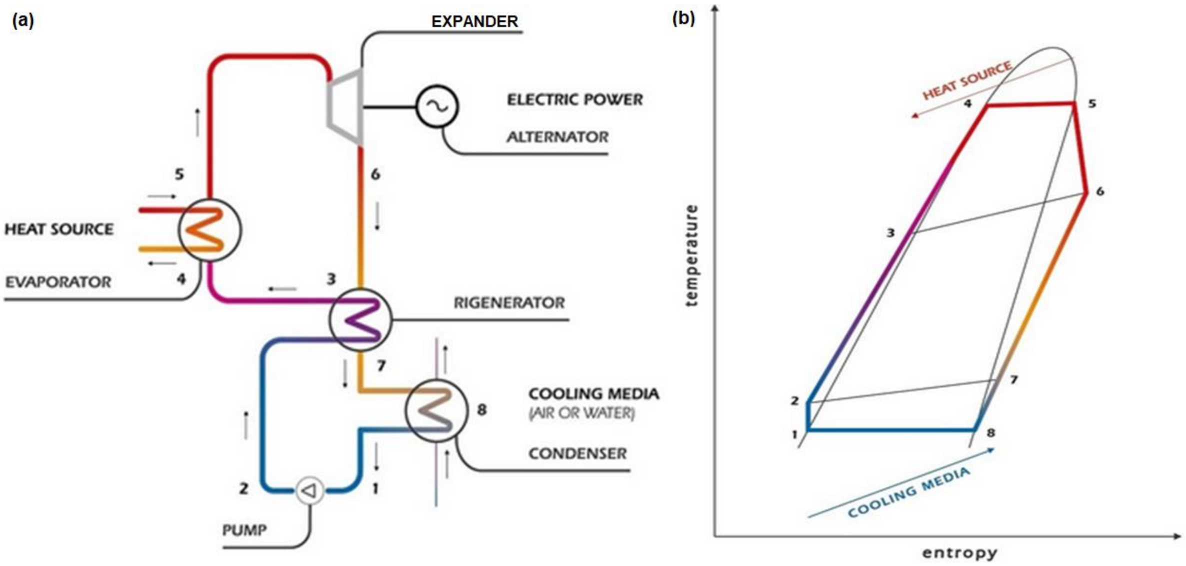

Fig. 3.9. The schematic of: a) biomass ORC, b) T-s diagram

The first and second law of thermodynamics should be applied to determine the performance of the ORC. The energy equilibrium equation may be used to calculate the quantity of power generated and the heat required by the ORC. In a steady state condition, energy and exergy balancing of the formula for each component are describe in Table 3.11.

Table 3.11. ORC components governing equations (Moran and Shapiro, 2006)

Components	**Energy balance**	**Exergy balance**
Pump	$\dot{W}_{pump} = \frac{\dot{m}(h_2 - h_1)}{\eta_{pump}},$	$\dot{W}_{pump} = \dot{E}_{X2} - \dot{E}_{X1} + \dot{E}_{D\_pump}$
Regenerator	$\dot{Q}_{reg} = \dot{m}(h_3 - h_2),$	$\dot{E}_{D\_reg} = \dot{E}_{X6} + \dot{E}_{X2} - \dot{E}_{X3} - \dot{E}_{X7}$
Evaporator	$\dot{Q}_{evap} = \dot{m}(h_5 - h_4),$	$\dot{E}_{D\_evap} = \left(1 - \frac{T_0}{T_{in}}\right) Q_{in} + \dot{E}_{X5} - \dot{E}_{X4},$
Expander	$\dot{W}_{exp} = \dot{m}(h_5 - h_6)\, \eta_{exp},$	$\dot{E}_{D\_exp} = \dot{E}_{X5} - \dot{E}_{X6} - \dot{W}_{exp},$
Condenser	$\dot{Q}_{cond} = \dot{m}(h_7 - h_1),$	$\dot{E}_{D\_cond} = \dot{E}_{X7} - \dot{E}_{X1} - \dot{Q}_{cond},$
Efficiency	$\eta_{thermal} = \frac{\dot{W}_{net}}{\dot{Q}_{evap}}$	$\psi_{system} = \frac{\sum \dot{W}_{ORC}}{\dot{E}_{Xin}}$

In the Table 3.11 $\dot{W}_{exp}, \dot{W}_{pump}$ are power of expander and pump respectively, while $\dot{m}$ is mass flow rate (kg/s), h is specific enthalpy (kJ/kg), and $\dot{Q}_{in}, \dot{Q}_{out}$ are the heat enters and exit from the system. $\dot{E}_{D\_exp}, \dot{E}_{D\_cond}, \dot{E}_{D\_evap}, \dot{E}_{Dpump}, \dot{E}_{D\_reg}$ are represent the rate destruction of exergy in the expander, condenser, pump, evaporator, and regenerator, respectively. Exergy analysis may improve economic and environmental performance by determining how much energy quality is accessible in biomass-ORC system. Furthermore, this study uses the exergy function to measure the sustainability of a mechanism and system. It is also known as the exergy sustainability index (ESI) among academics. Among other things, ESI is a reliable indicator. The degree of sustainability and may be determined from the related exergy balancing equations for each cycle and study of ESI (Aydin, 2013) that provide by Eqs. (3.60-3.63) as follows:

Exergy waste ratio (EWR):

$$EWR = \frac{\sum \dot{E}_{Xwaste}}{\sum \dot{E}_{Xinput}} = \frac{\sum \dot{E}_{destroyed}}{\sum \dot{E}_{Xinput}} \tag{3.60}$$

Exergy efficiency:

$$\psi_{overall} = \frac{\dot{E}_{Xout}}{\dot{E}_{Xin}} \tag{3.61}$$

Environmental effect factor (EEF):

$$EEF = \frac{EWR}{\psi_{overall}} \tag{3.62}$$

Exergy sustainability index (ESI):

$$ESI = \frac{1}{EEF} \tag{3.63}$$

This analysis is conduct with some presumptions: 1) steady state; 2) heat losses and pressure drop in component systems are neglected; 3) inlet expander temperature was based on a variation of $T_{c,o}$; 4) the cooling water temperature is set at 25 °C; 5) the pump and expander isentropic efficiency was set at 65% and 70%, respectively; 6) the exergy of hot water from the evaporator and the exergy of cooling water that entering and leaving a condenser are negligible. Then, the Eq. (3.64) for calculating the biomass mass flowrate in the evaporator:

$$\dot{m}_{bio} = \frac{\dot{Q}_{evap}}{\eta_{global}\, LHV_{bio}} \tag{3.64}$$

where $\dot{m}_{bio}$ is the biomass mass flowrate (kg/s), η_{global} is the global efficiency of the boiler (%); LHV_{bio} is the low heating value of biomass (kJ/kg) and the value is obtain from Table 3.12.

Table 3.12. Proximity analysis of woodwaste (Pala et al., 2017)

Analysis	**Biomass content**	**unit**	**value**
Ultimate analysis	Carbon	%	50.56
	Hydrogen	%	6.70
	Nitrogen	%	0.16
	Sulphur	%	0.20
	Oxygen	%	42.51
	Chlorine	%	0.002
Approximate analysis	Volatile matter content	%	81.81
	Ash	%	0.36
	Fixed carbon	%	17.83
	LHV	kJ/kg	19.74
	HHV	kJ/kg	19.40

Thermoeconomics seeks to determine the cost formation process of internal flows and ultimate products in energy systems and process plants This allows for a more accurate assessment of the various production possibilities and a better knowledge of the internal economic processes that occur during the production process (Lozano and Valero, 1993). The word thermoeconomics refers to a mix of thermodynamic and economic analysis. The proposed approach incorporates energy into thermodynamic analysis and reflects the unit costs of flows in an energy base. There were two key reasons for using energy rather than exergy in the computations. First, unit charges in terms of energy are the most common billing system viewed by final customers, who will ultimately decide whether or not to employ the solar plant's energy services (consumers pay per unit of energy consumed). Second, there is no cost allocation (each component has a single product flow) (Pala et al., 2017).

The economic indicators used in the analysis are Simple Pay Back (SPB), Net Present Value (NPV), and levelized cost of electricity (LCOE) (Eqs. 3.65-3.67) as follows:

$$SPB = \frac{C_{TCI}}{C_{ncf}}, \tag{3.65}$$

$$NPV = -(C_{TCI}) + \sum_{i=1}^{N} C_{ncf}(1+i)^{-t}\,, \tag{3.66}$$

$$LCOE = \frac{\frac{C_{TCI}}{1-(1+i)^{-n}} + (C_{bio} + C_{ash} + C_{O\&M})}{E_{e,a}}\,, \tag{3.67}$$

where C_{TCI} represent the system's total capital investment, to calculate it, add the beginning costs of the system's components, as stated in Eq. (3.68) and Table 3.13 shows the breakdown cost equations of each component for ORC system as follow:

$$C_{TCI} = C_{Boiler} + 1.5\, C_{ORC,PEC.} \tag{3.68}$$

Table 3.13. Breakdown of purchased components of ORC (Fraia et al., 2023; Langdon, 2024; Taheri et al., 2017)

Components cost	Cost function	No Eqs.
Biomass boiler	$C_{boiler} = 1600\,(\dot{m}_{bio} \times 0.9 \times 3600)^{0.67}$	(3.69)
ORC expander	$C_{ORC,exp} = 6000\, W_{ORCexp}^{0.7}$	(3.70)
ORC pump	$C_{ORC,pump} = 3540\, W_{ORCpump}^{0.71}$	(3.71)
ORC evaporator	$C_{ORC,evap} = 309.14(A_{ORCevap}) + 293.15$	(3.72)
ORC regenerator	$C_{ORC,reg} = 1.3(190 + A_{ORCreg})$	(3.73)
air condenser	$C_{ORC,cond} = 1397\, A_{ORCond}^{0.89}$	(3.74)
Working fluid	$C_{wf} = 25\, \dot{m}_{fluid}$	(3.75)

C_{ncf} is the system's annual economic savings, determined by adding annual revenues and operational costs as follows:

$$C_{ncf} = (C_e + C_h) - (C_{bio} + C_{ash} + C_{O\&M}), \tag{3.76}$$

where $C_e, C_h, C_{bio}, C_{ash}, C_{O\&M}$ is annual selling electricity cost, annual selling heating cost, annual biomass consumption, annual disposal ash, and annual cost operational and maintenance, respectively. Several approaches are used in the literature to calculate the entire cost of ORC systems based on the acquired equipment cost, taking into account extra expenses like as installation labour, piping, instrumentation and controls, electrical equipment, structural work, engineering, and supervision. In the current analysis, the assumed split of these expenses is provided in Table 3.14. The particular investment cost (€/kWe), which expresses the investment cost per unit of installed electrical capacity, is thus defined as the following equation:

$$SIC = \frac{C_{TCI}}{W_{net,plant}} \tag{3.77}$$

Table 3.14. Breakdown of non-purchased components (Braimakis et al., 2021; Lemmens, 2016)

Non-component cost	% PEC
Purchased equipment installation	30
Piping	20
Instrumentation and controls	10
Electrical equipment and materials	10
Structural work	15
Engineering and supervision	25
Contingencies	20
Start-up and working capital	20
Sum	150

The economic assumptions are summarized in Table 3.15. The price of biomass is an important factor in determining the investment's cost-effectiveness. However, its value is highly unknown because it is determined by a variety of global and local factors, including the type and quality of biomass, availability, supply and demand, internationally and nationally adopted bioenergy legislation, supply chains, and so on. The EU has a number of assistance schemes in place to encourage the use of biomass to generate electricity. According to existing feed-in-tariff schemes, power selling prices from solid biomass vary in different EU member states from a minimum of 81.2 €/MWhe (Slovakia) to up to 198 €/MWhe (Italy), with the majority falling between 90 and 120 €/MWhe (Banja et al., 2019). The selling price of energy is determined by national regulation. It may vary depending on the plant's power capacity and scope, with smaller plants and combined heat and power units being more heavily incentivized. As a result, in the current work, a base-case value of 120 €/MWhe is assumed. This analysis estimates a base-case value of 0.065 €/kWh.

Table 3.15. Base-case economic assumptions (Banja et al., 2019; “Italy Electricity Price,” 2024; Pallis et al., 2019; Pantaleo et al., 2015)

Parameter	Value
Electricity selling price	95 €/MWhe
Ash disposal cost	60 €/tn of ash
Project lifetime (n)	25 years
Annual operation and maintenance	2% of TCI
Interest rate (i)	7%
Biomass fuel cost (waste wood) per wet ton	50 €/tn
Biomass consumption	1500 tn/year
Heat selling price	100 €/MWh
Construction	2 years

3.5. Experimental study of ORC

3.5.1. Performance evaluation

The described components were assembled to create the prototype system. Fig. 3.10a shows a diagram of the system in which the measurement system represents the placement of monitoring and control sensors, the control system, the main circuit and the secondary. The electrical connections were made on two separate electrical panels concerning the power connections and the signal and measurement connections to prevent line disturbances on the signals generated by the sensors mainly due to the use of power inverters.

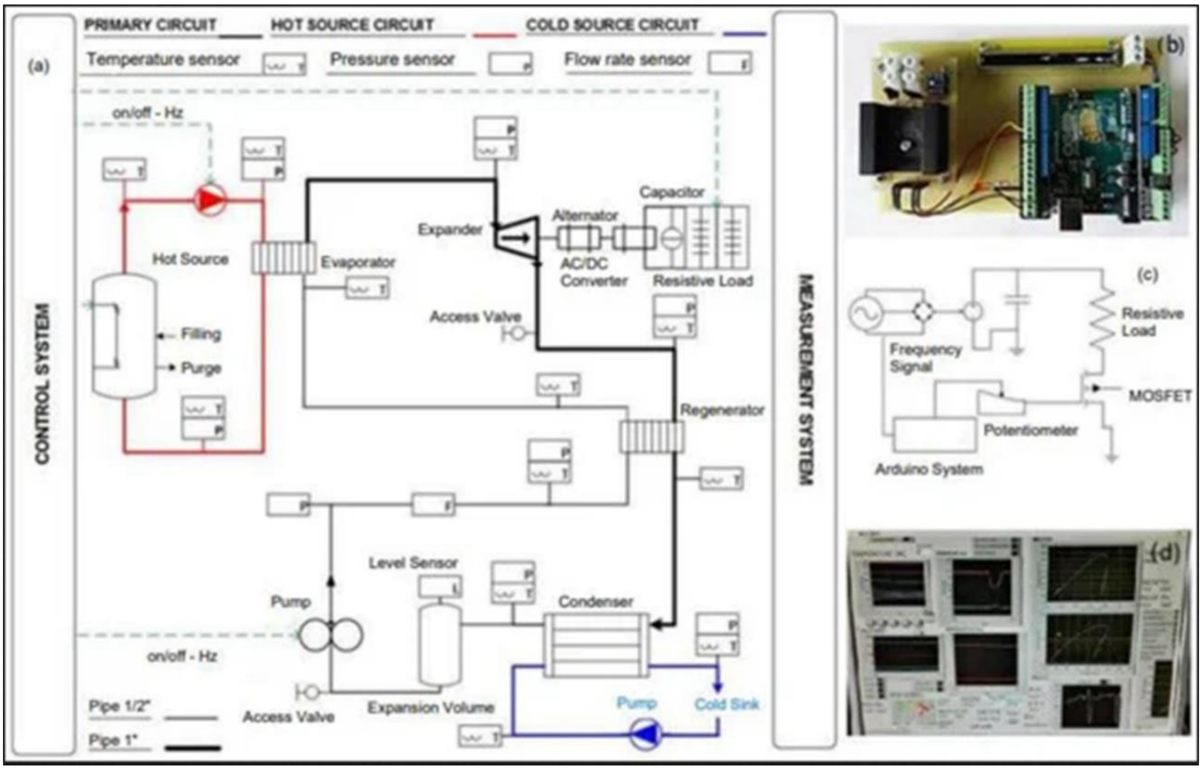

Fig. 3.10. ORC experimental setup: (a) P&I test rig, (b) frequency-driven rpm regulator, (c) electrical control system, (d) LabView user interface

In the preliminary test the system prototype's development went through preliminary tests to verify the components used. The thermodynamic cycle must occur in an airtight circuit without air with a maximum pressure of 25 bar. While carrying out the experimental test, monitoring the physical quantities of interest was achieved through the appropriate choice and positioning of sensors at the various points between each ORC main component (Table 3.16). At the same time, the instruments used for monitoring the thermodynamic cycle are shown in

Table 3.17, with detailed specifications and accuracy for each sensor. Additionally, the data management and acquisition software was developed specifically for the ORC prototype application using LabView (Fig. 3.10d), which has a main feature for real-time monitoring management and visualization. While the characteristic thermodynamics was evaluated in Microsoft Excel and integrated with NIST Refprop.

Table 3.16. Component’s detail and technical selection

Main Component	**Specification**
Expander	Sanden, hermetic Scroll type, integrated with brushless 3-phase generator
Evaporator	Flat-plate HE type, $A_{surface}$ = 2.38 m^2, no of plate = 60, vol = 1.28 m^3
Regenerator	Flat-plate HE type, $A_{surface}$ = 1.4 m^2, no of plate = 52, vol = 1.58 m^3
Condenser	Flat-plate HE type, $A_{surface}$ = 2.11 m^2, no of plate = 70, vol = 2.07 m^3
Working fluid pump	Nuert PRG 9, Magnetic vane pump, 1.1 kW, 4 winding magnetic poles
Boiler	Steam generator, 60 kW, T_{max} = 180 °C, P_{max} = 15 bar, $\dot{m}$ = 1.2 kg/s

Table 3.17. Main sensors specification

Main Sensor	Specification
Flow	Micromotion, coriolis effect mass sensor, 4-20 mA output, Acc: 0.5%
Temperature	Tersid, RTD 1/3 DIN, acc: 0.08-0.29 °C, 0-180 °C
Pressure	Barksdale, Diaphragm sensor, acc: 0.25%, 16-40 barG
AC voltage	HP Agilent, Acquiere 34970A, acc: 0.002% vm
DC voltage	HP Agilent, Acquiere 34970A, acc: 0.002% vm
Frequency	HP Agilent, Acquiere 34970A, acc: 0.002% vm
Current	LEM, half effect sensor, acc: 0.2% fs, 15 A

Eq. (3.78) describes how the partial derivatives approach is used to calculate measurement uncertainty. This method involves calculating measurement uncertainty by considering each variable on which it depends (Daniarta et al., 2024). The technique takes into account the uncertainty in each variable and then calculates how these uncertainties interact (combined uncertainty or) to affect the result (Y). Furthermore, Eqs. (3.79-3.80) can be used to determine the uncertainty of $\dot{W}_{exp}$ and η as described as follows:

$$U_c(Y) = \sqrt{\sum_{i\in\{sensors\}} \left(\frac{\partial Y}{\partial i}\right)^2 u^2(i)}, \tag{3.78}$$

$$U_c(\dot{W}_{exp}) = \sqrt{\left(\frac{\partial W_{exp}}{\partial i}\right)^2 u^2(T) + \left(\frac{\partial W_{exp}}{\partial i}\right)^2 u^2(P) + \left(\frac{\partial W_{exp}}{\partial i}\right)^2 u^2(\dot{m}) + \left(\frac{\partial W_{exp}}{\partial i}\right)^2 u^2(N)}, \tag{3.79}$$

$$U_c(\eta) = \sqrt{\left(\frac{\partial \eta}{\partial i}\right)^2 u^2(T) + \left(\frac{\partial \eta}{\partial i}\right)^2 u^2(P) + \left(\frac{\partial \eta}{\partial i}\right)^2 u^2(\dot{m}) + \left(\frac{\partial \eta}{\partial i}\right)^2 u^2(N)}, \tag{3.80}$$

where $\dot{W}_{exp}$ and η are governed by the ṁ with the different of enthalpy, which is principally influenced by temperature (T), pressure (P), mass flow rate (ṁ), and speed rotation of pump (N).

3.5.2. Predicted analysis and optimisation of experimental ORC using ANN

Numerous ORC experimental tests have been conducted but predicting unknown or unmeasured data and determining optimal operating settings remain widely debated topics. Machine learning approaches are gaining increased attention in ORC applications. Due to their self-learning capabilities, nonlinearity, and ability to approximate complex functions, artificial neural networks (ANN) have been extensively employed to develop predictive models. The conducted additional experimental tests on a 2 kW ORC prototype. By employing ANN to predict unknown or unmeasured experimental data, we aim to effectively reduce experimental resource consumption. Consequently, an ANN-ORC model was developed and validated using 102 sets of ORC experimental data to optimize system performance and operational parameters. The study includes a parametric analysis and investigates multi-objective optimization for maximizing output work and thermal efficiency.

The artificial neural network (ANN) is a computational model inspired by artificial neurons. In an ANN, each neuron corresponds to an activation function, and the connections between neurons are associated with weights that signify memory. The ANN approach is capable of managing non-linear, unrestricted, and non-convex systems. The output of an ANN model is influenced by the connection patterns, weights, and activation functions, as represented by (Aiken and Coxe, 2010):

$$y = f\left(\sum_j w_{ij} x_j + b\right), \tag{3.81}$$

where *f* represents the activation function, *w* is the weight value, *x* is the input vector, and *b* is the bias value.

This study seeks to forecast the behaviour of an established ORC system accurately. The input vector of the ANN model should contain as many parameters as feasible. The input vectors for the ORC system are seven key operating parameters: working fluid mass flow rate ($\dot{m}$), pump speed rotation (N_{pump}), expander inlet pressure (P_1), expander outlet pressure (P_2), expander inlet temperature (T_1), expander outlet temperature (T_2), condenser temperature (T_{cond}). The rationale for picking the seven operating parameters listed above is as follows. The ORC pump's mass flow rate and speed rotation can be adjusted based on its operating condition. The expansion ratio, which affects power production, is determined by the pressures at the expander's input (P_1) and output (P_2). The degree of superheat is closely proportional to the temperature and pressure at the expander input. Lowering the condenser outlet temperature improves the ORC system's thermal efficiency.

The next step is to determine the optimal number of hidden neurons. The mean relative error (MRE), mean squared error (MSE), and correlation coefficient (R) of the proposed model are calculated using neuron counts ranging from 4 to 11, as shown in Table 3.18. Initially, as the number of hidden neurons increases, the model's accuracy improves; however, after a certain point, it begins to decline. Considering both the model's accuracy and complexity, the final selection for the number of hidden neurons is set to 10.

Table 3.18. The statistic parameter results of each number hidden layer

X	**W_{exp}**			**$\eta_{thermal}$**		
	MSE	MRE	R	MSE	MRE	R (%)
4	13148	0.10051	0.97484	0.62309	0.09158	0.89136
5	3617.2	0.055702	0.99082	0.42153	0.077148	0.92416
6	3570.9	0.061877	0.99096	0.32584	0.073633	0.94535
7	4645.3	0.042817	0.98845	0.5531	0.13985	0.90027
8	4940.8	0.081504	0.98948	0.83783	0.12692	0.84847
9	6642.9	0.032561	0.98305	0.33335	0.072238	0.9409
10	**24960**	**0.1915**	**0.95442**	**0.43479**	**0.078412**	**0.92601**
11	23792	0.16877	0.95678	0.32694	0.076692	0.94227

Finally, the output layer of the ANN represents the power output ($\dot{W}_{exp}$) of a single scroll expander, while the thermal efficiency of the ORC ($\eta_{thermal}$) is illustrated in Fig. 3.11, depicting the structure of the neural network model with 102 experimental datasets were acquired and divided into three groups: 70% for training, 15% for testing and 20% for validation.

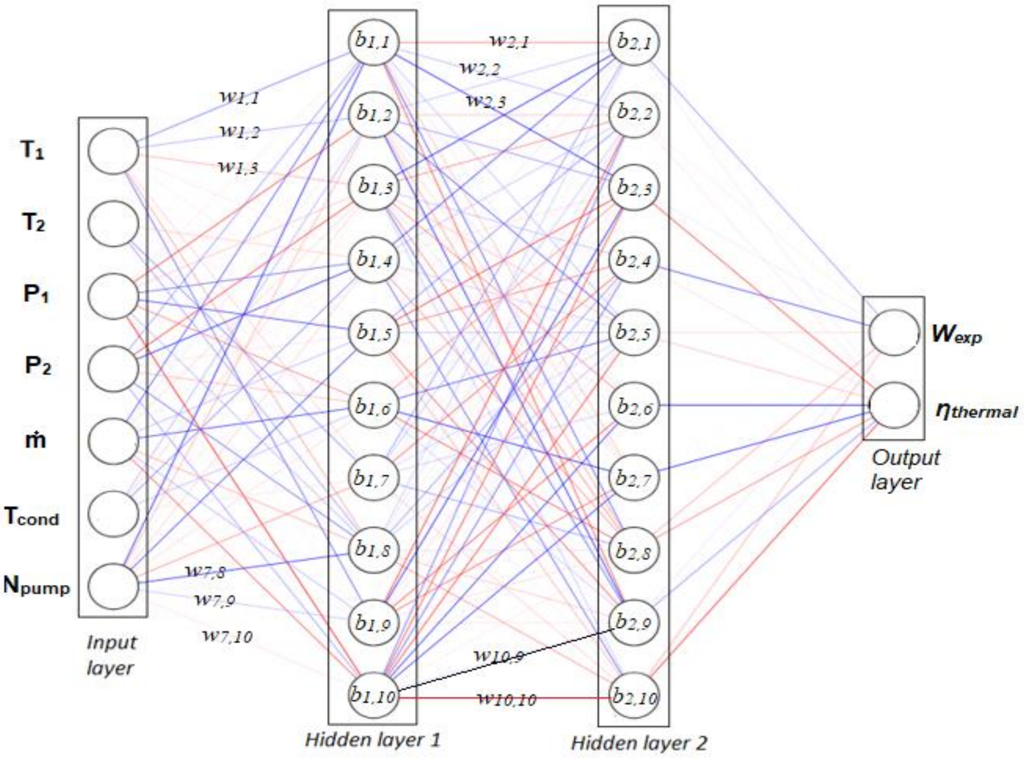

Fig. 3.11. The ANN of ORC

The partition of this data was decided. This study utilizes two widely recognized metrics to assess the prediction performance of the ANN model. The first metric is MSE, which serves as a straightforward measure of the average deviation of the data. Generally, a low MSE value indicates a high accuracy in forecasting. The MSE is calculated as follows:

$$MSE = \frac{1}{Q}\sum_{k=1}^{Q}[y(k) - t(k)]^2, \tag{3.82}$$

where *y(k)* and *t(k)* are the prediction and experiment data, respectively. MRE of a prediction is proportional to its percentage and it's expressed by:

$$MRE = \frac{1}{Q}\sum_{k=1}^{Q}\frac{[y(k)-t(k)]}{y(k)} \times 100\%, \tag{3.83}$$

The correlation coefficient between prediction and experiment data is represented as *y* and *t*, and it's expressed by:

$$R = \frac{(y-\bar{y})(t-\bar{t})^T}{\sqrt{(y-\bar{y})(y-\bar{y})^T}\sqrt{(t-\bar{t})(t-\bar{t})^T}}, \tag{3.84}$$

where $\bar{y}$ and $\bar{t}$ are the mean values of the two datasets. ANN models typically achieve a higher R-value. However, an R value close to 1 does not always guarantee a robust regression model. Therefore, the distributed absolute error and relative error, derived from Eqs. (3.85) and (3.86), are utilized to assess whether the model is sufficiently accurate to represent the experimental results.

$$absolute\ error = \ y(k) - t(k), \tag{3.85}$$

$$relative\ error = \frac{[y(k)-t(k)]}{y(k)} \times 100\%. \tag{3.86}$$

Fig. 3.12 presents a correlation matrix that illustrates the relationships between the inputs and outputs of the ANN model. The matrix is constructed using Pearson's coefficient, with values ranging from -1 to 1. Positive and negative signs indicate positive and negative correlations between variables, respectively.

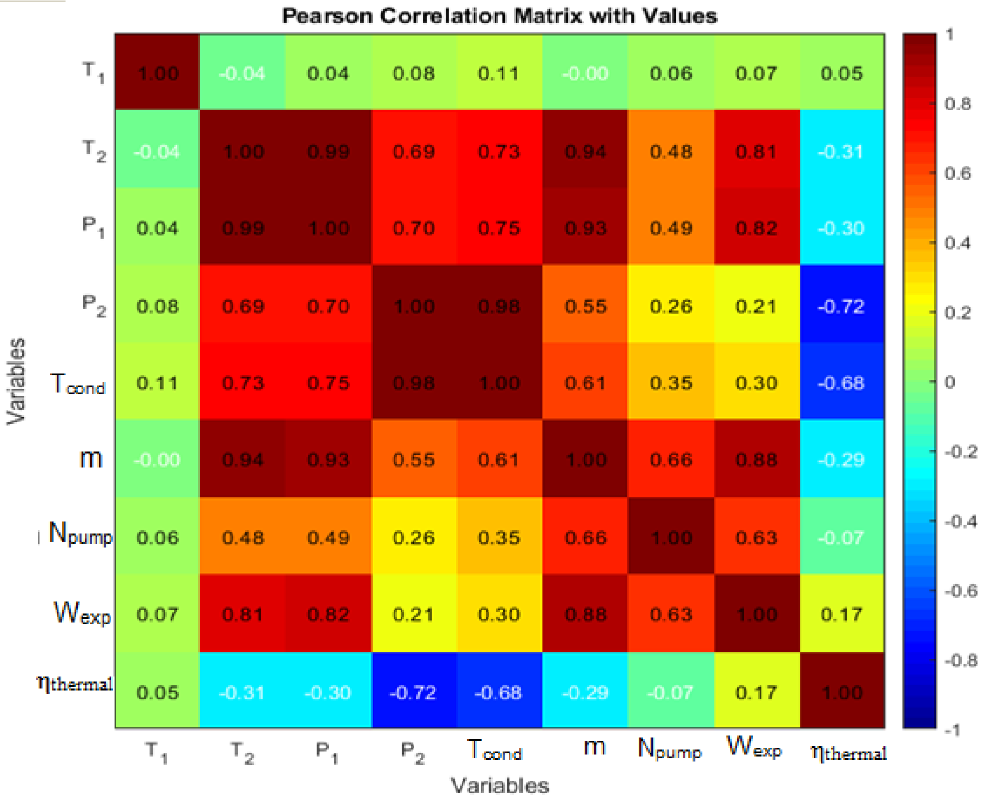

	T_1	T_2	P_1	P_2	T_{cond}	m	N_{pump}	W_{exp}	$\eta_{thermal}$
T_1	1.00	-0.04	0.04	0.08	0.11	-0.00	0.06	0.07	0.05
T_2	-0.04	1.00	0.99	0.69	0.73	0.94	0.48	0.81	-0.31
P_1	0.04	0.99	1.00	0.70	0.75	0.93	0.49	0.82	-0.30
P_2	0.08	0.69	0.70	1.00	0.98	0.55	0.26	0.21	-0.72
T_{cond}	0.11	0.73	0.75	0.98	1.00	0.61	0.35	0.30	-0.68
m	-0.00	0.94	0.93	0.55	0.61	1.00	0.66	0.88	-0.29
N_{pump}	0.06	0.48	0.49	0.26	0.35	0.66	1.00	0.63	-0.07
W_{exp}	0.07	0.81	0.82	0.21	0.30	0.88	0.63	1.00	0.17
$\eta_{thermal}$	0.05	-0.31	-0.30	-0.72	-0.68	-0.29	-0.07	0.17	1.00

Fig. 3.12 Pearson correlation matrix

The strength of the correlation increases as the coefficient approaches 1 or -1, while it weakens as it approaches zero. The correlation matrix serves two primary purposes. First, it clarifies the relationships among the input variables. For instance, $\dot{W}_{exp}$ exhibits strong correlations with $\dot{m}$, P_1, T_2, N_{pump} with respective values of 0.88, 0.82, 0.81, and 0.62. On the other hand, $\eta_{thermal}$ displays a negative correlation with the other input variables, except for $\dot{W}_{exp}$ and T_1. Consequently, in this study, $\eta_{thermal}$ will be influenced by the input variables from $\dot{W}_{exp}$, which can be attributed to the specific characteristics of the ORC. Additionally, Table 3.19 outlines the parameter settings for the ANN analysis conducted in this study.

Table 3.19. The specific parameter settings

Parameter	Value
Learning rate	0.5
Neural Number	10
Hidden layer	2
Performance	Mean squared error
Training ratio	75 %
Test ratio	15%
Validation ratio	15%

4. RESULTS

In this chapter, the performance results of ORC simulations based on energy, exergy and environmental analyses are discussed thoroughly with ORC heat sources from geothermal and solar. At the same time, economic discussion is added for biomass heat sources. Meanwhile, the addition of TES, from sizing to daily performance, is discussed for solar-ORC. Further performance of the experimental test rig is discussed, and prediction analysis and optimization with the ANN method are carried out.

4.1. ORC utilization from Tura geothermal power-plant excess steam

The Tura GPP operates at a design temperature of approximately 123–126 °C with a reservoir flow rate of 86 kg/s and an outflow temperature ranging from 122–125 °C, achieving a total production capacity of 2.7 MW. The excess hot water from the field, at a temperature of 75–78 °C, still retains a significant amount of enthalpy, which can be utilized for additional electricity generation, according to the operating condition, data and equations are provided in sub-chapter 3.2. The results are discussed below.

Fig. 4.1a shows the effect of evaporator pressure on the power net ($\dot{W}_{net}$) of each working fluid based on energy balance calculation. It can be seen based on the graphs, the small pressure enters the expander will produce a small power and efficiency, as well. Based on evaluation, it can be found that Propane is a working fluid that has the highest power net produce of 41 kW at a pressure of 2.48 MPa, and R125 has the lowest work net produce of 10.25 kW at the highest pressure of 3.6 MPa. This is because the expansion of the turbine work experienced by propane is greater than the other working fluids. This is in accordance with the supercritical ORC analysis carried out by (Burhanuddin et al., 2019) which uses propane as power and produces the greatest power compared to other working fluids. Meanwhile Fig.4.1b shows the effect of evaporator pressure on thermal efficiencies of each working fluids based on energy balance equations. It can be seen from the graphic that the smaller the pressure that enters the turbine, the smaller thermal efficiency of the cycle can be achieved. Based on evaluation, it can be found that R134a is a working fluid that has the highest thermal efficiency of 11.98 % at a pressure of 2.03 MPa, while the R125 has the lowest thermal efficiency of 8.17 % at the highest pressure of 3.6 MPa. This is because the heat utilization of the evaporator as a heat provider with amount of 206.7 kJ/kg can be utilised more by R134a compared to other working fluids.

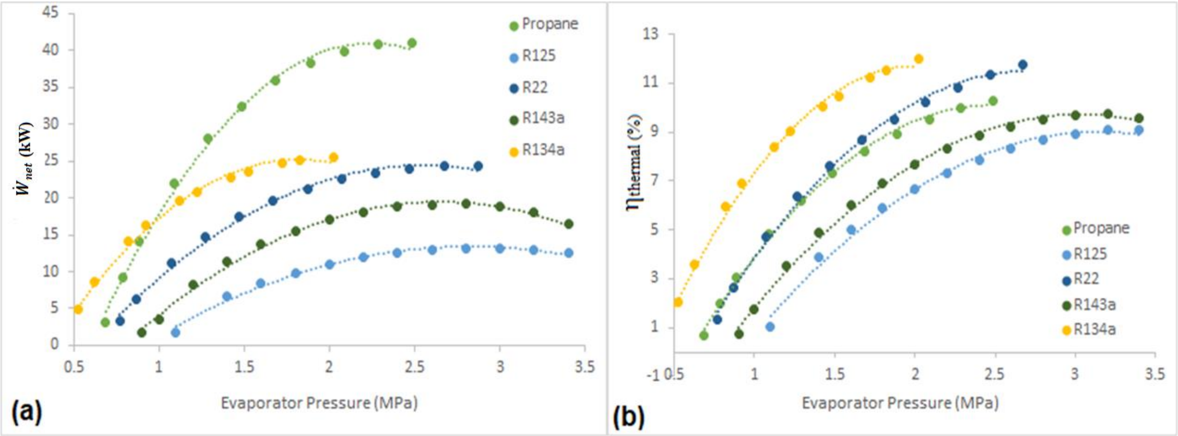

Fig. 4.1. Performance result in different evaporator pressure: a)$\dot{W}_{net}$, b) $\eta_{thermal}$

Fig. 4.2a shows that the greatest exergy destruction in the ORC components was occurred in the evaporator, followed by condenser, turbine and pump. The highest exergy destruction occurred in the evaporator during the heat exchange process. Meanwhile the evaporator that uses propane as its working fluid experiences the greatest exergy destruction (300 kW), compared to the other working R125 has the lowest exergy destruction. Fig. 4.2b shows the exergy efficiency all the ORC components of each working fluid and found that the propane's evaporator component produces the highest exergy efficiency (79%) compared to other working fluids. Contrarily, the pump is the component that has the lowest yield both in exergy destruction and in exergy efficiency. Based on the calculation results it can be observed that the working fluid R22 produces the lowest exergy destruction and exergy efficiency of 3.13 kW and 3.45% respectively. This is due to the low temperature increase at the pump so that the irreversibility of the pump is not large enough and resulting the exergy destruction at the pump is low enough.

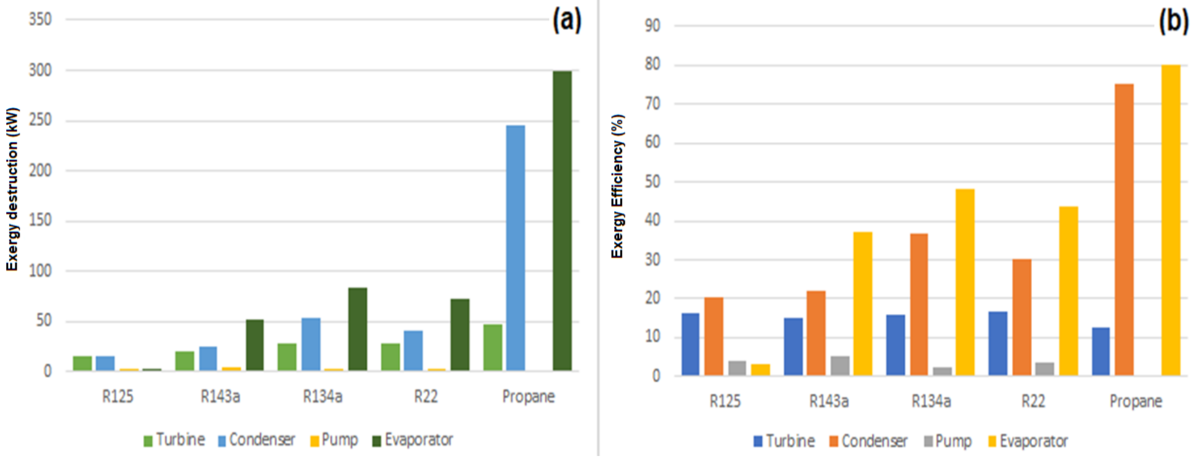

Fig. 4.2. Performance of exergy for each component: a) exergy destruction, b) exergy efficiency

The statement concerning to the exergy analysis is strengthened by the data on Fig. 4.3 which presents the exergy destruction of each component experienced by each working fluid. It can be stated that, almost all exergy destruction occurs in the evaporator, this is because the irreversible heat transfer process occurs in the evaporator. The working fluid of R125 has the highest exergy destruction in the evaporator compared to other working fluids at 83% followed by 73% (R143a), 61% (Propane), 55% (R143a), and 49% (R22). The same result occurred in the exergy analysis conducted by Abam et al., (2018) comparing performance analysis in ORC based on exergy point of view with some arrangement cycle and the result is the highest percentage of exergy destruction occurs in evaporator followed by turbines. Meanwhile, the same result conducted by Darvish et al., (2015) where the authors used R134a as the working fluid, and the result was that the boiler or evaporator was the component with the highest exergy destruction compared to other components at 59.7%. Another research by Ahmadi et al., (2019) was conducted an exergy analysis on the CHP system at the petrochemical plant and found that boilers play an important role in exhausting exergy followed by turbines. Compared to exergy analysis in other research or previous study, it can be declared that our research results have been the same trends with the others.

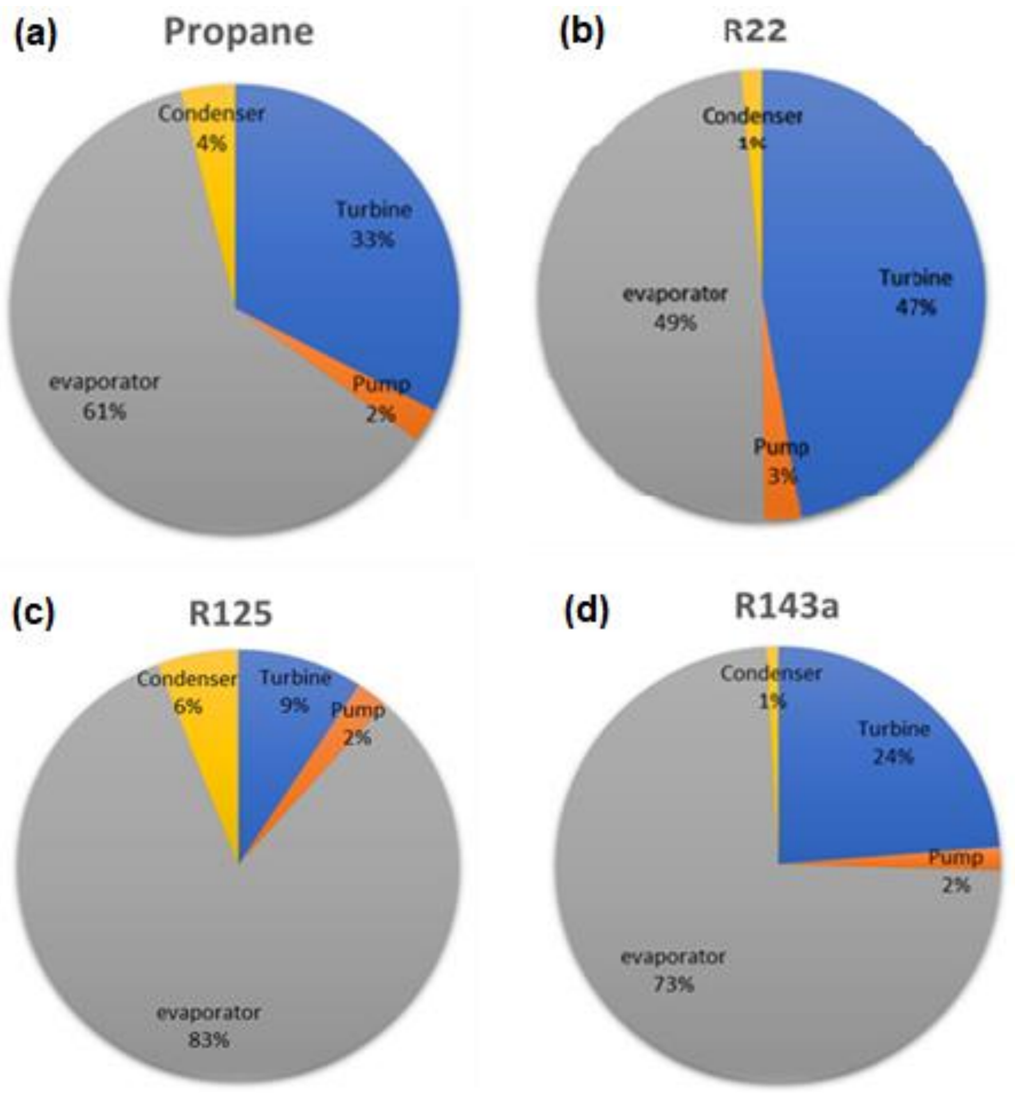

Fig. 4.3. Percentage of exergy destruction for each component: a) Propane, b) R245fa, c) R125, d) R143a

Fig. 4.4 shows the exergy sustainability of each working fluids which is represented by numerical parameter of exergy waste ratio (EWR), environmental effect factor (EEF), and exergy sustainability index (ESI) of each working fluids and two references as a comparison. EWR is the ratio of the overall waste exergy to the overall input exergy, while according to the calculation almost all working fluids have relatively the same EWR value, from 0.2397 to 0.2585 with Propane had the largest EWR value of 0.2585 and R125 had the lowest EWR value of 0.2397. The size of the EWR value is relatively small compared to the research conducted by Aydin, (2013) on the turbine component and by Abam et al., (2018) with the working fluid R245fa which produces EWR with values of 0.598 and 0.68, respectively. Consequently, the R125 had a minimum environmental influence compared to other working fluids.

The exergy sustainability index (ESI) is a degree of sustainability and is elaborated as the complementary of the environmental effect factor (Midilli et al., 2012). In Fig. 4.4, it can be seen that R143a had the highest ESI value of 0.5026 followed by R125, R22, and propane with value of 0.4669, 0.4715 and 0.4044, respectively. Those value is relatively small compared to

(Aydin, 2013) and (Abam et al., 2018) with ESI value of 0.651 and 0.491, respectively. As least review is the environmental effect factor (EEF), it can be interpreted as the indicator of the system of environmental damage due to the waste exergy destruction (Midilli et al., 2012). Fig.4.4. shows the EEF value of each working fluids, which Propane had the highest EEF value of 2.472 followed by R125, R22 and R143a with EEF values of 2.142, 2.121 and 1.989, respectively. In other hand, R143a had the smallest EEF value of among working fluids and it considered to be more sustainable.

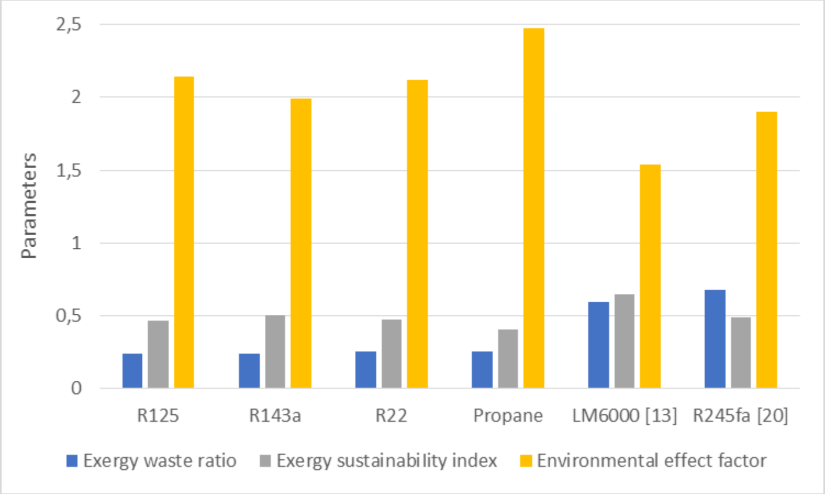

Fig. 4.4. Exergy sustainability indicators of each working fluids

4.2. Solar-ORC

4.2.1. The theoretical approach of the solar ORC integrated with PCM

In mostly European countries especially in Hungary, a solar energy resource potential with daily totals ranging from approximately 3.2 to 3.6 kWh/m² and annual totals between 1168, and 1314 kWh/m². These values highlight Hungary's relatively high suitability for solar energy utilization, making it an ideal location for implementing a solar-ORC integrated with a TES system. Based on local solar irradiation (Gödöllő) data, the operating conditions of the working cycle, and the equations provided in Sub-chapter 3.3.1, the following results are discussed.

Fig. 4.5 shows the temperature outlet profile generated by each solar collector for the average time in June. We can see that the three types of collectors produce the same temperature outlet ($T_{h,o}$) and rate heating product ($\dot{Q}_u$) trend. The highest temperature outlet is generated at around 9-10 o'clock by EFPC, ETC, and PTC with values of 372, 355, and 365 K, respectively. It is seeing that the value of solar irradiance (see Fig. 3.3) from the average climate in June and its very influential in Eq. (3.25) compared to the value of ambient temperature. So, in the following calculation, the outlet temperature results from the EFPC will be used to be the variable heat source of the solar collector. Meanwhile, at the same peak hours, the value of the rate heating product ($\dot{Q}_u$), the PTC resulted in the highest $\dot{Q}_{u'}$ around 654.68 W, followed by EFPC and ETC with values of 632.98 W and 480.47 W, respectively.

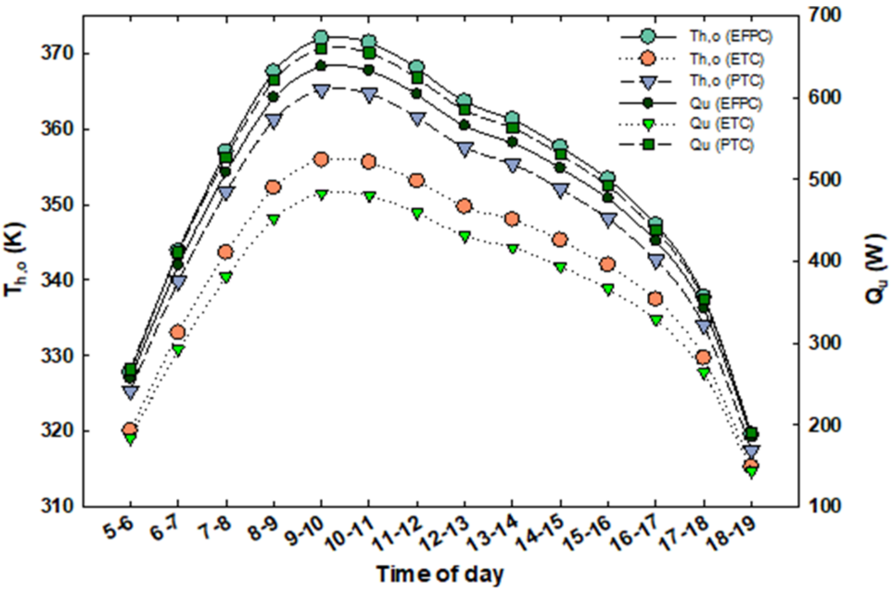

Fig. 4.5. The time profile of solar collector $T_{h,o}$ and $\dot{Q}_u$ for each type of collectors

Fig. 4.6a and Fig. 4.6b illustrate the comparison of monthly average of power output ($\dot{W}_{avg}$) results for each type of solar collector each month using the R245fa and R123 working fluids, respectively. It can be seen in the two figures that the PTC-type solar collector produces the highest $\dot{W}_{avg}$ each month compared to other types of solar collectors (EFPC, ETC) using either R245fa or R123 working fluid. While the highest $\dot{W}_{avg}$ produced in August was 45.5 kW and 32.33 kW using PTC for each of the working fluids R245fa and R123, respectively. It is caused by the large Gb in August compared to other months, so it can convert heat into an outlet temperature received by the solar collector. At the same temperature and Gb input, the PTC has a higher potential to generate power compared to EFPC and ETC.

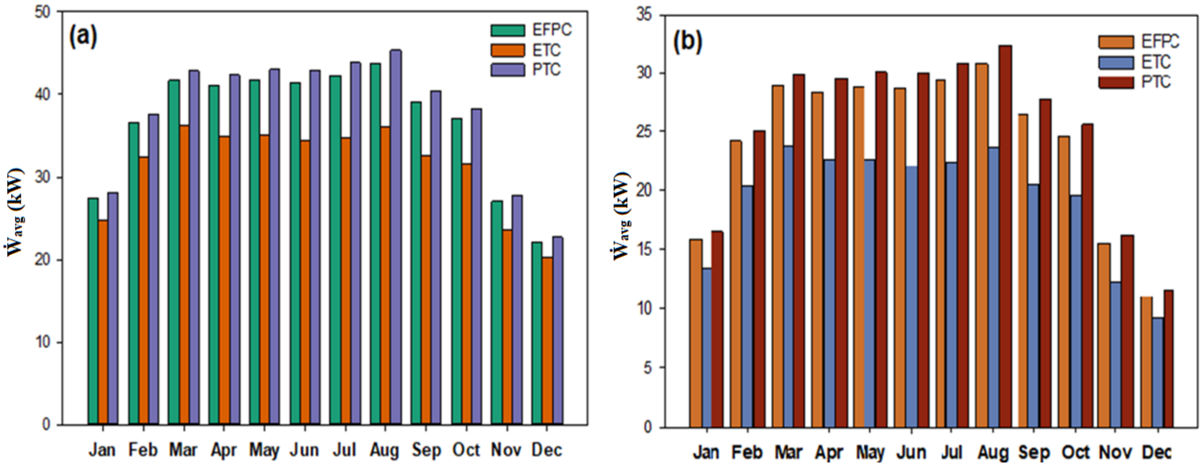

Fig. 4.6. Monthly profile of $\dot{W}_{avg}$ results of each solar collector: a) R245fa, b) R123

The net output power of the waste heat recovery system may be evaluated during the preliminary study. This net output power may be estimated by subtracting the pump power ($\dot{W}_{pump}$) from the expander power ($\dot{W}_{exp}$). The overall efficiency of the cycle ($\eta_{thermal}$), which represents the system's net output power ($\dot{W}_{net}$) per input heating power, was another metric used to quantify the performance of waste heat recovery as power production. In this sub-section, we will discuss the performance generated by the solar-ORC system for the average time in June 2021. Fig. 4.7 shows the same trend results in $\dot{W}_{net}$ and $\eta_{thermal}$ over time with different fluids.

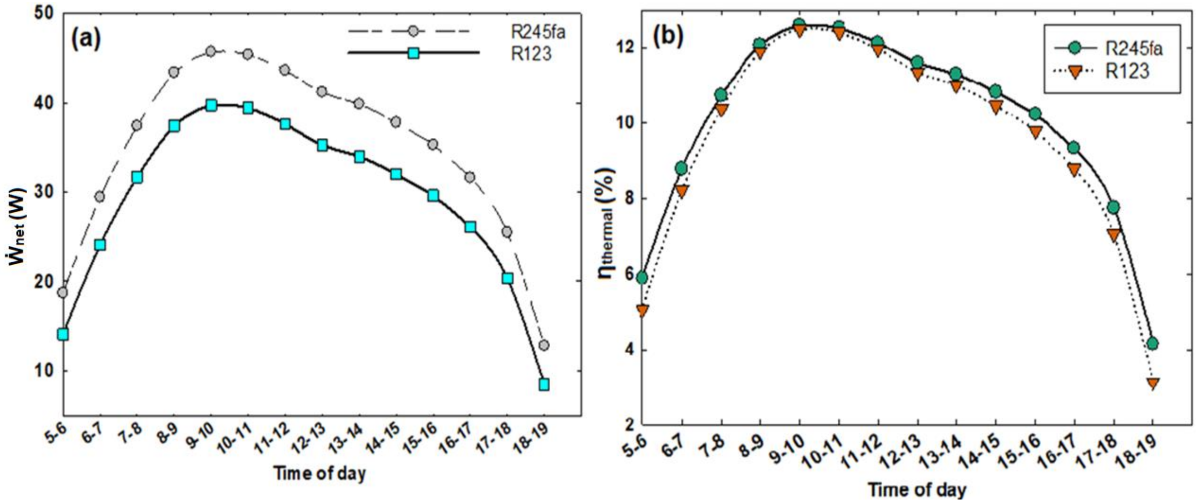

Fig. 4.7 Hourly profile performance for each working fluid: a) $\dot{W}_{net}$, b) $\eta_{thermal}$

Fig. 4.7a shows that the highest $\dot{W}_{net}$ generated is at 9-10 o'clock, with values of 45.82 W and 28.17 W for R245fa and R123, respectively. Whereas at the same hour (9-10) in Fig. 4.7b, the $\eta_{thermal}$ of R123 produced a higher value than R245fa with 13% and 12.5%, respectively. This is on account of the value of global solar irradiation (Gb) peaks at 9-10 o'clock, affecting the ORC's Wnet and $\eta_{thermal}$ results. At the same time, the enthalpy difference (h) owned by the two working fluids (R245fa and R123) enters the turbine and pump, which affects the amount of $\dot{W}_{net}$ between both working fluids.

Fig. 4.8 depicts the acquired modelling results for the TES-evaporator. The plots show the modelling results for various working fluids and selected solid materials used as TES materials for adjusting the dimensionless TES material mass parameter $\zeta(T)$ (see Section 3.4.1) and TES-evaporator temperature at the output (T_{TES}) at different working fluids (R245fa and R123). The outcome allowed us to compare and estimate the amount of TES materials required in the TES system. For example, the value of the (T_{TES}) parameter specifies the mass of the TES material necessary to warm and evaporate 1 kg of low-boiling working fluid in the ORC system. The simulated result is shown in Fig. 4.8a for R245fa working fluid, demonstrating that the lower the $\zeta(T)$ value, the less TES material is required to evaporate working fluid inside the ORC system. While Fig. 4.8b for R123 working fluid shows the value of the dimensionless mass parameter $\zeta(T)$ tends to be constant along the T_1, rise in the evaporator even though in detail value of $\zeta(T)$ for each TES material shows the same trend with R245fa.

Based on Fig. 4.8a, the acquired values of the $\zeta(T)$ parameter vary between 1.43 and 10.98, with the maximum result of $\zeta(T) = 10.98$ achieved for Monel metal as TES material and R245fa as working fluid inside the ORC system at a temperature of 341.3 K. Furthermore, for the same working fluid (R245fa), the TES-evaporator temperature at 369.55 K yields a lower $\zeta(T) = 1.98$ using the organic PCM. Meanwhile, for Fig. 4.8b, the obtained values of $\zeta(T)$ vary between 0.41 and 2.43 at the same temperature range for R123. The highest of $\zeta(T)$ is achieved by monel metal with the value of 2.43 at a temperature of 341.3 K. Moreover, the organic PCM results in the lowest of $\zeta(T)$ with a value of 0.41 at the TES-evaporator around 369.4 K. It is indicated in the plot that the combination of Monel metal and R245fa has the largest sizing parameter and the combination of R123 and organic PCM has the lowest sizing parameter.

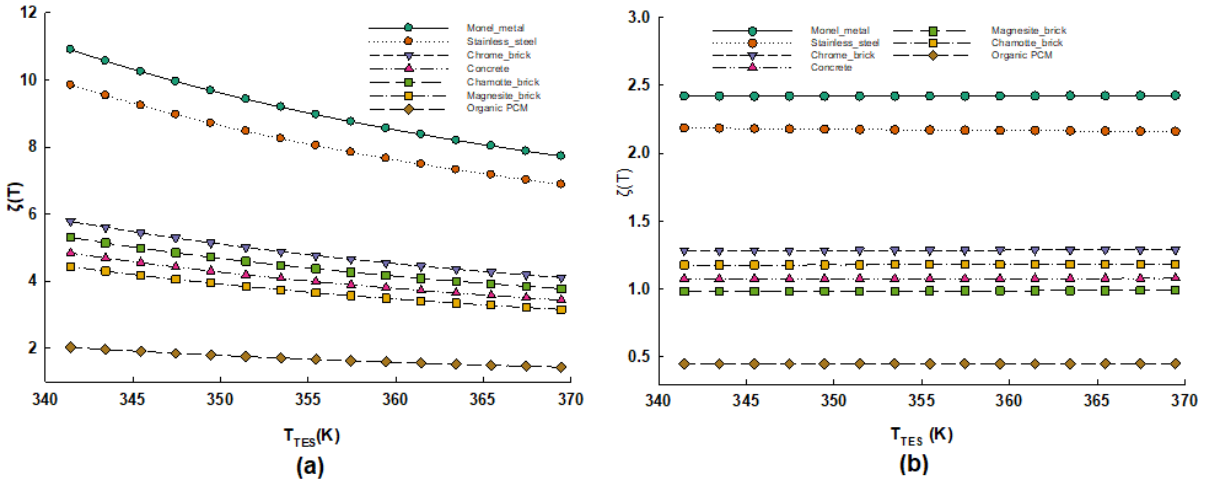

(a) (b)

Fig. 4.8. The temperature profile of *ζ(T)* for each TES material: a) R245fa, b) R123

The above analysis shows that organic PCM has a low *ζ(T)* value for both working fluids (R245fa and R123), which means that PCM requires less material to store and transfer heat to the working fluid that requires temperature (358.15-370.15 K). Meanwhile, Fig. 4.9 shows the temperature profile of *ζ(T)* for nine products of organic PCMs for the two working fluids (R245fa and R123), which show the same trend. The greater the TES temperature, the smaller the *ζ(T)* value. Fig. 4.9 shows that P-bromophenol shows the highest *ζ(T)* value at 358 K with values of 2.58 and 2.02 for R245fa and R123, respectively. Meanwhile, N-Octacosane showed the lowest *ζ(T)* value at 370 K of 1.26 and 1.02 for the working fluids R245fa and R123, respectively. However, for R123, the range of values for *ζ(T)* is lower than that for R245fa. It is caused by the cp value that each organic PCM has and the difference in enthalpies owned by the two working fluids that enter the evaporator.

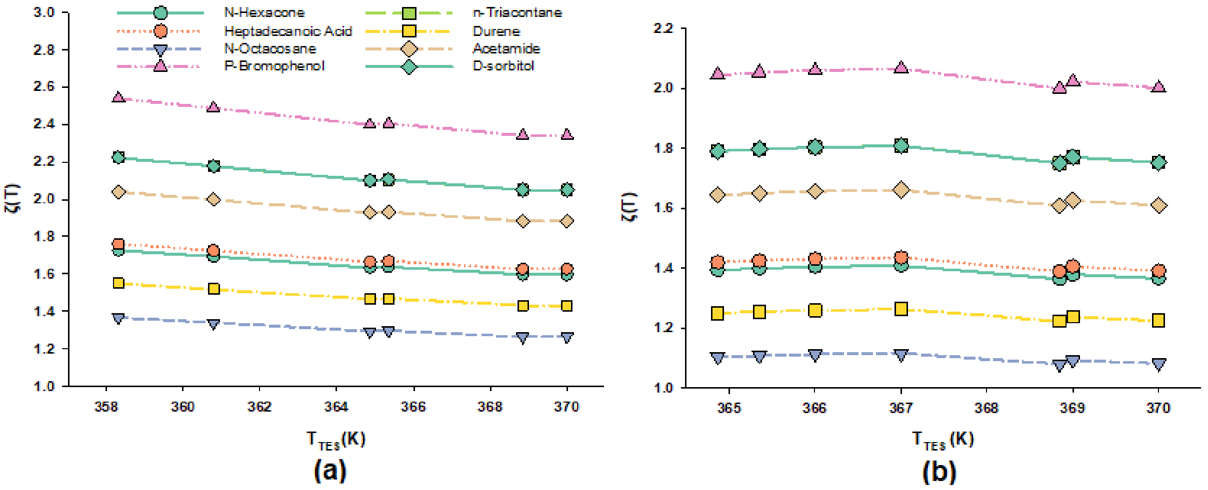

(a) (b)

Fig. 4.9. The temperature profile of *ζ(T)* for each organic PCM: a) R245fa, b) R123

Fig. 4.10a and Fig. 4.11a depict the proportionate breakdown of exergy destruction in each component for R245fa and R123, respectively. As predicted, the bulk of the exergy is lost in the solar collector array. This is an unavoidable result of converting solar radiation to enthalpy at a temperature significantly lower than the apparent temperature of the solar as an exergy source for practical reasons. Examining the breakdown of exergy destroyed in the ORC components only (Fig. 4.10b, Fig. 4.11b) and comparing the exergy efficiencies with those for the non-regenerative ORC system studied in Mago et al., (2008). (1) The exergy efficiency of the ORC components in the current study is generally lower; and (2) the relative percentages of exergy destroyed are also different, with the condenser in particular accounting for a significantly greater share of the overall exergy destruction in our study. The former of these results might be attributed to the lower temperature functioning of the system under consideration, as well as the pump and the turbine's low isentropic efficiencies due to their smaller size and positive displacement behaviour.

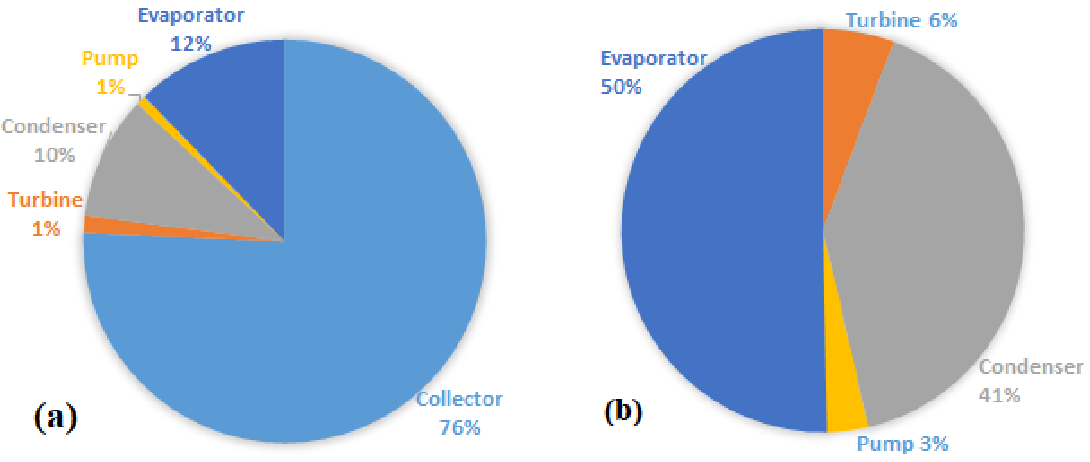

Fig. 4.10. Percentage of exergy destruction of R245fa: a) with solar collector, b) without solar collector

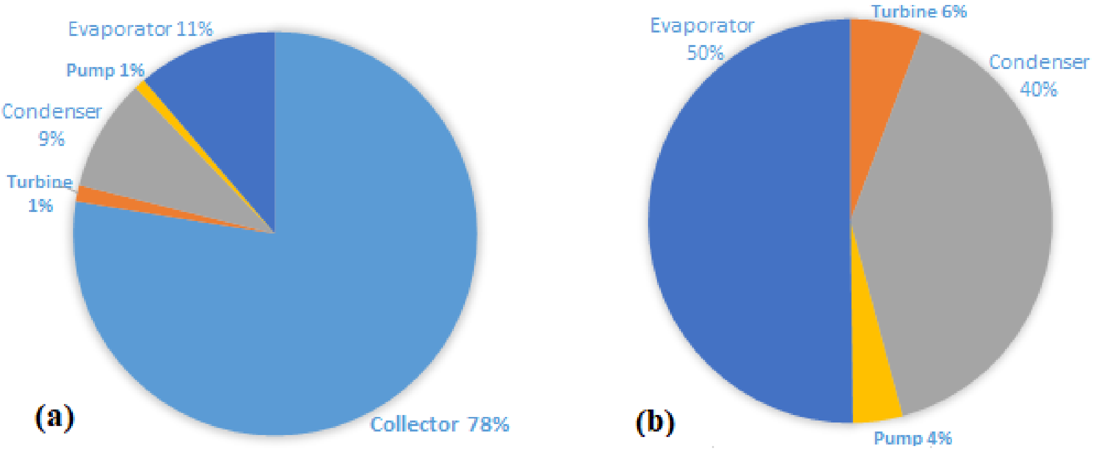

Fig. 4.11. Percentage of exergy destruction of R123: a) with solar collector, b) without solar collector

Table 4.1 details the exergy values of each component resulting from two working fluids (R245fa and R123). The evaporator is the component with the most significant exergy destruction, with 3994.7 W for R245fa and 4363.4 W for R123. The evaporator's exergy loss mainly results from the irreversibility of heat transfer across a little temperature difference. The substantial exergy loss also reduces the degree of thermodynamic perfection, which is lowest in the evaporator, 62.7% for R245fa and 56.15% for R123. On the other hand, the evaporator has the most significant effect coefficient, reflecting that the evaporator is the critical component of the analysed basic ORC. The condenser is the second component that has a more significant impact on Solar-ORC performance. It has the third-highest influence coefficient of 22.8% for R245fa and 20.9% for R123. However, compared to the collector and evaporator, the degree of thermodynamic perfection and energy efficiency is higher. Whole system exergy loss is 9.6-9.8 kW, thermodynamic perfection is 69-70%, and the total exergy efficiencies are 66.7% and 63.7% for both working fluids (R245fa and R123), respectively. According to the data reported in Table 4.1, R245fa has greater thermal and energy efficiencies than R123 for the same heat rate available for the evaporator from the solar collector, minimising overall system exergy destruction and enhancing the degree of thermodynamic performance.

Table 4.1. Exergy performance result of Solar-ORC

Component	R245fa						R123					
	Ex_D (W)	Ex_{use} (W)	Ex_{ava} (W)	ν (%)	β (%)	η_{Ex} (%)	Ex_D (W)	Ex_{use} (W)	Ex_{ava} (Watt)	V (%)	B (%)	η_{Ex} (%)
Collector	1869	6873.2	8742.2	79.8	41.8	58.6	1869	6873.2	8742.2	79.8	43.1	52.1
Turbine	3.77	459.3	463.1	99.3	2.2	99.2	3.43	415.4	418.8	99.1	2.03	99.2
Condenser	3936	132.6	4411.2	10.8	22.8	3.01	3459.1	102.5	3904.3	11.4	20.9	2.63
Pump	0.06	9.38	9.44	99.6	0.04	99.4	0.04	5.32	5.36	99.6	0.02	99.3
Evaporator	3994.7	4618.1	6873.2	62.7	33.1	73.5	4363.3	4101	6873.2	56.15	33.9	65.3
Total	9803.6	12092.5	20499.1	70.6	20	66.7	9694.9	11497.5	19943.8	69.4	20	63.7

4.2.2. Utilization of solar ORC integrated with PCMs in Indonesia condition

The climatic conditions in Bandung exhibit greater consistency in daily and monthly solar irradiation compared to the maximum solar irradiation. August emerges as the peak month for both maximum and average global solar irradiation, with values reaching approximately 150 kWh/m² and 70 kWh/m², respectively. Furthermore, the sunshine duration in August exceeds 6 hours, resulting in higher temperature increases compared to other months, with a maximum temperature of 26 °C and a daily average of 23°C. Based on the operating conditions, data, and equations outlined in Sub-chapter 3.3.2, the findings are discussed as follows.

Fig. 4.12a compares the value of average daily of heating product ($\dot{Q}_u$) generated by ETC in January, April, and July. The maximum $\dot{Q}_u$ is generated in July at roughly 94.5 kW, followed by January and April at 75 and 82 kW, respectively. Fig. 4.12b demonstrates that July has a higher solar collector efficiency (10% at 433 K) than other months (January and April) at the same temperature. It is because the value of solar irradiation has a far greater influence in Eq. (3.35) than the value of ambient temperature. So, in the next computation, the ETC outlet temperature values will be utilised as the solar collector's variable heat source.

The preliminary research may include an assessment of the solar-ORC system's net output power. The net output power may be determined by subtracting the pump power from the expander power. Another statistic used to assess the success of waste heat recovery as power generation was cycle efficiency, which indicates the system's net output power per input heating power. In this subsection, we will look at the solar-ORC system's average daily performance in January, April, and July 2021.

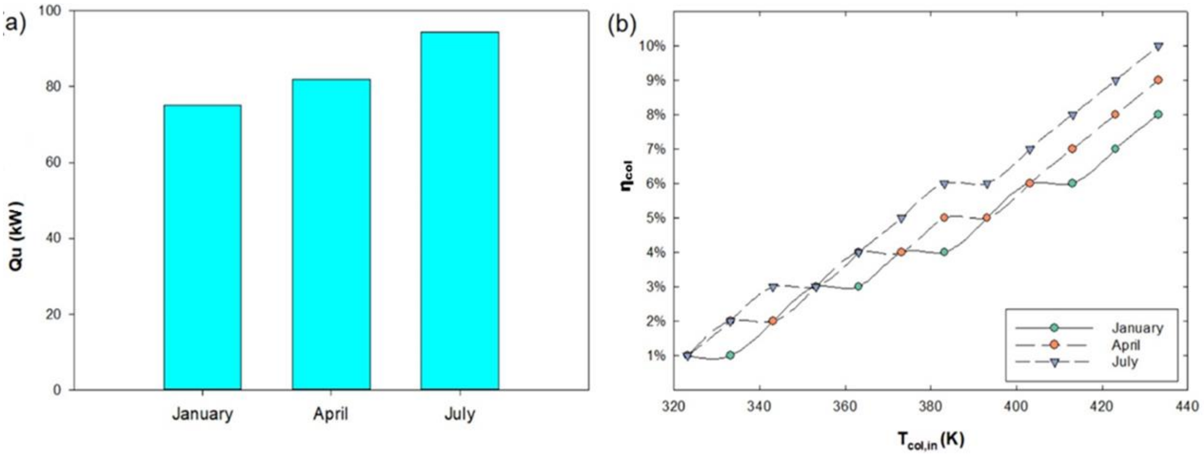

Fig. 4.12. The performance of ETC's solar collector in monthly profile: a) $\dot{Q}_u$, b) η_{col}

Fig. 4.13 displays consistent trend results in average daily power ($\dot{W}_{avg}$) and efficiency thermal ($\eta_{thermal}$) with time for several fluids. Fig. 4.13a demonstrates that the maximum $\dot{W}_{avg}$ created occurs in July 2021 for all working fluids, with R134a generating 685 W, followed by R410a and R245fa at 660 and 545 W, respectively. Fig. 4.13b displays the monthly profile of $\eta_{thermal}$, with R245fa having the highest value of 7.45%, followed by R134a and Propane at 6.1 and 5.35%, respectively. The performance model was validated by Permana et al., (2023) and Valencia Ochoa et al., (2023) which showed the same trend, namely from January to July, the $\dot{W}_{avg}$ and $\eta_{thermal}$ values increased along with the increase in solar irradiation in each month and region. For research conducted by Valencia Ochoa et al., (2023), where the research location was in Las Flores, Spain, which has an average solar radiation of 700-800 W/m^2. While the research location conducted by Permana et al., (2023) was in Gödöllő, Hungary, which has an average solar radiation of 400-500 W/m^2.

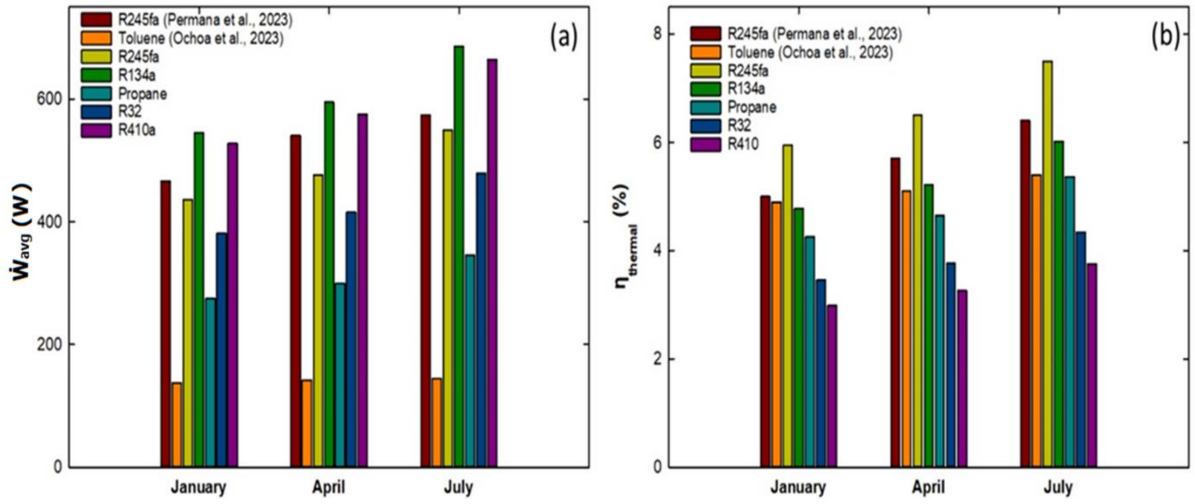

Fig. 4.13. Daily profile of the performance of solar-ORC in different working fluids: a)$\dot{W}_{avg}$, b) $\eta_{thermal}$

A parametric study was conducted to explore the impact of the following factors on the system's electrical output: (1) ORC working fluid flow-rate ($\dot{m}_{wf}$), (2) expander isentropic efficiency

(η_{iso}), and (3) condenser temperature (T_{cond}); the calculation was performed for both the "daily average" and the ETC's model system with operating fluid fluctuations. During each simulation run, one parameter was altered while the others remained stable. The purpose is to identify critical system parameters and understand their impact on system performance in order to maximise total work output and estimate the ideal energy and efficiency settings for the daily moderate operation. The three figures (Fig. 4.14a, Fig. 4.15a, Fig. 4.16a) show that Propane is the working fluid that produces the highest daily average of net power ($\dot{W}_{avg}$) based on mass flow rate ($\dot{m}_{wf}$), isentropic efficiency (η_{iso}), and condensed temperature (T_{cond}). It is caused by the type of Propane working fluid, which is isentropic, where at low temperatures in the evaporator, the enthalpy of Propane during the expander expansion process is the highest compared to other working fluids. In this test, the expander appears to provide modest power (less than 100 kW). According to recent study, volumetric and turboexpanders appear to be attractive solutions for solar thermal collectors (Badr et al., 1984; Imran et al., 2016; Weiß, 2015). Small ORC expanders must handle a wide range of selection criteria, including economics, market availability, reliability, maintainability, and other essential technical challenges.

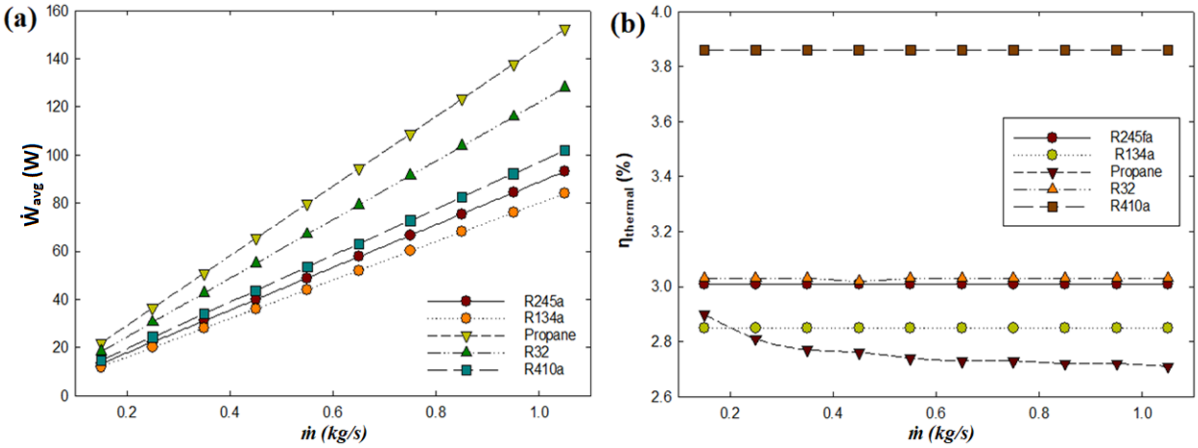

Fig. 4.14. The effect of $\dot{m}$ against the solar-ORC's daily performance for every working fluid: a) $\dot{W}_{avg}$, b) $\eta_{thermal}$

Fig. 4.14b and Fig. 4.15b show that the difference in $\dot{m}_{wf}$ and η_{iso} against $\eta_{thermal}$, which for Fig. 4.16b, the $\eta_{thermal}$ tends to be constant for the five working fluids, Propane experiences a decrease in thermal efficiency when the mass flow rate increases. However, R410a is the working fluid that produces the highest $\eta_{thermal}$, with 3.8%, on the same trend as Propane and R245fa for $\dot{m}_{wf}$ from 0.1-1.1 kg/s, with 2.7% and 3%, respectively. Therefore, the same results were shown by R410a in Fig. 4.15b, which produced the highest of $\eta_{thermal}$ (2.2-5.2%) in the η_{iso} (0.2-0.9) range compared to other working fluids such as Propane and R245fa with value of (1.5-3.7 %) and (1.9-3.9 %), respectively. This proves that even though propane and R245fa are the working fluids with the highest $\dot{W}_{avg}$, utilizing heat in the evaporator and large pumps to increase pressure still requires much energy. Moreover, in Fig. 4.16, both $\dot{W}_{avg}$ and $\eta_{thermal}$ show the same trend, namely, the higher the T_{cond}, the lower the $\dot{W}_{avg}$ and $\eta_{thermal}$ produced. The difference is that in Fig. 4.16a, Propane is the working fluid that produces the highest $\dot{W}_{avg}$, while in Fig. 4.16b, R134a is the working fluid that produces the highest $\eta_{thermal}$.

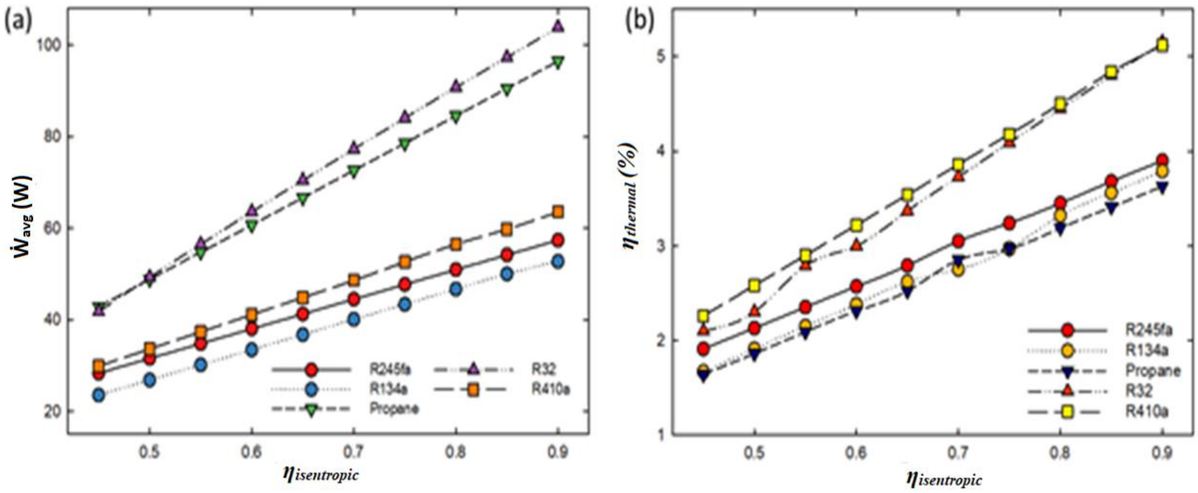

Fig. 4.15. The effect of η_{iso} against the solar-ORC's daily performance for every working fluid: a) $\dot{W}_{avg}$, b) $\eta_{thermal}$

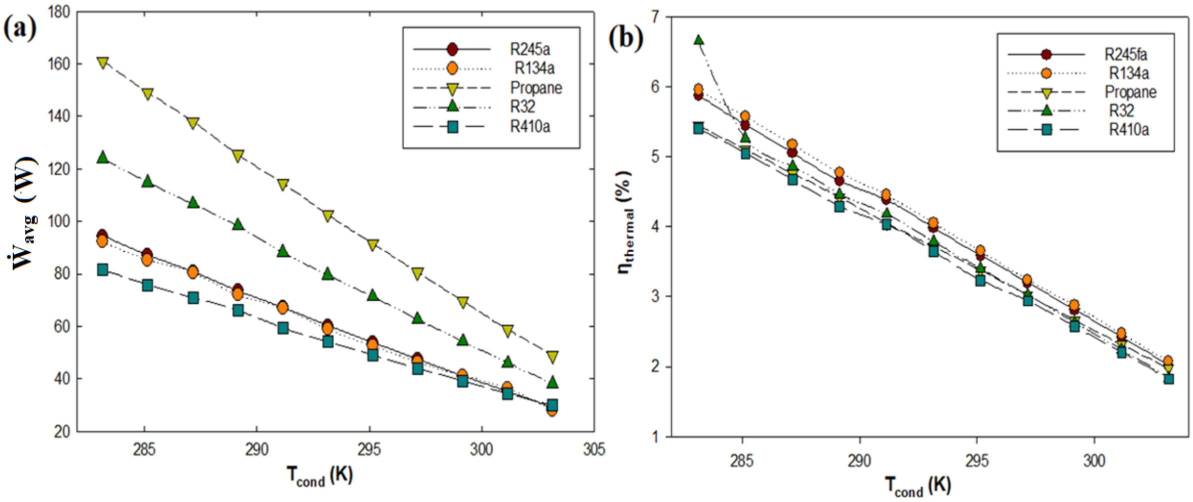

Fig. 4.16. The performance of T_{cond} against the solar-ORC's daily performance for every working fluid: a) $\dot{W}_{avg}$, b) $\eta_{thermal}$

Fig. 4.17 depicts the proportionate breakdown of exergy destruction in every component for R245fa, R134a, Propane, R32, R410a, respectively. As expected, the evaporator consumes the most exergy for all working fluids, with R134a accounting for about 364.9 W, followed by R410a, R245fa, R32, and Propane at 363.2, 360.1, 329.7, and 289 W, respectively. Where, the heat transfer from the heat source to the fluid occurs in this component. So, the possibility of exergy being destroyed is enormous. There is a need to conduct a pinch analysis and select the correct type of evaporator, in other to the damaged exergy is not too large. Fig. 4.18 is the exergy efficiency of each component with different working fluids where the performance from the exergy analysis, the opposite of the exergy destroys in each component. Fig. 4.18 shows that the expander can utilize exergy optimally. In this case, R245fa can utilize exergy better by 95.7% compared to working fluids such as Propane and R134a with 95.4% and 80.6%, respectively.

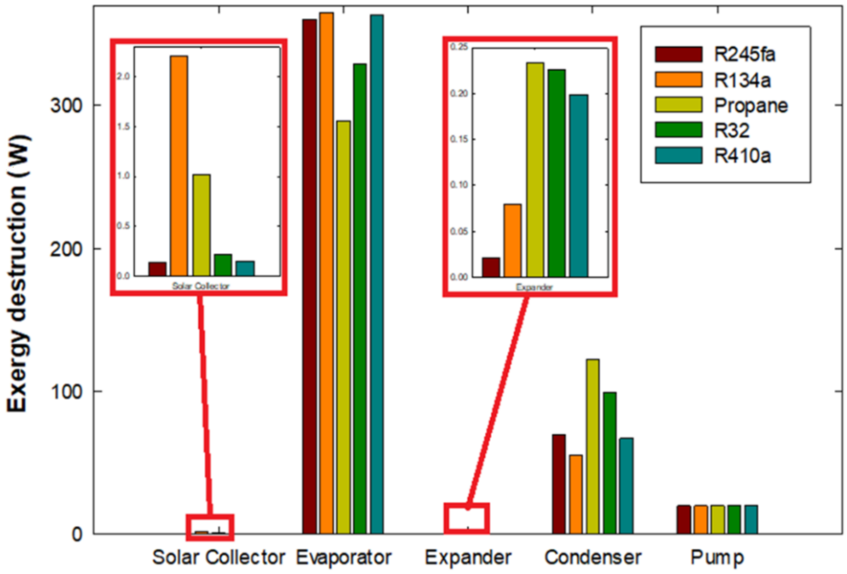

Fig. 4.17. The performance of exergy destruction of each component in different working fluids

Investigating the one by one of exergy destroyed in the ORC components alone (Fig. 4.17) and comparing the exergy efficiencies (Fig. 4.18) to those for the non-regenerative ORC system examined by (Mago et al., 2008). (1) The exergy efficiency of the ORC components in the current study is typically lower; and (2) the relative percentages of exergy destroyed vary, with the condenser accounting for a much bigger share of total exergy destruction in our study. The former of these results might be attributed to the system's lower temperature operation, as well as the pump and expander's poor isentropic efficiencies caused by their smaller size and positive displacement behaviour.

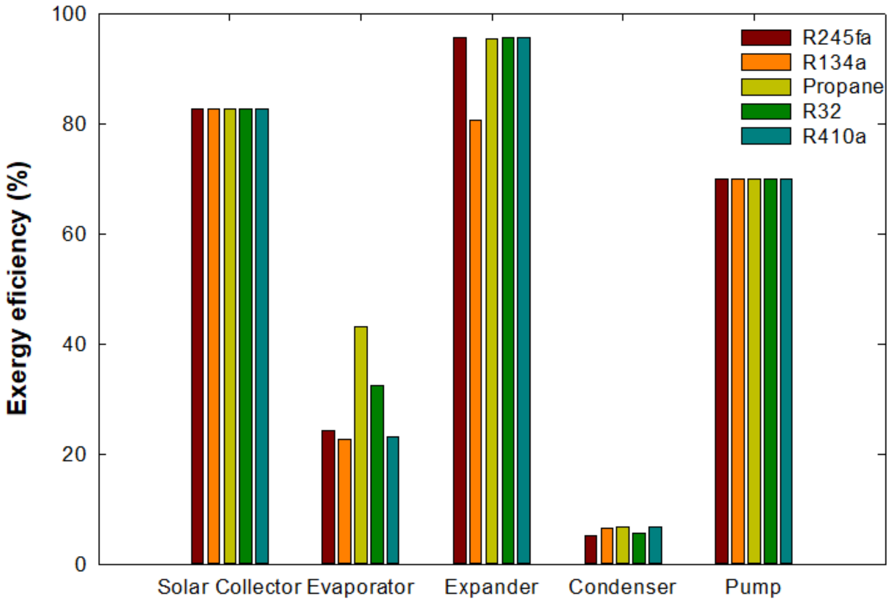

Fig. 4.18. The performance of exergy efficiency for each component of different working fluids

Fig. 4.19 shows the performance of several exergy parameters, such as exergy destruction, EWR, EEF, and ESI, against temperature changes with different working fluids. In this subsection, the role of exergy will be more exploited in relation to EWR, EEF and ESI which are parameters where the solar-ORC system impacts the environment and sustainability. Fig. 4.19a shows the same trend for the five working fluids, where there is an increase in exergy destruction with increasing temperature. At temperatures of 320 - 330 K, Propane experiences the biggest destruction energy compared to other refrigerants. At the highest temperature (356.4 K), R410a and R245fa are the working fluids with the highest destruction energy values of 507.7 and 504.3 kW, respectively.

EWR is the proportion of total waste exergy to total intake exergy, and practically all working fluids have the same EWR trend. Fig. 4.19b shows the decrease of EWR along with the increase in temperature. If seen in more detail, in the low-temperature range (320-330 K), Propane has the highest EWR value compared to other working fluids. However, as the temperature increases, as does Propane, the EWR produced by the five working fluids continues to decrease. In this parameter, R32 has the smallest EWR value, which means it has a minor influence on the environment compared to other working fluids.

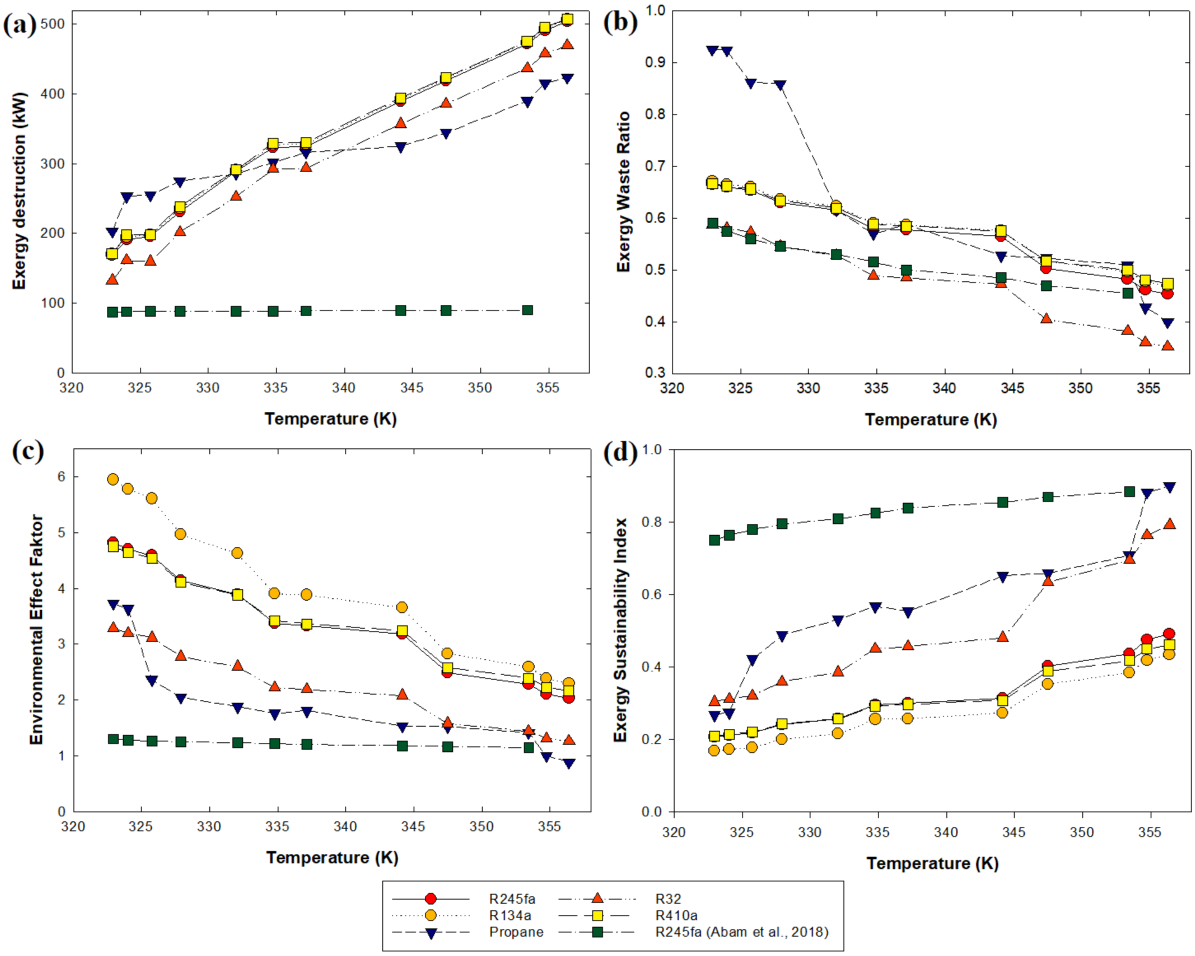

Fig. 4.19. Exergy performance of each parameter for different working fluids: a) exergy destruction, b) EWR, c) EEF, d) ESI

The EEF that may be viewed as a measure of environmental harm caused by waste exergy destruction (Midilli et al., 2012). Fig. 4.19c depicts the EEF value of each working fluid shows a decrease in EEF as temperature increases, where R134a is the working fluid that produces the highest EEF value, and Propane produces the lowest EEF value at the same temperature.

This means that Propane is the most sustainable working fluid. The exergy sustainability index is a feasible measure developed as a supplement to the environmental impact factor (Midili and Dincer, 2009). Fig. 4.19d shows the trend of ESI, where the temperature increases the ESI value of each working fluids increases. Propane is the working fluid with the highest ESI value, unlike R134a, which has the lowest ESI value at the same temperature trend. Meanwhile, the two environmental parameters (EEF and ESI) show that R134a harms the environment and sustainability. So, it is not surprising that European Chemicals Agency (ECHA), the use of R134a is starting to be banned included R125, R143a, and the HFOs R1234yf and R1234ze impact almost all new and existing low GWP HFC/HFO refrigerant mixes (Everitt, 2023). Furthermore, the results of the exergy sustainability indicator were confirmed by a study conducted by (Abam et al., 2018), who used R245a working fluid by comparing ORC cycle configurations from oxy-fuel sources, where a more stable trend was obtained in changes in EWR, EEF, and ESI values.

Fig. 4.20a and Fig. 4.20b show the required PCM storage volume (100-450 L) for partial storage and volume (300-1500 L) for full storage as a function of the PCM melting temperature (T_{TES}) and volumetric heat capacity (ρ_{hsl}) using the detailed properties of organic and inorganic PCM (see Table 3.9). The required storage volumes for the partial-storage and full-storage strategies are compared using Bandung's climate on July 2021 and using R245fa as a working fluid since it generates the highest system efficiency. For the full-storage strategy, higher PCM-TES lead to more minor storage volume requirements because the lower solar collector efficiency means the daily solar energy yield is also lower. For the partial-storage strategy, the melting temperature has a smaller effect on storage volume because the TES is sized for the difference in the solar energy yield between the peak and average days rather than the total.

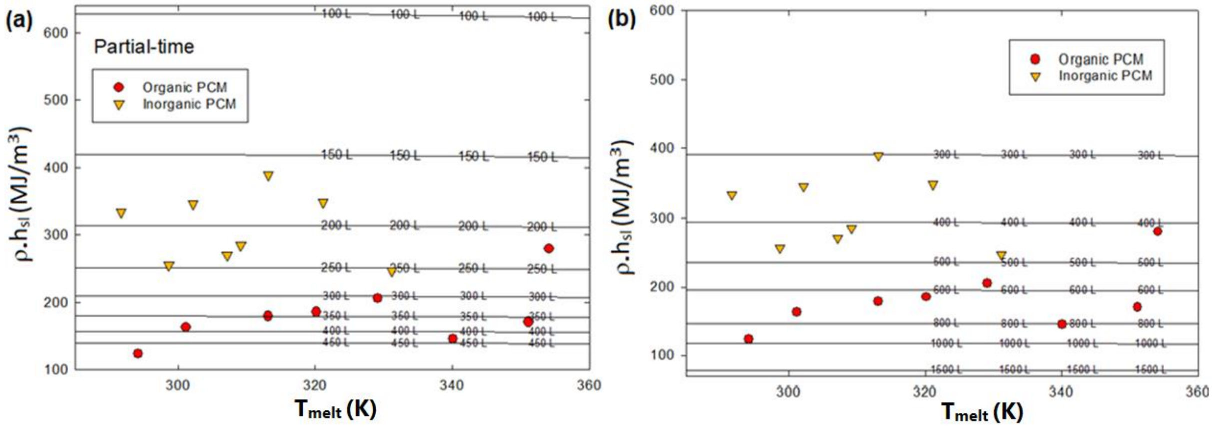

Fig. 4.20. TES volume required for a solar-ORC based on different PCMs for specific heat capacity: a) partial storage, b) full storage

The needed storage space is also strongly influenced by the volumetric latent heat of the PCM ($\rho.h_{sl}$), which is depicted on the y-axis. The plots also show a variety of current organic and inorganic PCM materials with known heat capacity and melting temperatures (T_{melt}). During phase shift, inorganic PCMs usually have larger volumetric heat capacities (250-400 MJ/m^3) than the rest of organic PCMs (120-270 MJ/m^3). It can be seen in both figures that organic PCM has the widest distribution in the T_{melt} range (285-360 K), but it has a lesser volume capacity of around 200-450 L for partial time and 950-1650 L for full-time compared to inorganic PCM has a higher volumetric heat capacity (250-400 MJ/m^3) but has a smaller volume capacity around 150-250 L for partial time and 650-1100 L for full-time with a reasonably low T_{melt} range (285-335 K). So, it is a suitable choice to use inorganic PCM for Indonesian households as the volume required is smaller and suitable with reservoir tanks that commonly used in housing and located it on the roofs of houses.

Fig. 4.21shows the performance of the TES-evaporator using various PCMs based on hourly time, which has a 250 L capacity. The Fig. 4.21c shows the difference in melting temperature of each PCM, we can see the temperature of the PCM when filling with heat starts when solar radiation begins, and it is from 5.00 to 18.00 with temperatures from 293.15 - 393.15 K and in the same period, the heat stored by the PCM increases to 75,000 kJ (Fig. 4.21a). After the PCM is fully charged until 18.00, then the ORC starts working at night, so it can be seen in Fig. 4.21a and Fig. 4.21c that both the heat and the T_{TES} decrease and the power used by the ORC begins to be used starting from 18.00 with the highest net power reaching 600 W (Fig. 4.21b) and slowly decreases in terms of power, heat and PCM's temperature.

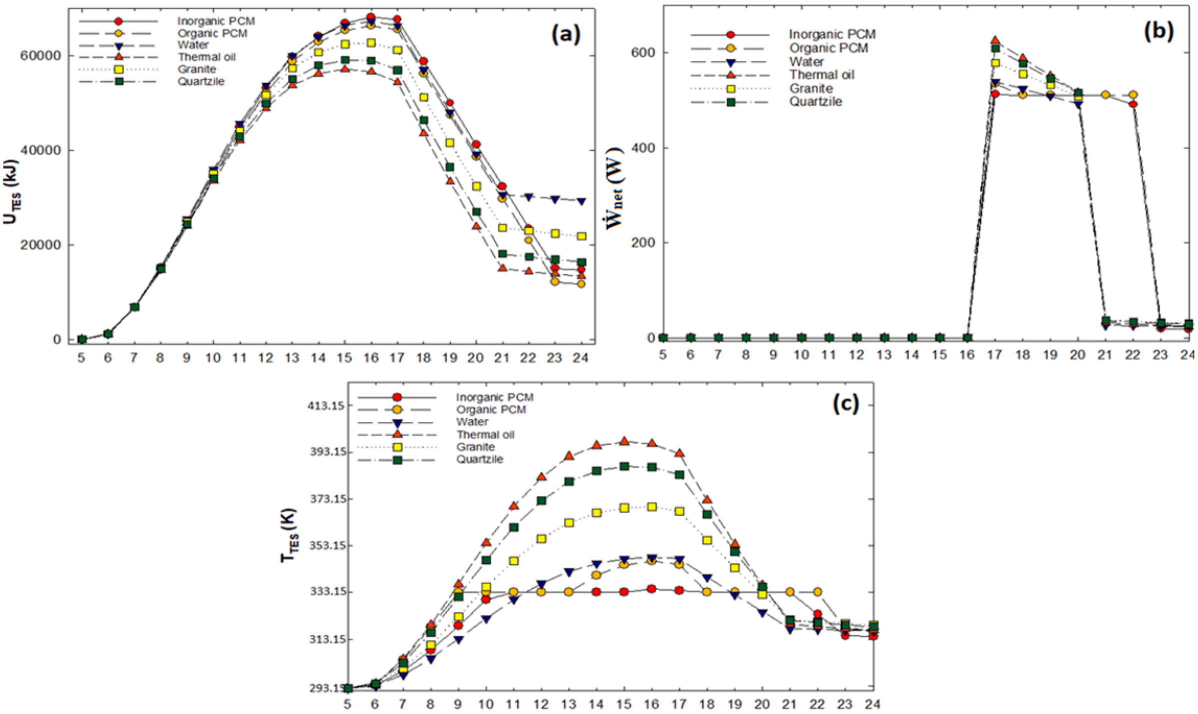

Fig. 4.21. The performance of small solar-ORC (500 W) with operated using full-time for capacity of 250 L: a) U_{TES}, b) $\dot{W}_{net}$, c) T_{TES}

Other PCM is water has a lower maximum temperature than the other sensible storage media and the organic PCM, but not the inorganic PCM, due to its high specific heat capacity; however, the storage temperature is still high enough that significant pressurisation (16 bar at 473 K) would be required to keep the water in the liquid phase. Thermal oil has the lowest thermal capacity (~55000 kJ) yet it generates the highest of $\dot{W}_{net}$ and it generates an average net power of ~600 W around 5 hours continuous operating time. It has the most significant daily temperature variation, the highest maximum storage temperature, the highest intake temperatures to the collector array, and the lowest collector efficiency. Furthermore, due to enhanced superheating at the expander intake, higher T_{TES} result in more significant initial power outputs at the start of the ORC operation period (Fig. 4.21b). However, the overall labour output and operating time duration are greater for materials with lower storage temperatures.

4.3. Biomass-ORC

4.3.1. Thermoeconomic analysis of ORC from Napier grass biomass

Napier grass was selected as the biomass feedstock due to its adaptability to a wide range of climates and soil conditions in Indonesia, coupled with its high heating value (HHV) of 16.56–18.11 MJ/kg. The key ORC components, including the expander, condenser, pump, and evaporator, were analysed in detail to evaluate the cycle's performance. This analysis not only influences the performance outcomes but also impacts the thermoeconomic results. Based on the available data, operating conditions, and equations are provided in sub-chapter 3.4.1, the findings are discussed as follows.

The effect of condensation temperature (T_{cond}) on the maximum power ($\dot{W}_{exp}$) produced by the expander can be analysed to determine the appropriate capacity of the centrifugal chiller to be converted into an ORC system. Fig. 4.22 shows the characteristic of the change in condensation temperature against the power produced in the ORC system with the expander capacity variations from 350 TR to 550 TR on different working fluids (R123 and R245fa).

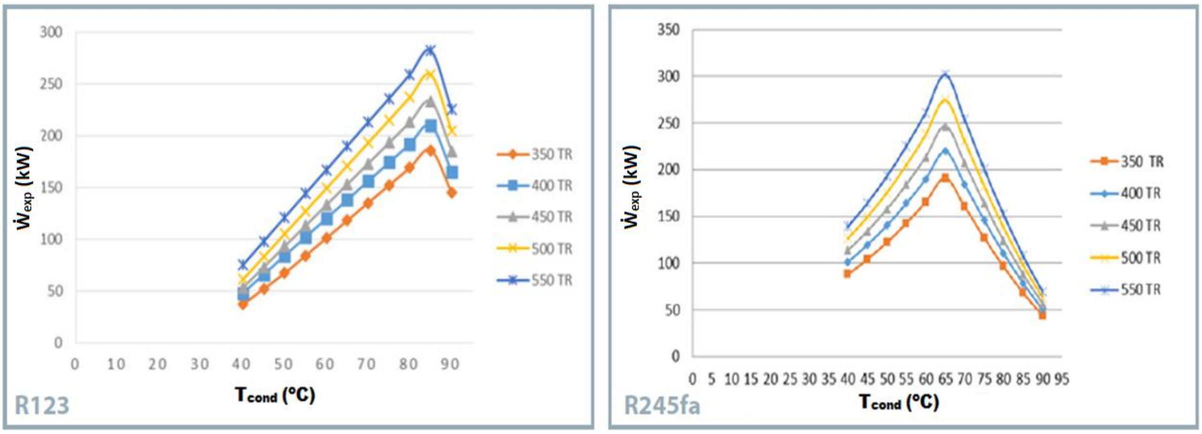

Fig. 4.22. Performance ($\dot{W}_{exp}$) result in different condensation temperature (T_{cond}) for expander capacity: a) R123, b) R245fa

Fig. 4.22a shows that for the working fluid R123, the condensation temperature which produces the maximum expander circulation is 85 °C. At the same time, the expander power, which produces more than 200 kW of power, is obtained by using a centrifugal chiller capacity of 500 TR. Taking into account the generator and motor losses and the pump's power required, the appropriate expander to produce a net electrical output of 200 kWe is 550 TR. Fig. 4.22b indicates that the condensation temperature that produces the most significant power for the working fluid R245fa is 65 °C. The expander power of more than 200 kW is obtained by using a capacity of 450 TR. By calculating the same losses (generator, motor, and pump), the selected capacity to produce a net electrical output of 200 kWe is 500 TR. However, in this study, the capacity of the output power generated by the ORC has been determined, which is around 200 kWe. Table 4.2 shows the result of ORC simulation containing each state of parameters and the amount of thermal efficiency obtained by the two working fluids (R123 and R245fa). We can see the highest $\dot{W}_{exp}$ obtained by R245fa with 271.1 kW, followed by R123 with 269.7 kW. As for the ORC performance, $\eta_{thermal}$ was 7.04% achieved by R123, followed by R245fa with 6.62%.

Table 4.2. The optimum result of ORC simulation

Working fluids	$\dot{m}_{wf}$ **(kg/s)**	$\dot{m}_{HTF}$ **(kg/s)**	$\dot{m}_{cw}$ **(kg/s)**	$\dot{m}_{air}$ **(kg/s)**	$T_{c,o}$ **(°C)**	$\dot{Q}_{cond}$ **(kW)**	$\dot{Q}_{evap}$ **(kW)**	$\dot{W}_{exp}$ **(kW)**	$\dot{W}_{FP}$ **(kW)**	$\eta_{thermal}$ **(%)**
R123	18.89	16.56	31.45	72.18	54.80	3329.03	3581.11	269.7	17.60	7.04
R245fa	15.32	11.35	48.16	78.31	47.43	3609.86	3865.75	271.1	15.25	6.62

Fig. 4.23 illustrates that the electrical output produced by the two working fluids, R123 and R245fa, is relatively similar, with R123 achieving a slightly higher output of 238.78 kWe compared to R245fa's output of 237.82 kWe. This minor difference in electrical output also extends to the electricity demands of certain components within the ORC system. For instance, equipment such as feed pumps and HTF pumps, which are integral to system operation, consume slightly more electricity when the working fluid is R123 compared to R245fa. Conversely, for the cooling tower fan and cooling tower pump, the trend reverses, with R245fa demonstrating higher electricity consumption. Specifically, the cooling tower fan and pump using R245fa require 14.09 kWe and 4.89 kWe, respectively, whereas the same components with R123 consume slightly less electricity, at 13.86 kWe and 3.33 kWe, respectively. This comparative analysis is emphasizing the need for careful selection based on the specific thermodynamic and operational requirements of the ORC system.

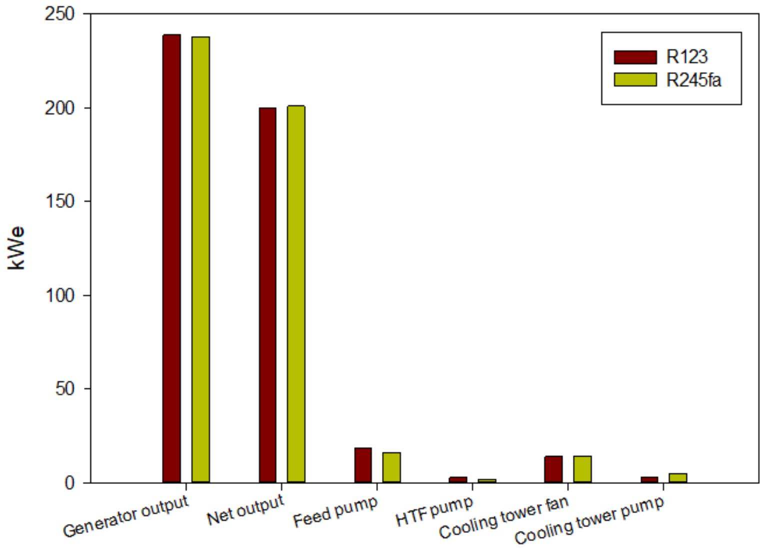

Fig. 4.23. Electrical consumption of each component

Based on Table 4.3, the investment cost of components with R123 requires the most considerable cost between the two types of working fluids. R123 requires an investment cost of ORC power plant components of 3230.28 USD/kWe, compared to R245fa with 2311.68 USD/kWe. As operating conditions in the condenser have the greatest effect on the difference in investment costs that will impact the cooling tower investment costs. This condition occurred because the calculation of the cooling tower investment costs based on the thermoeconomic equations is strongly influenced by the outlet temperature of the cooling water to the cooling tower. The lower the temperature is required, the higher the cost of the cooling tower investment. In contrast to the centrifugal chiller and boiler investment cost calculations, the cooling tower investment costs based on thermoeconomic calculations can be reduced by lowering the cooling water outlet temperature. This can be done by increasing the mass flow rate of cooling water to the condenser.

Table 4.3. Total investment cost of the ORC unit

Component	**Cost (USD)**	
	R123	R245fa
ORC unit	159,072.097	143,164.88
Boiler	140,000	140,000
Cooling tower (PEC_{CT})	342,719.03	174,988.26
Feed pump (PEC_{FP})	2480.83	2387
HTF pump (PEC_{HTFP})	871.03	790.60
Cooling tower pump (PEC_{CTP})	912.74	1004.68
Total cost	**646,055**	**462,336**
USD/kWe	**3230.28**	**2311.68**

The LHV value per kilogram of Napier grass biomass is 16,779 kJ/kg (see Table 3.10). According to Mohammed et al. (2015), in the best conditions, Napier grass can be harvested four times a year with an average yield of 8.75 dry tons per hectare. Assuming that the availability factor ORC power plants per year is 0.85, the demand for Napier grass biomass for ORC power plants with different working fluid (R123, R245fa) for one year of operation can be seen in Table 4.4.

Table 4.4. Biomass fuel demand based on working fluid difference

Working fluid	Q_{bio} **(kW)**	$\dot{m}_{bio}$ **(kg/s)**	$\dot{m}_{bio}$ **(ton/day)**	$\dot{m}_{bio}$ **(ton/yr)**	**Land area (ha)**
R123	4213.07	0.25	21.69	7918	226.24
R245fa	4547.9	0.27	23.41	8547	244.22

From the calculations that have been carried out related to performance, component investment costs, and biomass requirements for ORC power plants based on the working fluid (R123, R245fa), it can be seen that there is no one type of working fluid that is genuinely superior to be selected as a single fluid job. Each fluid has its advantages and disadvantages. In terms of ORC efficiency, it can be seen that the working fluid R123 has the highest value of 7.04%, followed by R245fa (6.62%). R123 requires the slightest heat, 3581.11 kW, followed by R245fa (3865.75 kW) for the amount of heat input in the working fluid evaporator. This is directly related to the amount of biomass the ORC plant needs and, finally, the area of land required for planting the Napier grass biomass.

Since the initial objective of this research was to find an ORC power plant with a competitive investment cost compared to other types of power plants, the working fluid R245fa was chosen to be the working fluid for the ORC power plant with a component investment cost of 2311.68

USD/kW. The need for a land area for planting the Napier grass biomass of 244.22 ha with 21.69 ton/day can be overcome by using unproductive lands such as critical land and abandoned mines. According to Mohammed et al., (2015), Napier grass can be planted to fill vacant land in oil palm plantations, estimated to be 26.63% of the total land. Meanwhile, according to Warmanti, (2012), Napier grass can be cultivated on sandy land along the coast by using the correct dose of NPK fertilizer.

4.3.2. 4E analysis of existing biomass-ORC with capacity of 150 kWe

The biomass-ORC power-plant, located in Bologna, Italy, has a production capacity of 150 kWe and utilizes R134a as its working fluid. Energy generation in the plant is driven by wood waste combustion, achieving temperatures of 160-180°C and pressures of 11-12 bar. For this study, detailed calculations, as outlined in Sub-chapter 3.4.2, were performed using a combination of analytical tools.

After each component has been correctly modelled and merged into a unified system capable of iteration, the analysis tool's final schematic diagram is generated. The cooling tower and condenser's condition determines whether or not the two pieces of equipment can operate correctly. Once the biomass-ORC system model is operational, check the data from the modelling findings and the system's actual operating circumstances, as stated in Table 4.5. The modelling settings show a significant variance in pump power and regenerator temperature, with 1-2% differences, respectively. There is quite a large difference in pump power and condenser evaporator, around 4% differences error, respectively. This is because several parameters are not known in actual conditions, such as the properties of moist air, the size of the air condenser and regenerator sizing, which can affect the temperature of the working fluid that enters the pump and that will be heated in the regenerator.

Table 4.5. Comparing result of actual condition vs Unisim

Parameter	Unit	Actual	Unisim	Error (%)
P_{cond}	MPa	0.43	0.45	4.44
$T_{cooling}$	°C	5.1	5.1	0
T_{reg}	°C	73.6	74.54	1.28
P_{evap}	MPa	1.84	1.87	1.09
T_{exp}	°C	153	155	1.31
$\dot{W}_{exp}$	kW	85	85.3	0.35
$\dot{W}_{pump}$	kW	4.8	3	4.25

Fig. 4.24 is a profile of the heat exchanger (regenerator and evaporator) used in the biomass-ORC plant in Bologna. It can be seen in Fig. 4.24a, where the regenerator plays a role in the initial heating due to heat transfer flow from the expansion of the expander (green line) so that the working fluid from the pump (yellow line) can be heated until the temperature increases ~50 °C with the heat of 220 kW so that the condenser load to cool the working fluid is not excessive. Next, Fig. 4.24b shows the heat transfer from the biomass stream (green line) and working fluid (yellow line) in the evaporator, where the working fluid from the regenerator can be heated to 155 °C with a heat supply of 620 kW. So that the temperature and heat possessed by the working fluid are sufficient to rotate the expander and produce electricity.

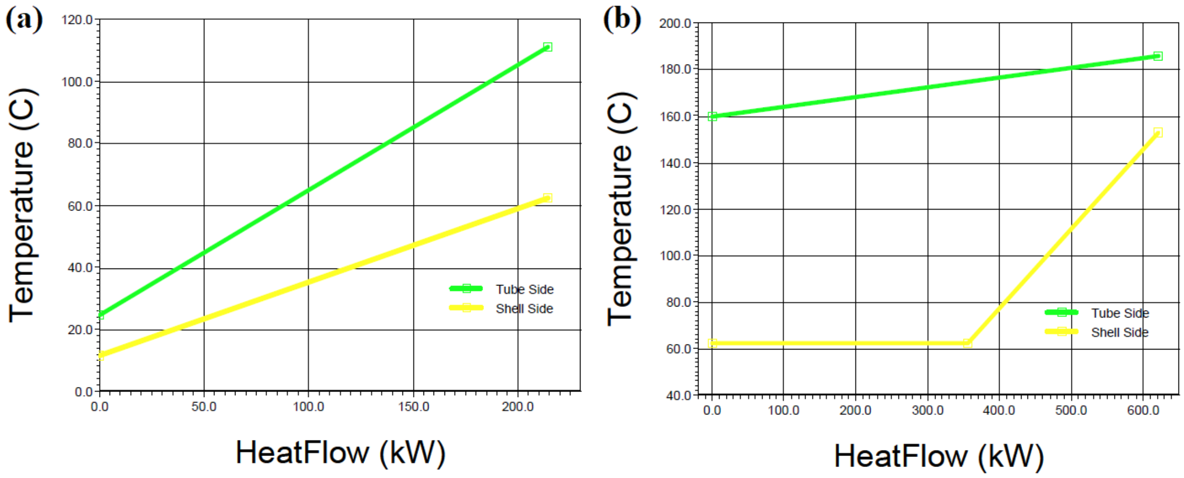

Fig. 4.24. Heat profile in biomass-ORC component: a) regenerator, b) evaporator

Fig. 4.25 shows the performance of the expander power output ($\dot{W}_{exp}$) against increasing temperature (T_{evap}) with different variables (mass flow rate ($\dot{m}$), isentropic efficiency (η_{iso}), and evaporator pressure (P_{evap})). Fig. 4.25a shows the difference in mass flow rate (1-5 kg/s) and temperature rise (145-155 °C) on the size of the $\dot{W}_{exp}$. The isentropic efficiency increase in components results in minor losses produced by the components, so energy conversion is optimal. Using the isentropic efficiency assumption of 0.9 results in an expander size of 70.43 kW in the same temperature range. On the other hand, Fig. 4.25c shows the difference in evaporator pressure (1.72-1.87 MPa) as the resulting $\dot{W}_{exp}$ increases, where the smallest evaporator pressure value (1.72 MPa) produces the largest $\dot{W}_{exp}$ (87.1 kW) in the same temperature range. This is because the power required by the pump is smaller (3.23 kW), and the heat produced by the evaporator is more optimal (225.5 kWh) to produce greater enthalpy for use by the expander in the same temperature range.

Similar results are shown in Fig. 4.26, where there is an increase in temperature on the thermal efficiency of biomass-ORC. In Fig. 4.26a, changes in mass flow rate (1-5 kg/s) do not significantly affect efficiency because the difference in net power is only affected by the increase in temperature. This differs from isentropic efficiency, where the difference between $\dot{W}_{exp}$ and evaporator heat is greatly influenced by isentropic efficiency. So, the highest η_{iso} value (0.9) produces the highest thermal efficiency (37.4%) at the same temperature. The thermal efficiency results in Fig. 4.26c produce the same trend as Fig. 4.25, where the lowest evaporator pressure (1.72 MPa) produces the highest thermal efficiency with a value of 37.2%.

In the analysis results in Fig. 4.25a and Fig. 4.26a, increasing the mass flow rate only has a significant effect on expander power but tends to stagnate on the efficiency of the ORC system. This was experienced by research by Soltani et al., (2015), where increasing the mass flow rate typically enhances all extensive outputs, which is expected as a result of increased power generation. While, varying the fuel mass flow rate has no effect on system's efficiency (since only capacity increases). Meanwhile, research by Karellas and Braimakis, (2016) confirms the results of the increase in expander power and system efficiency as the expander inlet temperature increases (Fig. 4.25c and Fig. 4.26c). It shows that lower pressure at high temperatures produces the highest expander power in biomass-ORC generation.

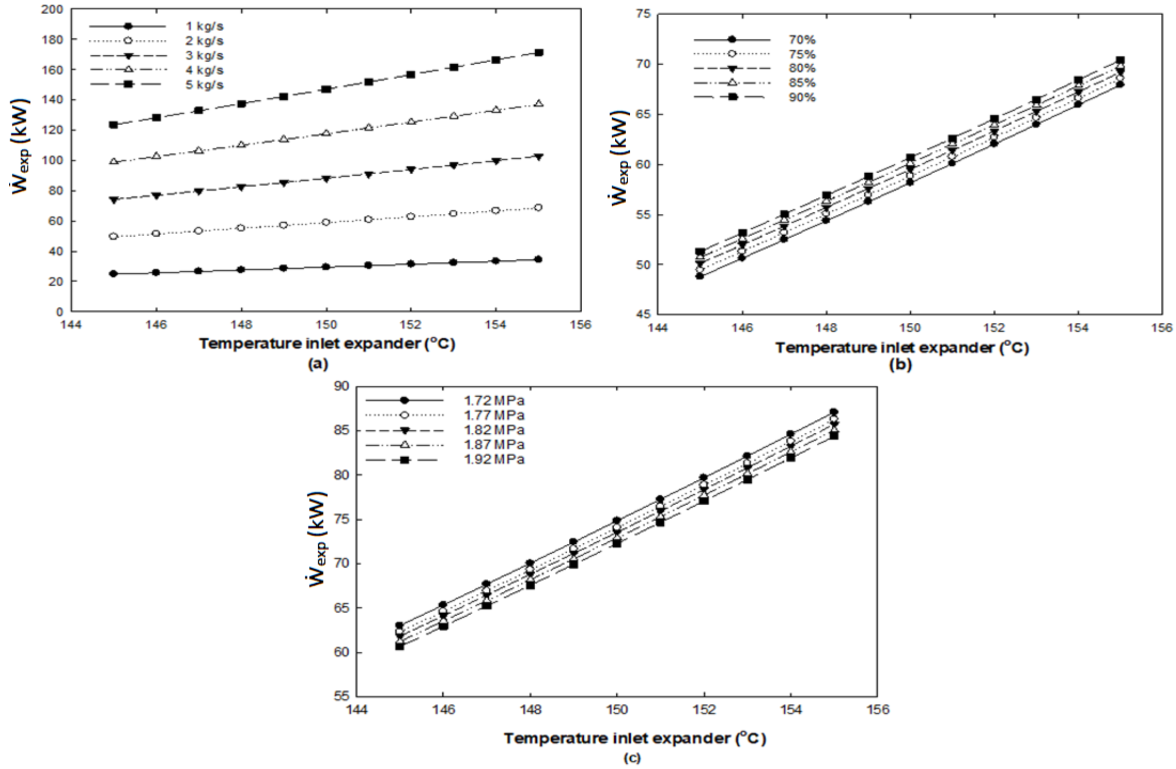

Fig. 4.25. The performance of $\dot{W}_{exp}$ vs T_{in} in different variable: a) $\dot{m}$, b) η_{iso}, c) P_{evap}

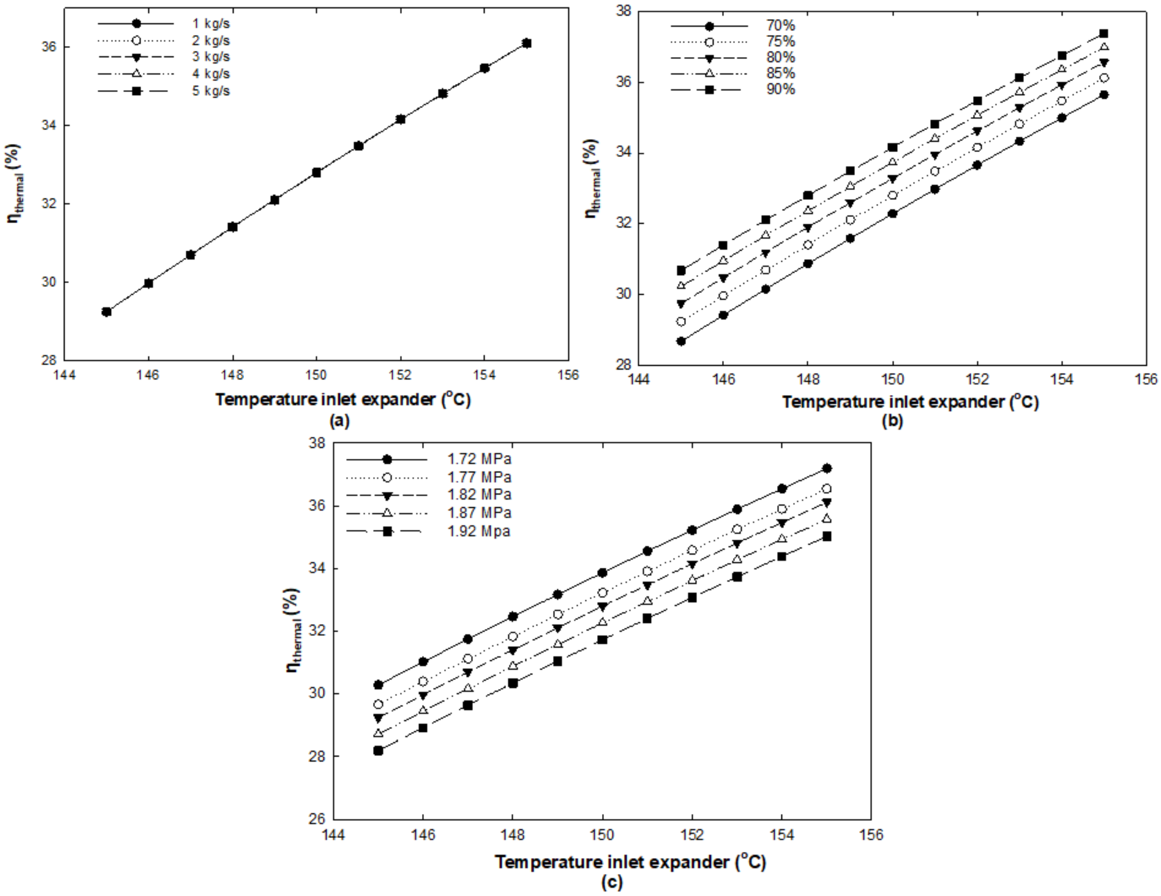

Fig. 4.26. The performance of $\eta_{thermal}$ vs T_{in} in different variable: a) $\dot{m}$, b) η_{iso}, c) P_{evap}

Fig. 4.27a shows the decrease in destruction exergy and system exergy efficiency as the expander inlet temperature increases, where the highest temperature (155 °C) produces the lowest destruction exergy and efficiency exergy with amounts of 71.54 kW and 8.9%, respectively. Meanwhile, the highest exergy damage experienced by each component is the evaporator, and the lowest is the pump, with values of 24.76 and 1.2 kW, respectively as shown in Fig. 4.27b. The evaporator is also the most significant exergy-contributing component compared to other components, around 33.84%, which can be seen in Fig. 4.27c. This is very natural because the evaporator is the component where heat exchange between the biomass heat source and the working fluid occurs, and an increase in entropy due to non-optimal heat conversion often occurs. In some literature, the exergy destruction value of the evaporator is very high, but this is minimized by a regenerator, which utilizes the heat from the expansion in the expander so that it is not directly cooled by the condenser so that the cooling load can be reduced.

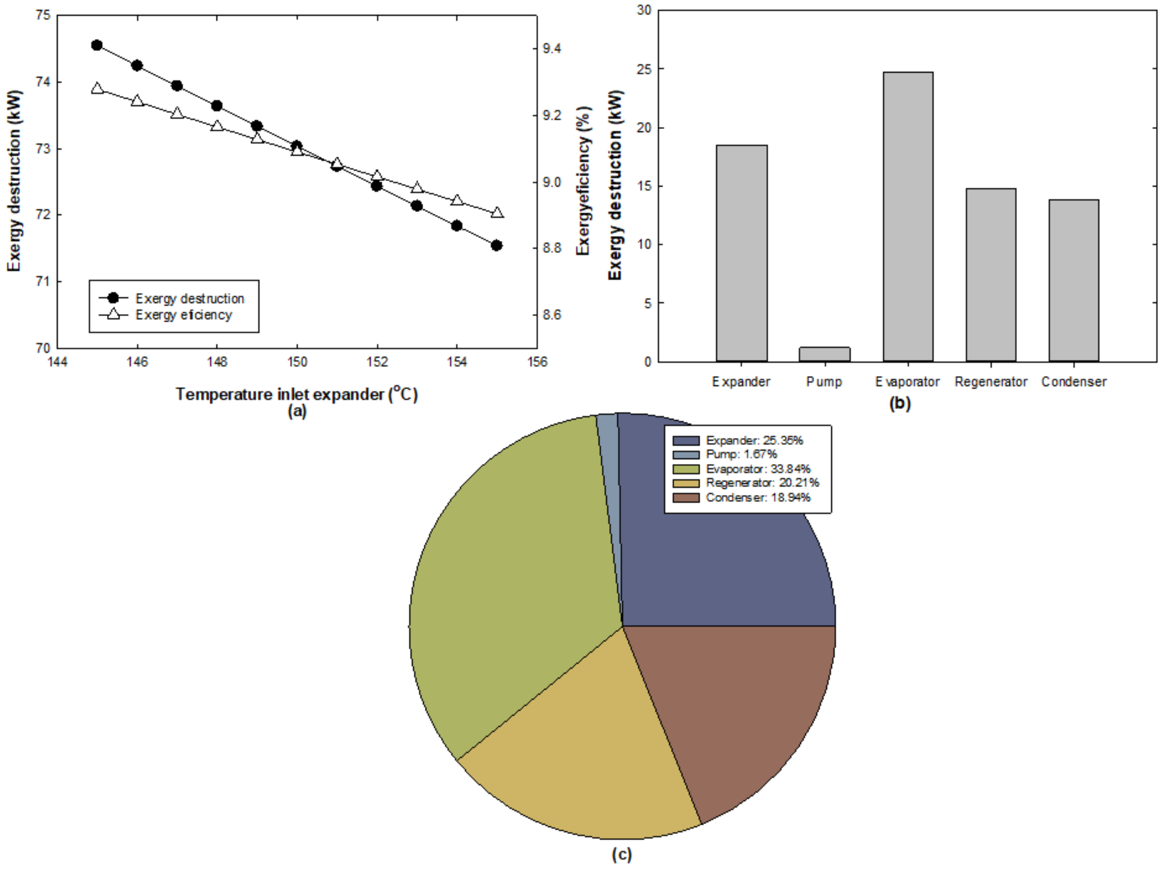

Fig. 4.27. Exergy performance of biomass-ORC: a) temperature inlet expander, b) component's exergy destruction, c) exergy efficiency of each component

Fig. 4.28 depicts the exergy sustainability of each working fluid, as indicated by numerical parameters such as exergy waste ratio (EWR), environmental effect factor (EEF), and exergy sustainability index (ESI), as well as two benchmarks for comparison. EWR is the ratio of overall waste exergy to overall input exergy, and according to the computation, practically all working fluids have almost the same EWR value, ranging from 0.25 to 0.85, with R134a having the highest EWR value of 0.843 and R143a having the lowest EWR value of 0.27 (Permana et al., 2021). The EWR value is relatively minor in comparison to the studies done by (Aydin,

2013) on the turbine component and (Abam et al., 2018) with the working fluid R245fa, which generate EWR values of 0.65 and 0.75, respectively.

Another indicator is the environmental effect factor, it may indicate the system's environmental harm caused by waste exergy destruction (Abam et al., 2018). Fig. 4.28 displays the EEF values of each working fluid, with Propane having the highest EEF value of R143a (Permana et al., 2021)., followed by R245fa (Abam et al., 2018), R134a with EEF values of 1.98, 1.83, and 1.02, respectively. R134a, on the other hand, had the lowest EEF value among working fluids and was regarded as more sustainable. The R134a had a lower environmental impact than other working fluids. As the last review, ESI is a degree of sustainability that serves as a supplement to the EEF (Aydin, 2013). Fig. 4.28 shows that R134a had the highest ESI value of 0.98. These values are relatively minor compared to (Aydin, 2013) and (Abam et al., 2018), who had ESI values of 0.651 and 0.491, respectively.

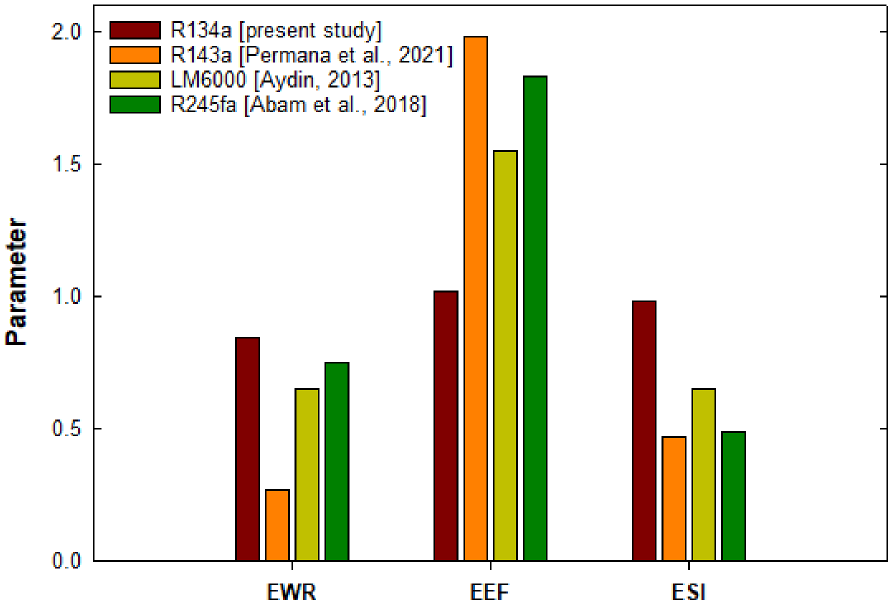

Fig. 4.28. Exergy sustainability index

This section discusses the crucial findings from the case study system's economic analysis. Table 4.6 shows investment costs for the system's components. The total investment cost (C_{TCI}) is the sum of the individual system's components.

Meanwhile, Table 4.7 shows the annual economic analysis of the system including SIC, NPV, SPP, and LCOE. Moreover, in Table 4.7 presents several differences between the annual biomass-ORC economic calculations. This can be based on making different assumptions regarding component prices, net electricity selling prices, biomass prices, and annual energy usage hours.

Table 4.6 Component cost

Components	Investment cost (×10^3)
Boiler (€)	1,684
Expander (€)	135
Pump (€)	9.2
Evaporator (€)	18.9
Regenerator (€)	24.6
Air-cooled condenser (€)	40.4
Working fluid (€)	75
O&M (€)	38.2
C_e (€/year)	28.5
C_h (€/year)	169.4
C_{bio} (€/year)	75
C_{ncf} (€)	84.4

Table 4.7. Annual economic biomass-ORC plant

Parameter	Present value	Value (Braimakis et al., 2021)
C_{TCI} (×10^3 €)	2025	1224
SIC_{Plant} (×10^3 €/kWe)	13.5	13.9
SIC_{ORC} (×10^3 €/kWe)	2.3	2.4
NPV (×10^3 €)	238	259
SPB (years)	24	20
LCOE (€/kW.h)	0.93	0.91

Meanwhile, C_{CTI} and C_{nf} are obtained from Eqs. (3.68) and (3.76) with the assumption that the average selling price of heating and electricity for the last three years is around 80-100 €/MWh and with biomass consumption of 1500 tons/year and assuming residential use of up to 2000 hr/year. So from these parameters, we get SIC, NPV and LCOE of 13.5×10^3 €/kWe, 238 ×10^3 €/year and 0.93 €/kW.h, respectively. This mean that investment in ORC with biomass is quite significant compared to conventional nuclear and coal fuel plants. Moreover, from the calculation results, SPB from biomass-ORC investment can be achieved in 26-27 years, assuming constant inflation. If we look at similar research conducted by (Braimakis et al., 2021) using cyclopentane working fluid, this simulation produces power and efficiency of around 88 kWe and 8.1%, respectively.

4.4. Experimental study of ORC

4.4.1. Performance evaluation of ORC 2 kW test rig

The tests conduct involved a procedure repeated throughout the test campaign. The maximum temperature conditions of the source were imposed higher, and some operating parameters of the thermodynamic cycle have been changed (such as the rotation frequency of the circuit feed pump and the load resistive applied to the expander) to verify its behaviour and identify performance. First, the steam generator, which represents the source, is activated by the temperature of the thermodynamic cycle. Once the test temperature conditions have been reached, the dissipation circuit pumps are activated, and only then is the ORC pump. During the test, the temperatures of the sources are kept constant. For a given value of the pump rotation speed, the resistive electrical load is varied to investigate the behaviour of the system for different rotation speeds of the expander and mass flow rate. The data obtained from the experiment was recorded via LabView acquisition for around 3 hours and 30 minutes. Finally, the ORC prototype system operated stagnantly and produced power on changes in the required parameters. Next, the data is processed using statistical methods and reduced to an average of every 5 minutes to facilitate the description of the characteristics of the prototype system created.

Fig. 4.29 depicts the experimental performance analysis of an ORC system with a nominal power generation capacity of 2 kW. It uses two detailed subplots to explore how system behaviour varies under different operational conditions, specifically focusing on the relationship between mass flow rate (ṁ) and the expander inlet pressure (P_1), while analysing the power output ($\dot{W}_{exp}$) and thermal efficiency ($\eta_{thermal}$).

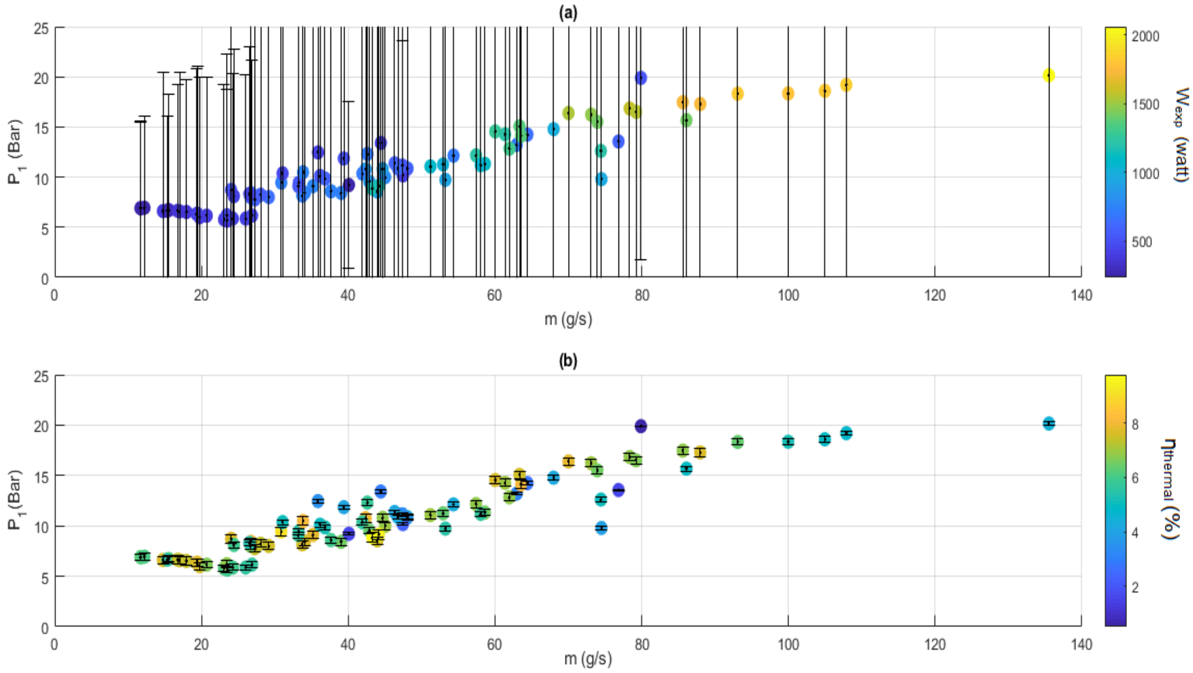

Fig. 4.29. Parametric analysis of $\dot{m}$ vs P_1: a) $\dot{W}_{exp}$, b) $\eta_{thermal}$

In Fig. 4.29a, the performance metric under consideration is the power output from the expander, $\dot{W}_{exp}$, measured in Watts. Here, the $\dot{m}$ ranges from 0 to 140 g/s, reflecting varying input conditions for the working fluid within the system. The y-axis shows the P_1, which ranges from approximately 5 to 25 bar, representing the pressures achieved under different operating regimes. Each data point is color-coded to represent the corresponding power output, with a colourmap on the right indicating values from 500 W (deep blue) to 2000 W (bright yellow). Most of the markers are concentrated at lower $\dot{m}$, illustrating the conditions under which the system generates power. A gradient from blue to yellow can be observed, demonstrating an increase in power generation as both $\dot{m}$ and P_1 rise. Vertical error bars accompany each marker, highlighting the variability or uncertainty in the recorded pressure values, which is a common characteristic in experimental setups. This visualization underscores the system's ability to reach its nominal power output of 2 kW, particularly at higher mass flow rates and pressures. It provides critical insight into the operating window where the system is most effective.

Fig. 4.29b shifts the focus to the thermal efficiency ($\eta_{thermal}$) of the system, expressed as a percentage. Once again, the x-axis spans the mass flow rate ($\dot{m}$), while the y-axis indicates the evaporator inlet pressure (P_1). Here, the data points are similarly color-coded, but this time to represent thermal efficiency, as shown by the colourmap ranging from 2% (dark blue) to 8% (bright yellow). This subplot highlights the efficiency trends under varying operational conditions. A positive correlation is evident, with higher $\eta_{thermal}$ achieved at greater $\dot{m}$ and elevated pressures. Interestingly, horizontal and vertical error bars surround each data point, emphasizing the variability in both $\dot{m}$ and P_1. These error bars are essential for understanding the uncertainties inherent in experimental setups. The efficiency values peak at around 8%, showcasing the system's ability to convert thermal energy into useful work with reasonable effectiveness under optimized conditions. In practical terms, the increasing $\dot{W}_{exp}$ and $\eta_{thermal}$ with higher $\dot{m}$ and P_1 align with thermodynamic expectations. Higher pressures improve the expansion process in the turbine or expander, leading to better power extraction. Similarly, the mass flow rate impacts the heat transfer in the evaporator and condenser, directly influencing both $\dot{W}_{exp}$ and $\eta_{thermal}$.

Fig. 4.30 is focusing on the relationship between the $\dot{m}$ and the T_2, while examining the same performance metrics: $\dot{W}_{exp}$ and $\eta_{thermal}$. This figure mirrors the layout of the first, with two subplots arranged vertically, emphasizing how outlet temperature influences the performance of the ORC system under varying $\dot{m}$.

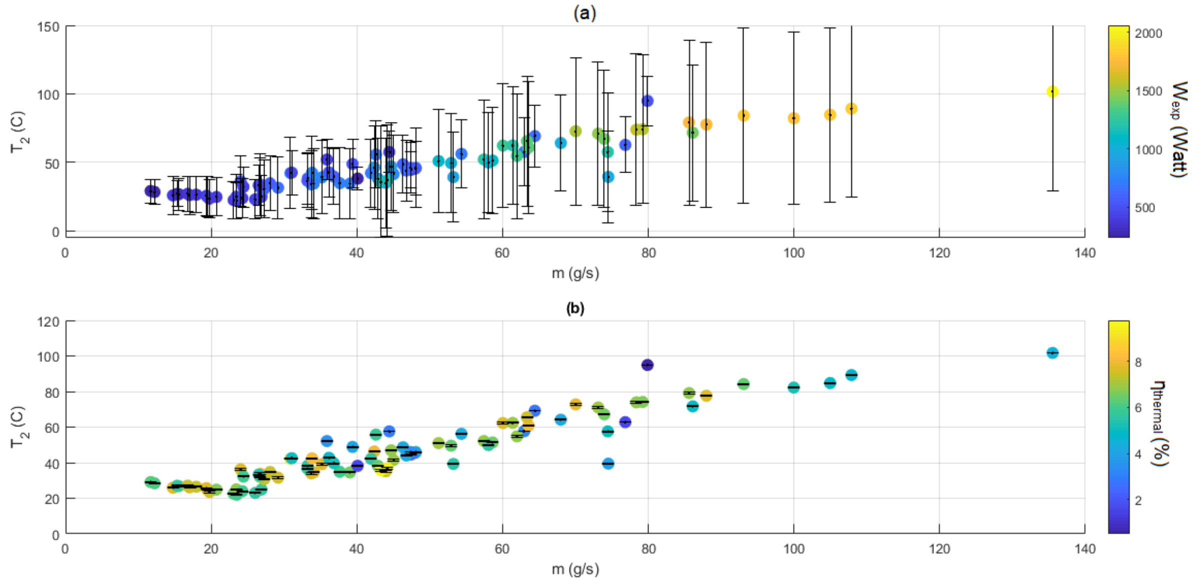

Fig. 4.30. Parametric analysis of $\dot{m}$ vs T_2: a) $\dot{W}_{exp}$, b) $\eta_{thermal}$

The same phenomenon is shown in Fig. 4.30, where producing the highest $\dot{W}_{exp}$ involves one or two of the highest input variables; in Fig. 4.30a, it can be seen that the largest $\dot{W}_{exp}$ (2000 Watt) is at the expander outlet temperature T_2 (102 °C) and the highest $\dot{m}$ (135 g/s). The data points are color-coded to reflect $\dot{W}_{exp}$, with the accompanying colour scale to the right ranging from 500 Watt (dark blue) to 2000 Watt (yellow). Most data points are concentrated at lower temperatures and flow rates, but a clear positive trend is visible: as the flow rate increases, the outlet temperature also rises, accompanied by an increase in $\dot{W}_{exp}$. Vertical black error bars extend from each data point, reflecting uncertainties or variations in the recorded outlet temperature values. This variability becomes more pronounced at higher flow rates, suggesting that the system's thermal dynamics become more complex at elevated operating conditions.

The data demonstrates that the ORC system achieves its designed 2 kW capacity at higher T_2 and $\dot{m}$, further illustrating the relationship between expander performance and heat recovery efficiency. Here in Fig. 4.31b, the colour coding represents thermal efficiency, as indicated by the colour scale ranging from 2% (dark blue) to 8% (yellow). The data points reveal a consistent trend where $\eta_{thermal}$ increases with both ṁ and T_2. Horizontal and vertical error bars encircle each data point, reflecting measurement uncertainties in both $\dot{m}$ and T_2. Notably, higher efficiencies (above 6%) are achieved at T_2 exceeding 80 °C and ṁ around 100 g/s or higher. This visualization emphasizes the importance of the turbine outlet temperature as a critical parameter for maximizing the $\eta_{thermal}$. At higher T_2, the ORC system effectively utilizes the available heat energy, resulting in better energy conversion and closer alignment with the theoretical Carnot efficiency.

The two sets of figures (Fig. 4.31 and Fig. 4.32) provide a comprehensive visualization of the thermodynamic behaviour of an ORC experimental setup. They investigate the influence of N_{pump} and corresponding operational parameters such as $\dot{m}$, $\dot{W}_{exp}$, $\eta_{thermal}$, and T_2 and P_1. Both figures offer insights into the system's behaviour at various operating conditions, with error bars representing uncertainty in measurements.

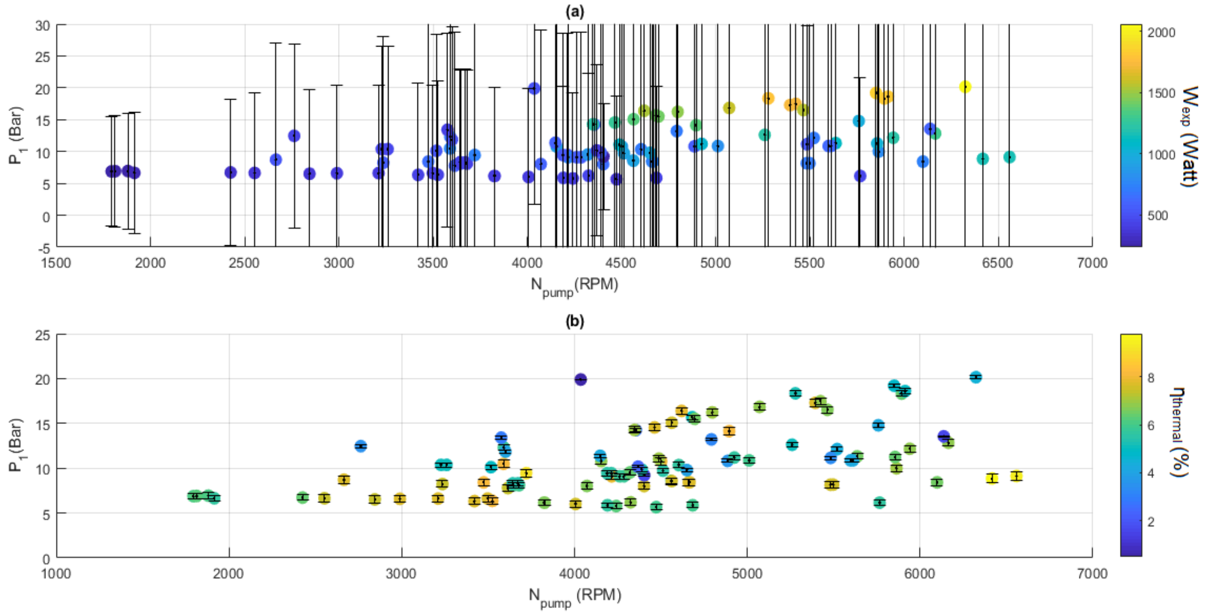

Fig. 4.31. Parametric analysis of N_{pump} vs P_1: (a) $\dot{W}_{exp}$, (b) $\eta_{thermal}$

In Fig. 4.31a, the trend indicates that increasing N_{pump} generally raises P_1, which is consistent with increased fluid compression due to higher pump performance. However, as P_1 rises, the black error bars demonstrate increasing measurement uncertainty, particularly at higher rotational speeds. Data points with warmer colours (yellow-orange) signify higher $\dot{W}_{exp}$ values (close to 2000 W), which is aligned with the design goal of a 2 kW capacity ORC system. These points are concentrated around intermediate N_{pump} values (4000-6000 RPM), where the system appears to operate most efficiently. Meanwhile, Fig. 4.31b depicts P_1 is plotted against

N_{pump}, with the colorbred showing $\eta_{thermal}$. The $\eta_{thermal}$ increases with pump speed but plateaus at higher RPMs, likely due to diminishing returns as pressure ratios and fluid losses stabilize. The data points with the highest efficiency (~8%) occur near the optimal operational region (5000–6000 RPM), indicating a sweet spot for balancing compression work, flow rate, and heat transfer effectiveness.

In Fig. 4.32a, the scatter plot maps the evaporator outlet temperature against N_{pump}, with $\dot{W}_{exp}$ represented through the colour gradient. At lower RPMs (below 3000 RPM), T_2 values remain modest, constrained by limited fluid compression. As N_{pump} increases, T_2 rises non-linearly, indicating higher heat absorption by the working fluid. Points with higher $\dot{W}_{exp}$ values (yellow-coloured markers) align with higher T_2 values, reinforcing the role of optimal thermal energy input in achieving high expansion power. Measurement uncertainties (error bars) expand significantly at high RPMs, underscoring experimental challenges in capturing dynamic behaviour during elevated heat transfer rates. Fig. 4.32b demonstrates the relationship between T_2 and N_{pump}, with $\eta_{thermal}$ as the colour scale. The thermal efficiency peaks in the mid-range RPM region (3500-5000 RPM) and then declines, even as T_2 continues to rise. This trend indicates inefficiencies due to overheating or losses in fluid dynamics and heat exchanger performance.

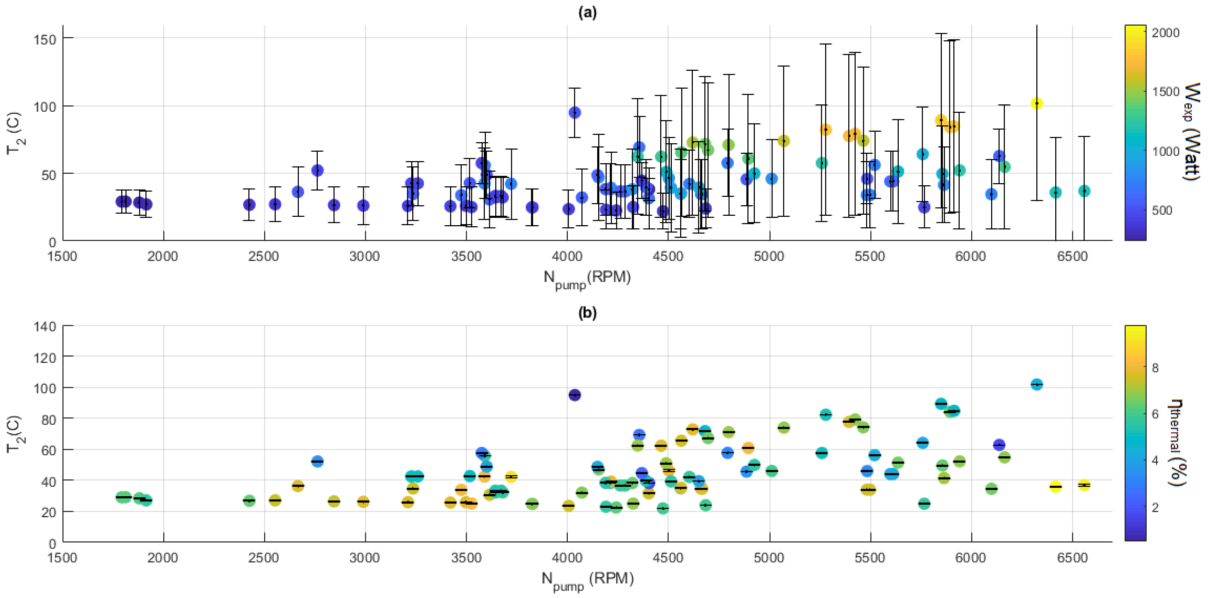

Fig. 4.32. Parametric analysis of N_{pump} vs T_2: (a) $\dot{W}_{exp}$, (b) $\eta_{thermal}$

The optimal operating region appears to lie within 4000-6000 RPM, where both $\dot{W}_{exp}$ and $\eta_{thermal}$ reach their maximum practical values. Beyond this range, diminishing returns set in due to physical constraints such as fluid cavitation, heat exchanger limitations, and increased entropy generation. The prominent error bars at extreme operating conditions highlight experimental challenges, including sensor precision, transient thermal behaviour, and flow instability. These visualizations provide valuable feedback for scaling ORC systems, particularly for real-world applications like waste heat recovery, where dynamic load profiles demand robust and adaptive control of N_{pump} and other parameters. In conclusion, these figures provide a detailed lens into the performance characteristics of a 2 kW ORC system, revealing the delicate balance between mechanical inputs, thermodynamic outputs, and real-world uncertainties.

4.4.2. Prediction analysis and optimisation of experimental ORC using ANN

Additional experimental tests were conducted on a 2 kW ORC prototype. To enhance efficiency and minimize resource consumption, an ANN was employed to predict unmeasured or unknown experimental data. As a result, an ANN-ORC model was developed and validated using 102 sets of experimental data, enabling the optimization of system performance and operational parameters. The study includes a comprehensive parametric analysis and explores multi-objective optimization to maximize both output work and thermal efficiency. Based on the operating parameters, data, and equations detailed in Subchapter 3.5.2, the findings are discussed as follows.

The gradient and the number of validation checks are used to finalize the network training. The training process concludes after 12 epochs, with the best validation performance achieved after 6 epochs, as illustrated in Fig. 4.33a. Fig.4.33b presents the performance graphs for the training process, including the gradient, learning rate (μ), and validation checks. The validation failure curve indicates that the model could not achieve a lower mean squared error (MSE) after 12 epochs demonstrating a steady, resulting in the training being halted decrease in error and proper stopping criteria, which avoids over fitting.

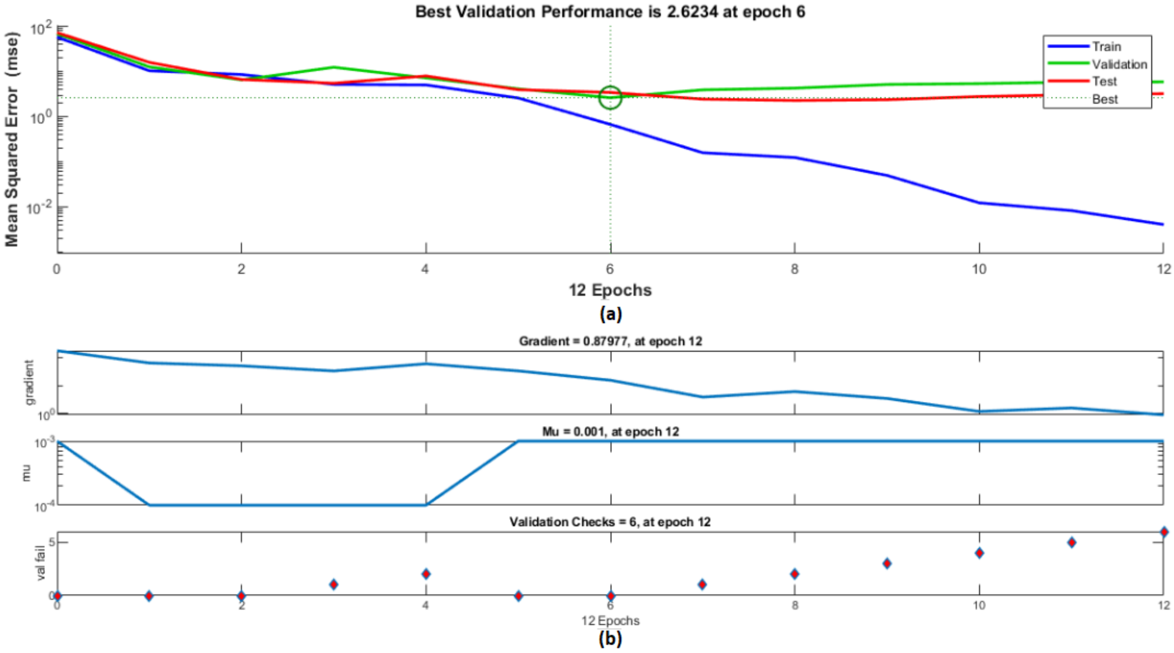

(a)

(b)

Fig. 4.33 Model performance operation: a) validation, b) epoch

The projected $\dot{W}_{exp}$ and $\eta_{thermal}$ results are directly comparable to the experimental data and fitting with slope and intercept of 0.9877 and 17.473 for $\dot{W}_{exp}$ (Fig. 4.34a) indicating high prediction accuracy, while the slope and intercept for $\eta_{thermal}$ is 0.900 and 0.5549 (Fig. 4.34b) emphasizing that while the model is effective, there is some variability in efficiency predictions. Fig. 4.35 depicts the absolute and relative errors of the training samples acquired by the predicted and actual. Fig. 4.35a examines $\dot{W}_{exp}$, revealing fluctuations but predominantly low errors, validating the reliability of the model. Meanwhile, Fig. 4.35b assesses $\eta_{thermal}$, showing minimal absolute errors but slightly higher relative errors, reflecting variations in efficiency at lower magnitudes. The absolute inaccuracy for W_{exp} and $\eta_{thermal}$ is 0-700 W and 0-3%, respectively. Most relative errors for $\dot{W}_{exp}$ and $\eta_{thermal}$ are within 0-50%, respectively. Only a few data points transcend these ranges. The difference is noticeable when comparing the expected performance map based on the colour contour in Figs 4.37-4.40, which indicates the expected performance map's tight alignment with the experimental data utilized for validation.

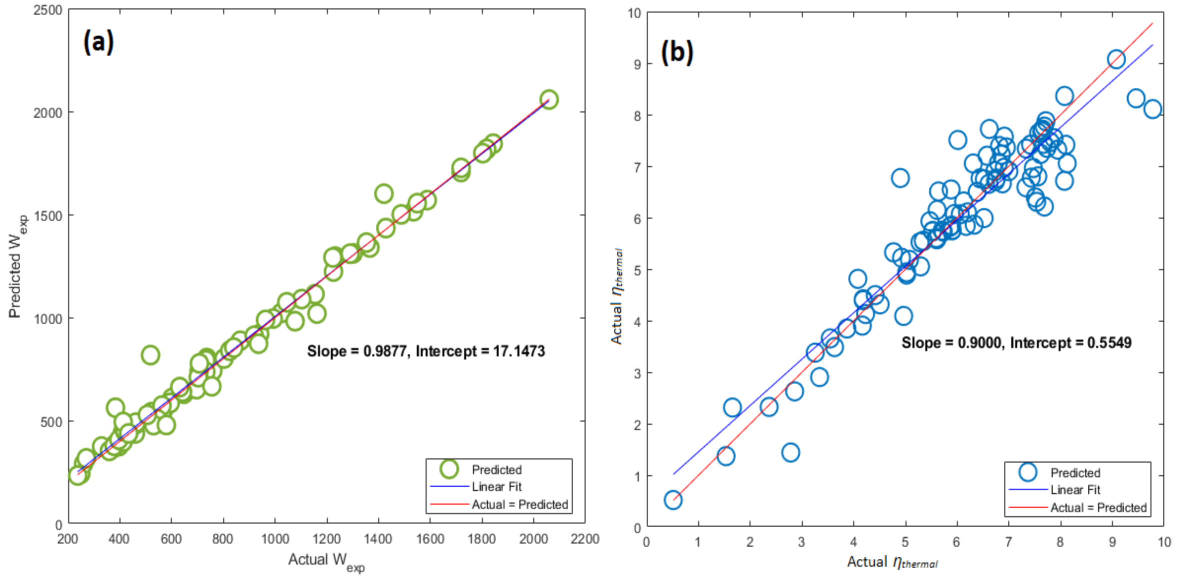

Fig. 4.34. Training result of predicted and actual: a) $\dot{W}_{exp}$, b) $\eta_{thermal}$

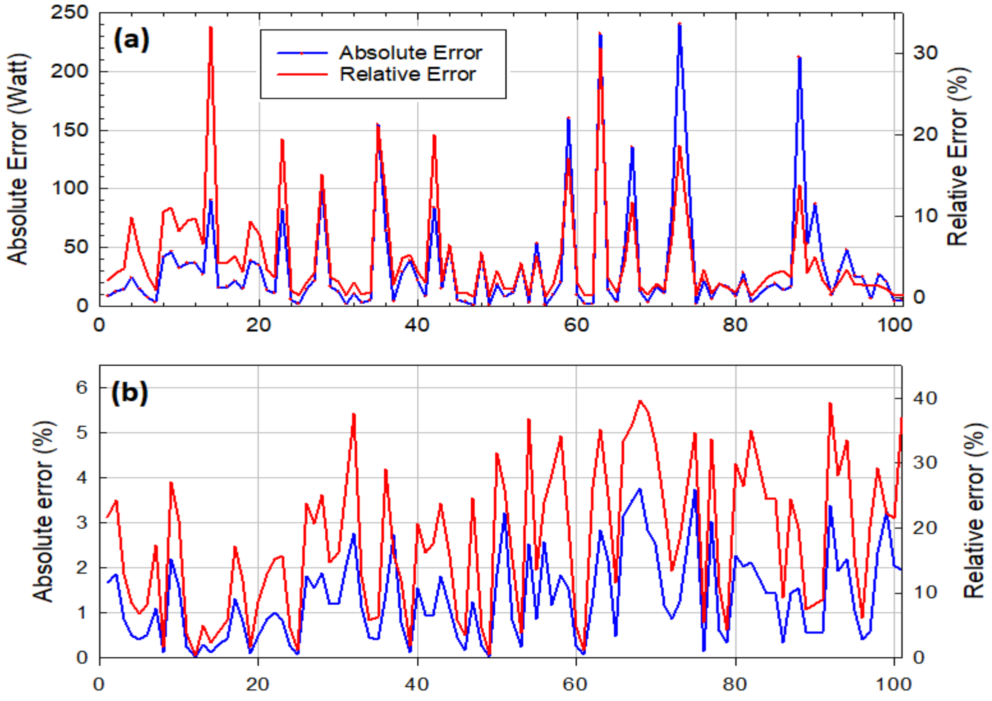

Fig. 4.35. Result of Absolute error and relative error: a) $\dot{W}_{exp}$, b) $\eta_{thermal}$

The predicted vs actual results involving two input variables that have the influence on the W_{exp} and $\eta_{thermal}$ results are shown in Fig. 4.36 - Fig. 4.39. The contour colour map of both images is the predicted result of the neural network analysis training data, where the colour dot shape is the actual data for $\dot{W}_{exp}$ and $\eta_{thermal}$, respectively. However, due to normal fit, the figures show that two specified ANN models generate essentially identical shapes. $\dot{W}_{exp}$ prediction contour results show that the larger the $\dot{m}$ and P_1, the greater the predicted $\dot{W}_{exp}$ and actual $\dot{W}_{exp}$ shown by Fig. 4.36a and Fig. 4.37a, and the maximum of actual W_{exp} is around 1600-2000 W at the similar range with predicted $\dot{W}_{exp}$ with input variables of $\dot{m}$ around (80-120 g/s) and P_1 (14-20 Bar) and T_2 (75-90 °C), respectively. On the other hand, in Fig. 4.36b and Fig. 4.37b, it can be seen that in both predicted and actual results, $\dot{m}$ has no significant effect on $\eta_{thermal}$. It's in line with the results of the parameter analysis carried out by Permana et al. (2023) in its solar-ORC study.

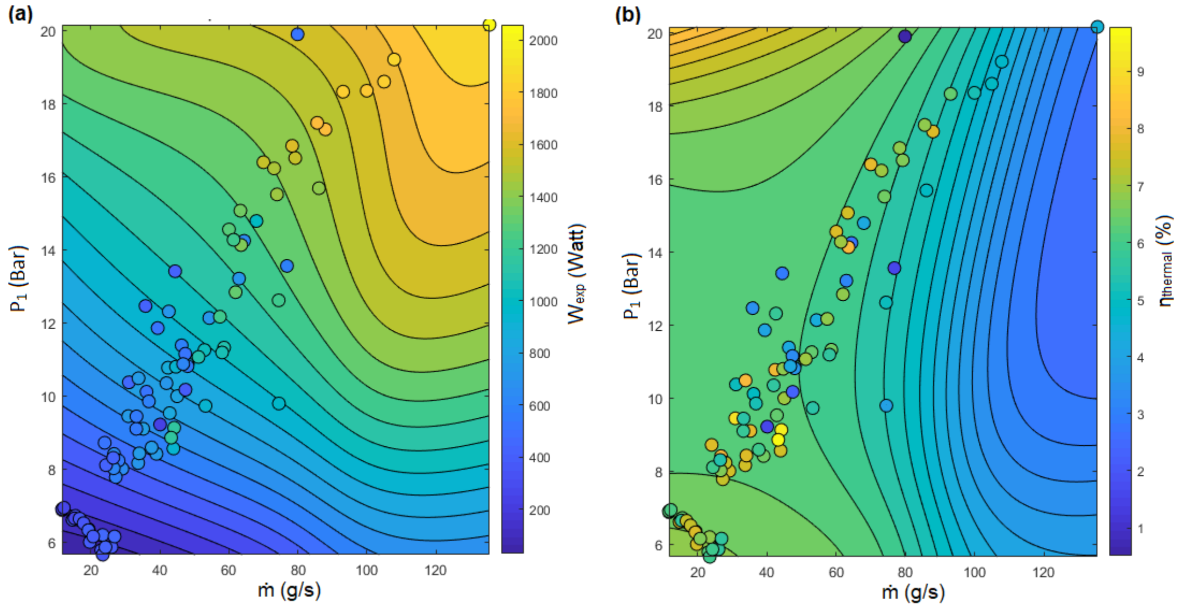

Fig. 4.36. The contour map of training result in different of $\dot{m}$ and P_1: a) $\dot{W}_{exp}$, b) $\eta_{thermal}$

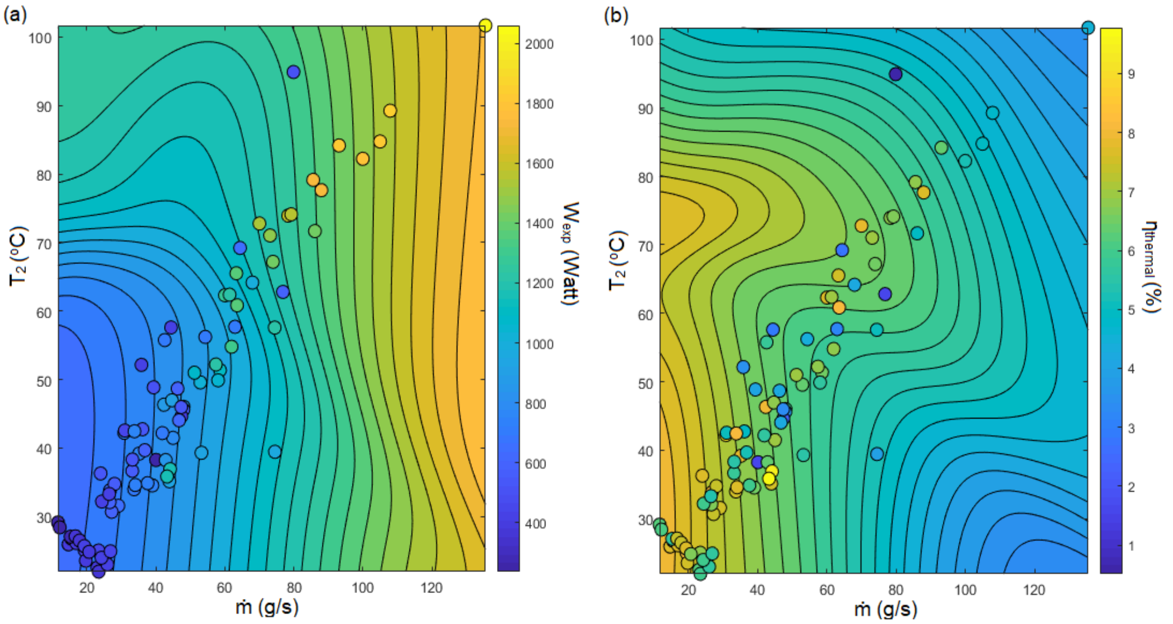

Fig. 4.37. The contour map of training result in different of $\dot{m}$ vs T_2: a) $\dot{W}_{exp}$, b) $\eta_{thermal}$

Fig. 4.38a Results of actual- $\dot{W}_{exp}$ vs predicted- $\dot{W}_{exp}$ of the two input variables (N_{pump} vs P_1) are in the same value range (1600-2000 Watt), namely in the N_{pump} and P_1 ranges of (5500-6500 RPM) and (17-20 Bar), respectively. In the same trend where in the N_{pump} range of 5500-6500 RPM, Fig. 4.39a shows the power produced by $\dot{W}_{exp}$ is large (1600-2000 Watt) but in the range of T_2 (75-100 °C) for both actual and predicted result. Fig. 4.38b shows efficiency results for actual and predicted results showing different tendencies. In the relationship between N_{pump} and P_1 is shown by Fig. 4.39, 8-10% efficiencies are spread over several N_{pump} distributions (2500-6500 RPM), but at large P_1, less than 18 bars. While in Fig. 4.39b, high predicted $\eta_{thermal}$ results can be seen at N_{pump} (5000-6500 RPM) and T_2 below 55 °C, in the same T_2 range; on the other hand, the actual $\eta_{thermal}$ results are at N_{pump} (2500-5000 rpm).

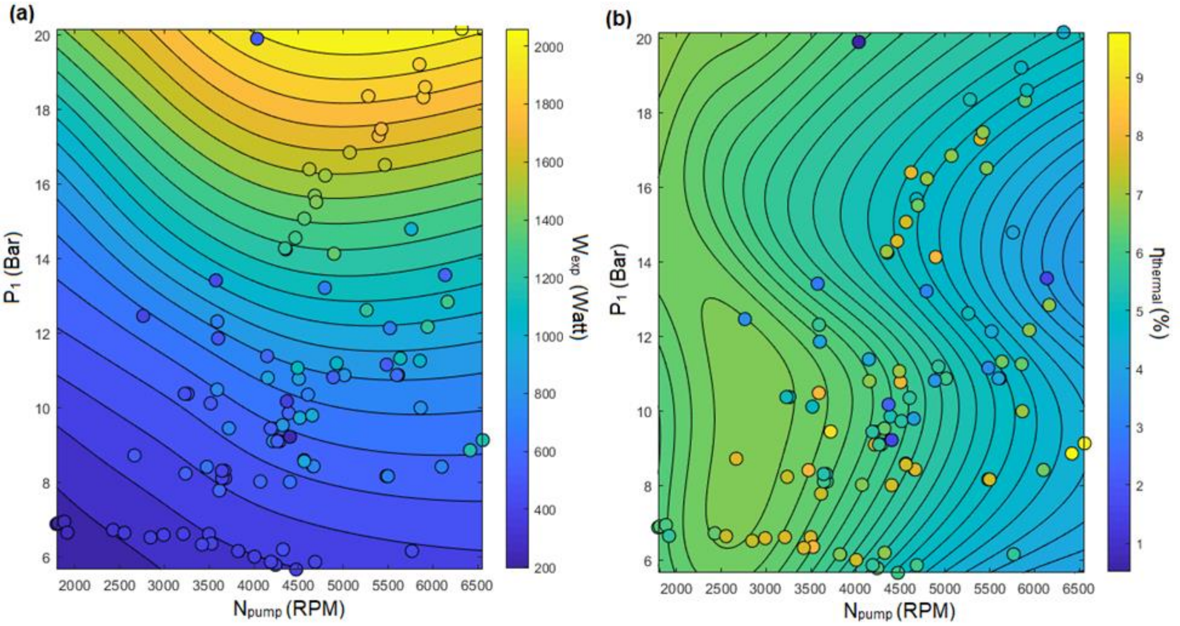

Fig. 4.38. The contour map of training result in different of N_{pump} vs P_1: a) $\dot{W}_{exp}$, b) $\eta_{thermal}$

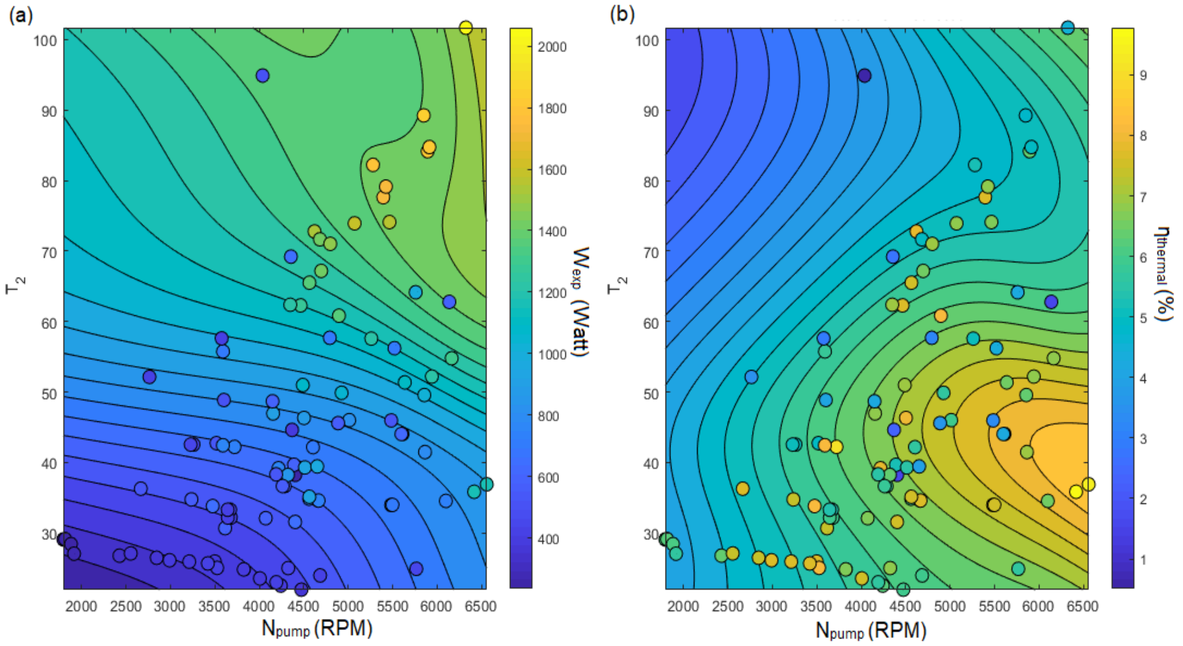

Fig. 4.39. The contour map of training result in different of N_{pump} vs T_2: a) $\dot{W}_{exp}$, b) $\eta_{thermal}$

The *R-values* provided in Table 4.8 reflect the correlation coefficients across training, validation, test, and combined datasets for all figures. These values indicate the performance and reliability of the prediction model in capturing the relationships between actual and predicted values for various cases. Fig. 4.36 demonstrates exceptionally high correlation values across all datasets, with the highest *R-value* of 0.9997 during training and a slightly lower value of 0.97875 for testing, resulting in a combined *R-value* of 0.99548. This figure reflects the model's robust ability to generalize with minimal deviation. Fig. 4.37 shows slightly reduced R-values compared to Fig. 4.36 but still maintains high accuracy, particularly in the combined dataset with an *R-value* of 0.99643. The consistency between validation (0.99606) and testing (0.98475) highlights the model's adaptability across datasets. Fig. 4.38 achieves the highest overall R-values, particularly for the validation (0.99805) and combined datasets (0.99824), indicating superior prediction reliability. This figure likely represents the most optimized case of the model. Fig. 4.39 has slightly lower *R-values* compared to the other figures, particularly for validation (0.98976) and testing (0.98765), with a combined *R-value* of 0.99371. While still highly accurate, this figure suggests more variation in the model's predictions.

Table 4.8. The R-value of each figure

Figures	**R-values**			
	Training	Validation	Test	All
Fig. 4.36	0.9997	0.99697	0.97875	0.99548
Fig. 4.37	0.99863	0.99606	0.98475	0.99643
Fig. 4.38	0.99924	0.99805	0.99522	0.99824
Fig. 4.39	0.99568	0.98976	0.98765	0.99371

These *R-values*, paired with the detailed insights from the figures, demonstrate the model's strength in predicting ORC performance. The Fig. 4.36, Fig. 4.37, and Fig. 4.38 highlight excellent predictive accuracy, with Fig. 4.38 emerging as the most significant in terms of overall reliability, whereas Fig. 4.39 suggests opportunities for further refinement in validation and testing phases.

As demonstrated in the previous section, the operational parameters significantly influence overall system performance. In engineering applications, $\dot{W}_{exp}$ and $\eta_{thermal}$ are key evaluation metrics. However, the maximum $\dot{W}_{exp}$ and maximum $\eta_{thermal}$ may occur at different times, as they respond differently to various operational factors. Therefore, a multi-objective optimization using an ANN model is carried out to simultaneously maximize $\dot{W}_{exp}$ and $\eta_{thermal}$, aiming to achieve the optimal system performance and operation settings. The operational parameters mentioned in the previous subsection are used as decision variables, while $\dot{W}_{exp}$ and $\eta_{thermal}$ are chosen as the multi-objective functions.

The data points in all figures above are correspond to experimental or calculated results, with colours matching the contour values, providing validation and insight into the system's behaviour. Together, these plots reveal the trade-offs in ORC optimization, where maximizing $\dot{W}_{exp}$ often comes at the expense of $\eta_{thermal}$, and achieving higher efficiency can limit power output. Such visualizations are crucial for designing ORC systems, helping to identify optimal operating conditions that balance power output and efficiency based on application-specific priorities:

Objectives:

$$\max \dot{W}_{exp} \;\; ; \max \eta_{thermal}$$

Constrain:

$$\dot{\mathrm{m}}_{min} \leq \dot{\mathrm{m}}_{wf} \leq \dot{\mathrm{m}}_{max}$$

$$T_{1\_min} \leq T_1 \leq T_{1\_max}$$

$$T_{2\_min} \leq T_2 \leq T_{2\_max}$$

$$P_{1\_min} \leq P_1 \leq P_{1\_max}$$

$$P_{2\_min} \leq P_2 \leq P_{2\_max}$$

$$T_{cond\_min} \leq T_{cond} \leq T_{cond\_max}$$

$$N_{pump\_min} \leq N_{pump} \leq N_{pump\_max}$$

Table 4.9 lists the ranges for the six operating parameters. Based on the energy balance, the following constraints must be satisfied.

Table 4.9. The lower-upper value of optimization variables

Optimization variables	**Lower (min)**	**Upper (max)**	**unit**
$\dot{m}$	11.7	135.5	g/s
T_1	132.42	166.39	°C
T_2	21.95	101.68	°C
P_1	5.65	20.15	Bar
P_2	1.44	10.03	Bar
T_{cond}	24.16	89.855	°C
N_{pump}	1793.6	6558.1	RPM

Fig. 4.40 shows two other optimized input variables that produce optimum $\dot{W}_{exp}$ and $\eta_{thermal}$. The collared area contours are the predicted results of the ANN results, the dots represent the actual experimental results, the triangle are the optimized efficiency, located in a high-performance region, and the colour changes in all three indicate the large prediction values of $\dot{W}_{exp}$ values (~1200 MW) and dark blue indicating lower values (~600 MW). While $\eta_{thermal}$ which describe a higher efficiency (15% and above) is indicated in yellow, while lower efficiency (5%) is represented by dark blue. In Fig. 4.40a, the actual value of $\dot{W}_{exp}$ (1000-1200 Watt) is at a $\dot{m}$ and P_1 in the range of 60-100 g/s and 12-20 Bar, respectively. Anomalies occur with the predicted results in predicted-$\dot{W}_{exp}$ occur at high of $\dot{m}$ (>120 g/s) and P_1 (>14 Bar) only. This also occurs in the results of actual-$\eta_{thermal}$ vs predicted-$\eta_{thermal}$ with value of around (9-10 %) and (13-15%) shown by Fig. 4.40b, which are in the range of $\dot{m}$ (70-120 g/s) and P_1 (6-14 Bar).

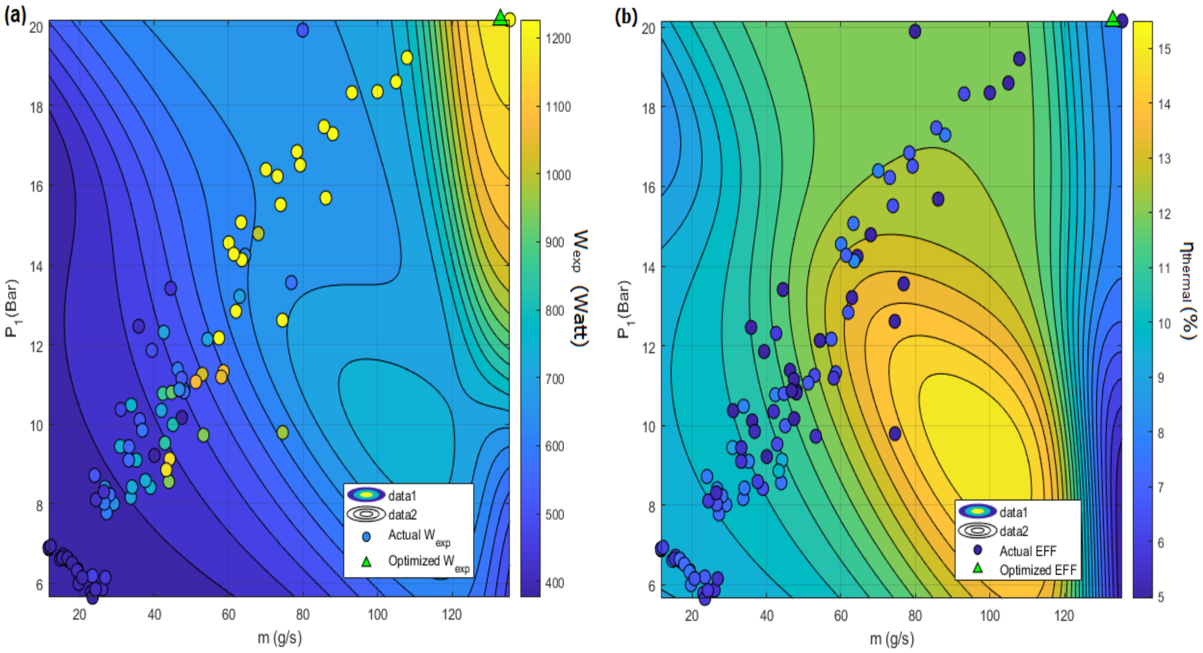

Fig. 4.40. Performance map of predicted vs actual vs optimization: a) $\dot{W}_{exp}$, b) $\eta_{thermal}$

The Pareto optimal frontier for maximizing both $\dot{W}_{exp}$ and $\eta_{thermal}$ are calculated and illustrated in Fig. 4.41. The trade-offs between these objectives, illustrating that both cannot be simultaneously maximized. The optimal solution (green square) reflects a compromise, guided by system priorities. All the optimal design points along the Pareto frontier are non-dominated, giving decision-makers flexibility in selecting the best operational parameters. As $\eta_{thermal}$ is increases, net output work decreases.

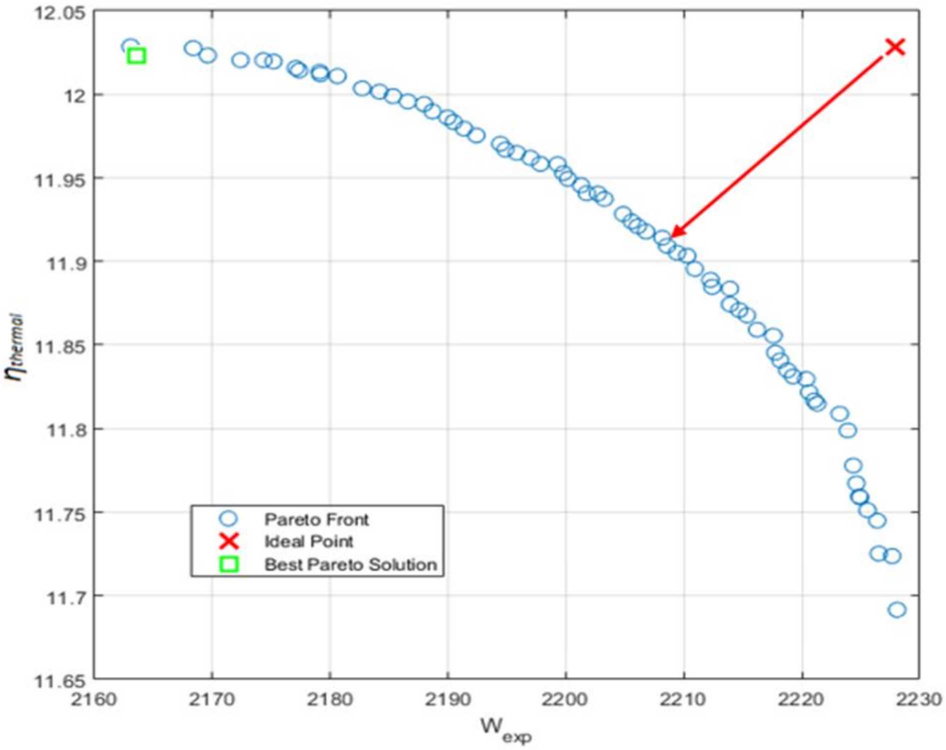

Fig. 4.41. Pareto front performance result

The ideal point achieves the highest $\eta_{thermal}$ of 11.91% and a $\dot{W}_{exp}$ of 2209 W, while the best Pareto solution yields the lowest $\dot{W}_{exp}$ of 2163.4 Watt but with a higher $\eta_{thermal}$ of 12.03%. Simultaneously reaching maximum thermal efficiency and net output work is not possible. It is important to note that the best Pareto solution represents the outcome of multi-objective optimization with $\dot{W}_{exp}$ and $\eta_{thermal}$ as the objective functions. The Technique for Order Preference by Similarity to Ideal Solution (TOPSIS) is applied to select the optimal Pareto solution, which identifies alternatives with the shortest distance to the positive ideal solution and the farthest distance from the negative ideal solution. The Pareto-optimal solution achieves a $\eta_{thermal}$ of 7.76% and a $\dot{W}_{exp}$ of 2.31 kW. Table 4.10 summarizes the optimal operating parameters (T_1, T_2, P_1, P_2, T_{cond}, $\dot{m}$, N_{pump}) required to achieve both the highest $\dot{W}_{exp}$ and $\eta_{thermal}$ for both the ideal point and the best Pareto solution.

Table 4.10. Optimisation results

	Variables	**Value**	**Unit**
Input	$\dot{m}$	68.303	g/s
	T_1	140.95	°C
	T_2	99.671	°C
	P_1	6.0199	Bar
	P_2	1.4473	Bar
	T_{cond}	33.033	°C
	N_{pump}	5800.6	RPM
Ideal point	$\dot{W}_{exp}$	2209	W
	$\eta_{thermal}$	11.91	%
Best Pareto solution	$\dot{W}_{exp}$	2163.4	W
	$\eta_{thermal}$	12.03	%

5. NEW SCIENTIFIC RESULTS

This section presents the new scientific findings from this research work as follows:

1. ORC utilisation using geothermal excess steam in low temperature range

The low temperature of geothermal power-plant excess-steam can be exploited via ORC. Therefore, I have investigated the key performance differences among various working fluids for ORC systems, particularly in relation to evaporator pressure. Propane emerged as the highest performer, achieving a notable network of 41 kW at 2.48 MPa, while in terms of thermal efficiency, R134a excelled with 11.98% at 2.03 MPa, making it the most efficient for heat utilization.

Using exergy analysis, I confirmed that the evaporator consistently exhibited the highest losses, especially when using propane, but also the highest exergy efficiency, a unique balance I found critical to overall ORC performance. Furthermore, exergy sustainability indicators revealed R143a as the most sustainable choice with the highest value of ESI (0.5026) and the lowest value of EEF (1.989), while propane, despite its power advantages, had the highest EEF at 2.472, marking a higher environmental impact. These findings underscore how fluid selection and pressure adjustments can substantially enhance ORC efficiency and sustainability, providing actionable insights into optimizing ORC systems.

2. Sizing and selecting PCMs for solar-ORC integrating with thermal energy storage

In analysing solar-ORC from different climate condition and regional I have explored the regional optimization of Solar-ORC systems and demonstrated their adaptability to diverse climatic conditions, with significant findings from studies in Europe and south-east Asia. In Hungary as a representative, I found that strong summer solar radiation, particularly in August, enabled substantial ORC output, with a system using R245fa achieving an impressive power production of 45.5 kW. This result underscores the high potential of solar thermal applications in regions with intense seasonal sunlight. Meanwhile, in tropical climates such as Indonesia, I assured that Solar-ORC systems maintained stable, year-round performance, with R134a producing a daily power of approximately 685 W and R245fa achieving a peak efficiency of 7.45%, confirming their suitability for consistent tropical irradiation.

My approach involved analysing the role of PCMs and TES designs. In Central-European such as Hungary, I identified organic PCMs like N-Octacosane as highly efficient, achieving a dimensionless mass parameter of 1.26 at a melting temperature of 370 K, ideal for temperature-sensitive storage systems. In contrast, I achieved the reliability of inorganic PCMs for Southeast Asia (Indonesia), particularly using salt hydrates, when used in a 250 L thermal energy storage system, effectively storing power up to 500 W. These findings highlight the importance of tailoring PCM and TES solutions to specific climatic conditions, with my Hungarian study emphasizing the benefits of high solar peaks for ORC performance, while my work in South-East Asia showcased the reliability of stable, year-round systems. Together, these insights contribute to advancing Solar-ORC technology and its global applications through region-specific PCM-TES designs.

3. *Energy, exergy, environment and economy (4E) aspect of Biomass-ORC*

In finding an energy, exergy, environment and economy value of Biomass-ORC I have evaluated both a biomass ORC system fuelled by Napier grass and a test-rig system using woodwaste combustion. A key challenge I identified was finding the right balance between operational performance and costs. For the biomass-ORC system, I found that R245fa outperformed R123 in terms of expander power and economic viability, making it the preferred working fluid. I also recommended cultivating Napier grass in underutilized oil palm plantation areas to meet biomass demands. In the 150 kW of biomass-ORC test-rig system, I optimized parameters like mass flow rate, isentropic efficiency, and evaporator pressure, which significantly boosted performance. I achieved 171.5 kW of power output and a thermal efficiency of 37.4% by adjusting these parameters. Additionally, by using a regenerator to recover heat from the expander, I was able to minimize exergy destruction and improve overall efficiency. Therefore, the existing biomass-ORC plant is already using R134a as the working fluid. According to further analysis, R134a considered known as environmental benefits, and the system showed strong economic potential with an NPV of 238 k€, LCOE of 0.93 €/kWh, and SPB of 26-27 years. These findings highlight the importance of optimizing fluid choice, operating conditions, and biomass resources to enhance both the performance and sustainability of biomass-ORC systems.

4. *The prediction and multi-objective optimisation from ORC experiment results through ANN*

Experimental investigations of the 2 kW ORC test rig have been carried out. Based on experiment result, I found that experimental value can be predicted by employing machine learning through ANN, and high possibly enough from another heat source. I found that the ANN model achieved a high prediction accuracy (MSE ~1.24%), offering a robust and reliable approach for ORC performance prediction. This approach provides a substantial quantitative edge over traditional models, which often struggle with ORC’s non-linear and dynamic behaviours. The model’s precision in capturing power output variations marks a major advancement, allowing for more accurate forecasting of ORC responses to fluctuating inputs, such as mass flow rate and pressure. This improvement supports more adaptable ORC operations, a critical factor for managing the variability inherent in renewable energy sources. Through implementing ANN-driven multi-objective optimization, I established a method to enhance both power output and thermal efficiency in ORC systems. For instance, the optimized expander achieved an output power of 2229 W with a thermal efficiency of 11.67%. These results provide actionable insights into optimal configurations for ORC performance, offering a meaningful contribution that can be adapted to different ORC setups and conditions. This optimization framework has strong potential for customized, high-performance designs, which are increasingly essential in industry-specific renewable energy applications.

6. CONCLUSION

The findings in this dissertation contribute substantially to the advancement of ORC research by exploring the potential of geothermal, biomass, and solar sources for sustainable power generation through comprehensive energy, exergy, and environmental analyses, as well as predictive modelling and optimization techniques.

The study on geothermal waste heat recovery revealed that selecting optimal working fluids can significantly enhance ORC performance. Propane achieved the highest power output of 41 kW at a pressure of 2.48 MPa, while R134a demonstrated the greatest thermal efficiency of 11.97% at 2.97 MPa. Propane also showed the highest exergy efficiency, reaching 79%, highlighting its suitability for efficient energy conversion. Environmental analysis further indicated R125 as the least impactful fluid, with the lowest EWR value (0.2397), suggesting its minimal environmental footprint. However, R134a had the highest ESI value, emphasizing the importance of balancing environmental impact with operational efficiency.

In biomass-ORC systems, Napier grass was confirmed as a viable feedstock for Indonesia, given its high heating value. Through thermoeconomic analysis, R245fa was identified as the more cost-effective fluid, with lower investment costs (2311.68 USD/kWe) compared to R123. For large-scale biomass-based ORC in Italy, optimization indicated a need for adjustments in mass flow rate, evaporator, and condenser pressures to achieve a power output close to the designed capacity (149.56 kW) and a thermal efficiency of 13.77%. The economic analysis showed that biomass-ORC has competitive viability, supported by favourable NPV and LCOE values and a reasonable payback period of 24 years.

For Solar-ORC systems, regional climatic differences between Hungary and Indonesia underscored the need for tailored TES and PCM integration to maximize efficiency. In Hungary, the high solar radiation peaks allowed for notable outputs, with R245fa producing power 45.5 kW during August, highlighting temperate climates' potential for high-efficiency solar-thermal applications. In Indonesia, stable year-round solar radiation supported consistent Solar-ORC output, with R134a producing a daily power output of 685 W, and R245fa achieving peak efficiency at 7.45%. PCM analysis confirmed that inorganic salt hydrates with high latent heat storage are effective for TES, especially for extended night use in Indonesia, where a 300L capacity could sustain ORC operations for up to five hours at 500W.

Finally, ANN analysis for a waste heat recovery ORC prototype demonstrated the model's high prediction accuracy, with MSE of approximately 1.24%, supporting reliable performance predictions in ORC systems. The ANN-based optimization achieved an expander power of 2229 W and thermal efficiency of 11.67%, showcasing ANN's capability to model ORC's complex, non-linear behaviours and offering a robust tool for optimizing ORC designs. Uncertainty analysis validated the predictive reliability, with absolute errors for power and efficiency below 250 W and 40%, respectively.

7. SUMMARY

The study focuses on utilization ORC systems to harness renewable energy sources such as geothermal, biomass, and solar energy. The ORC, a variation of the conventional Steam Rankine Cycle, uses low-boiling-point organic fluids, enabling power generation from moderate and low-temperature heat sources, which traditional systems cannot efficiently utilize. ORC technology is explored in various applications across Europe (Hungary and Italy) and Asia (Indonesia), particularly in areas with abundant geothermal and solar resources. The research examines ORC's performance and suitability in different regions, utilizing thermodynamic, exergy, environmental and economic analyses (4E) to optimize energy conversion efficiency and sustainability.

A key challenge addressed is the limited adoption of ORC in regions with substantial renewable energy potential, such as Indonesia, where geothermal and solar resources remain underutilized for ORC applications. The study aims to fill this gap by investigating ORC configurations tailored for each resource type and optimizing performance across multiple ORC implementations. It also integrates ANN to predict and improve ORC efficiency. Additionally, the study assesses solar ORC systems in Hungary and Indonesia, factoring in the intermittent nature of solar energy and evaluating TES options for continuous power output.

For instance, in the geothermal ORC application, propane emerged as the optimal working fluid, achieving a peak work output ($\dot{W}_{net}$). While, R134a demonstrated the highest efficiency. For solar-ORC in Hungary, ORC system, using R245fa as the working fluid, produced a maximum output power of 45.5 kW in August, which aligns with the region's peak solar radiation period. Meanwhile, in the Indonesian region, consistent solar irradiance allowed for a steady daily output of around 685 Wh with R134a and a peak efficiency of 7.45% for R245fa. These results underscore the importance of regional customization and PCM selection in sustaining high solar-ORC performance across different climates. For 150 kWe biomass-ORC plant in Bologna, Italy, the study achieved power output optimization by adjusting variables like mass flow rate, isentropic efficiency, and evaporator pressure using R134a. The economic analysis indicated that the biomass-ORC plant presented a viable investment through LCOE method. Additionally, the study assessed the biomass demand based on working fluid differences. The findings suggest that R245fa is more cost-effective for ORC biomass utilization due to lower overall component costs, despite the slightly higher land requirements for biomass feedstock

Further, the use of ANN models to optimize ORC parameters demonstrated predictive accuracy and optimization potential, achieving an impressive thermal efficiency in the ideal Pareto solution. The ANN-based optimization enabled adjustments across parameters like mass flow rate, inlet pressures, and pump speeds, leading to targeted improvements in ORC performance, demonstrating a pathway to enhanced efficiency and economic viability for ORC systems.

8. ÖSSZEFOGLALÁS (SUMMARY IN HUNGARIAN)

A disszertáció az Organikus Rankine Ciklus (ORC) alkalmazhatóságára öszpontosít a megújuló energiaforrások, pl. geotermikus, biomassza- és napenergia hasznosítása során. Az ORC, amely a hagyományos gőz munkaközegű Rankine-ciklus egy változata, alacsony forráspontú szerves folyadékokkal működik, lehetővé téve az energiatermelést a közepes és alacsony hőmérsékletű hőforrásokból, amelyeket a hagyományos rendszerek nem képesek hatékonyan hasznosítani. Az ORC technológiát különféle alkalmazásokban kutatják Európában (Magyarország és Olaszország) és Ázsiában (Indonézia), különösen olyan területeken, ahol bőséges geotermikus és napenergia források állnak rendelkezésre. A kutatás az ORC teljesítményét és alkalmazhatóságát vizsgálja különböző régiókban a termodinamikai, exergia, környezeti és gazdasági (4E) elemzések felhasználásával az energiaátalakítás hatékonyságának és fenntarthatóságának optimalizálása érdekében.

A tanulmány egyik kihívása az ORC korlátozott elterjedtsége azokban a régiókban, ahol jelentős megújulóenergia-potenciál van, pl. Indonéziában, ahol alacsony a geotermikus és napenergiaforrások elterjedtsége az ORC alkalmazások területén. A tanulmány ezt a hiányt pótolja azáltal, hogy megvizsgálja az egyes erőforrástípusokra javasolt ORC-konfigurációkat, és azok teljesítményét különböző implementációk optimalizálásával. A tanulmány mesterséges neurális hálózatos (ANN) modellezést is felhasználja az ORC hatékonyságának előrejelzésére és javítására. Emellett megvizsgálja a napelemes ORC-rendszereket Magyarországon és Indonéziában, figyelembe véve a napenergia időszakos jellegét, és értékeli az energiatárolási (TES) lehetőségeket a folyamatos energiatermelés biztosítására.

Pl. a geotermikus ORC-alkalmazásban a propán bizonyult a legoptimálisabb munkaközegnek mivel a legmagasabb teljesítményt ($\dot{W}_{net}$) adott, míg az R134a mutatta a legnagyobb hatékonyságot. Magyarországon a napenergiával működő ORC-rendszer, amely R245fa-t használ munkaközegként, augusztusban 45,5 kW teljesítményt mutatott, ami a régió csúcs napsugárzási időszakával esik egybe. Eközben az indonéz régióban a folyamatos napsugárzás napi 685 Wh körüli állandó termelést tett lehetővé R134a-val, és az R245fa esetében 7,45%-os csúcs hatékonyságot hozott. Ezek az eredmények kiemelik a regiós adottságok figyelembevételét és a fázisváltó anyagok (PCM) kiválasztásának fontosságát a napenergiás ORC-rendszerek magas teljesítményének biztosítására különböző éghajlatoknál. Az olaszországi Bolognában működő 150 kWe biomassza-ORC üzem esetében a tanulmány a tömegáram, az izentrópikus hatékonyság és a párolgási nyomás beállításával optimalizálta a teljesítményt R134a használa esetén. A gazdasági elemzés szerint a biomassza-ORC üzem a LCOE módszer alapján életképes beruházásnak bizonyult. Emellett a tanulmány a biomassza-igényt is vizsgálta különböző munkaközeg esetére. Az eredmények azt mutatták, hogy az R245fa költséghatékonyabb az ORC biomassza-hasznosításban, mivel az eszköz összköltsége alacsonyabb, ugyanakkor a biomassza alapanyaghoz nagyobb földterület szükséges.

Az ANN-modellek alkalmazása az ORC paramétereinek meghatározására becsülhető pontosságot és optimalizálási potenciált adott, és jó termikus hatékonyságot mutatott. Az ANN-alapú optimalizálás lehetővé tette a tömegáram, belépési nyomások és szivattyú sebességek finomhangolását, ami javulásokat eredményezett az ORC teljesítményében, valamint a hatékonyság és gazdaságosság növelésében.

9. APPENDICES

A1: Bibliography

Abam, F.I., Ekwe, E.B., Effiom, S.O., Ndukwu, M.C., 2018. A comparative performance analysis and thermo-sustainability indicators of modified low-heat organic Rankine cycles (ORCs): An exergy-based procedure. Energy Rep. 4, 110–118. DOI: 10.1016/j.egyr.2017.08.003

Ahmadi, G., Toghraie, D., Akbari, O., 2019. Energy, exergy and environmental (3E) analysis of the existing CHP system in a petrochemical plant. Renew. Sustain. Energy Rev. 99, 234–242. DOI: 10.1016/j.rser.2018.10.009

Aiken, L.S., Coxe, S., 2010. Linear Regression. John Wiley and Sons.

Alguacil, M., Prieto, C., Rodriguez, A., Lohr, J., 2014. Direct Steam Generation in Parabolic Trough Collectors. Energy Procedia 49, 21–29. DOI: 10.1016/j.egypro.2014.03.003

Alshibil, A.M.A., Farkas, I., Víg, P., 2022. Multi-aspect approach of electrical and thermal performance evaluation for hybrid photovoltaic/thermal solar collector using TRNSYS tool. Int. J. Thermofluids 16, 100222. DOI: 10.1016/j.ijft.2022.100222

Alvi, J.Z., Feng, Y., Wang, Q., Imran, M., Alvi, J., 2020. Modelling, simulation and comparison of phase change material storage based direct and indirect solar organic Rankine cycle systems. Appl. Therm. Eng. 170, 114780. DOI: 10.1016/j.applthermaleng.2019.114780

Anastasovski, A., Rasković, P., Guzović, Z., 2020. A review of heat integration approaches for organic rankine cycle with waste heat in production processes. Energy Convers. Manag. 221, 113175. DOI: 10.1016/j.enconman.2020.113175

Arkar, C., Medved, S., 2015. Optimization of latent heat storage in solar air heating system with vacuum tube air solar collector. Sol. Energy 111, 10–20. DOI: 10.1016/j.solener.2014.10.013

ASHRAE, 2021. ASHRAE Handbook—Fundamentals, Inch-Pound. ed.

Aydin, H., 2013. Exergetic sustainability analysis of LM6000 gas turbine power plant with steam cycle. Energy 57, 766–774. DOI: 10.1016/j.energy.2013.05.018

Badr, O., O'Callaghan, P.W., Hussein, M., Probert, S.D., 1984. Multi-vane expanders as prime movers for low-grade energy organic Rankine-cycle engines. Appl. Energy 16, 129–146. DOI: 10.1016/0306-2619(84)90060-6

Bai, Z., Liu, Q., Lei, J., Jin, H., 2018. Investigation on the mid-temperature solar thermochemical power generation system with methanol decomposition. Appl. Energy 217, 56–65. DOI: 10.1016/j.apenergy.2018.02.101

Banja, M., Sikkema, R., Jégard, M., Motola, V., Dallemand, J.-F., 2019. Biomass for energy in the EU – The support framework. Energy Policy 131, 215–228. DOI: 10.1016/j.enpol.2019.04.038

Bao, J., Lin, Y., Zhang, R., Zhang, N., He, G., 2017. Effects of stage number of condensing process on the power generation systems for LNG cold energy recovery. Appl. Therm. Eng. 126, 566–582. DOI: 10.1016/j.applthermaleng.2017.07.144

Bao, J., & Zhao, L. (2013). A review of working fluid and expander selections for Organic Rankine Cycle. Renewable and Sustainable Energy Reviews, 24, 325-342.

Bejan, A., Tsatsaronis, G., Moran, M.J., 1995. Thermal Design and Optimization. John Wiley and Sons.

Bellos, E., Sarakatsanis, I., Tzivanidis, C., 2020. Investigation of Different Storage Systems for Solar-Driven Organic Rankine Cycle. Appl. Syst. Innov. 3, 52. DOI: 10.3390/asi3040052

Bellos, E., Tzivanidis, C., 2019. Design of a solar-driven cogeneration system using flat plate collectors and evacuated tube collectors. Int. J. Energy Res. 43, 5841–5851. DOI: 10.1002/er.4689

Boda, K., 2016. Fostering geothermal development in hungary: opportunities and bottlenecks. Presented at the UNU-GTP, United Nations University, Reykjavik, Iceland.

Bracmort, K., 2019. Biomass: Comparison of Definitions in Legislation. Congressional Research Service.

Braimakis, K., Charalampidis, A., Karellas, S., 2021. Techno-economic assessment of a small-scale biomass ORC-CHP for district heating. Energy Convers. Manag. 247, 114705. DOI: 10.1016/j.enconman.2021.114705

Braimakis, K., Karellas, S., 2018. Exergetic optimization of double stage Organic Rankine Cycle (ORC). Energy 149, 296–313. DOI: 10.1016/j.energy.2018.02.044

Buonomano, A., Calise, F., Palombo, A., 2013. Solar heating and cooling systems by CPVT and ET solar collectors: A novel transient simulation model. Appl. Energy 103, 588–606. DOI: 10.1016/j.apenergy.2012.10.023

Burhanuddin, H., Willy, A., Abdurrachim, Pasek, A.D., 2019. Thermodynamic Analysis of Supercritical Organic Rankine Cycle with Propane (R-290) as a Working Fluid. Presented at the The 10th AUN/SEED-Net RC MEManuE.

Calise, F., d'Accadia, M.D., Vicidomini, M., 2019. Optimization and dynamic analysis of a novel polygeneration system producing heat, cool and fresh water. Renew. Energy 143, 1331–1347. DOI: 10.1016/j.renene.2019.05.051

Campana, C., Cioccolanti, L., Renzi, M., Caresana, F., 2019. Experimental analysis of a small-scale scroll expander for low-temperature waste heat recovery in Organic Rankine Cycle. Energy 187, 115929. DOI: 10.1016/j.energy.2019.115929

Carberry, J.J., Fair, J.R., Schowalter, W.P., Tipell, M., Wei, J., Peters, M.S., 1991. McGraw-Hill Chemical Engineering Series. Mc Graw-hill Education.

ChemSpider, 2023. Search and share chemistry. URL http://www.chemspider.com/ (accessed 3.20.23).

Chen, H., Goswami, D.Y., Stefanakos, E.K., 2010. A review of thermodynamic cycles and working fluids for the conversion of low-grade heat. Renew. Sustain. Energy Rev. 14, 3059–3067. DOI: 10.1016/j.rser.2010.07.006

Chitgar, N., Hemmati, A., Sadrzadeh, M., 2023. A comparative performance analysis, working fluid selection, and machine learning optimization of ORC systems driven by geothermal energy. Energy Convers. Manag. 286, 117072. DOI: 10.1016/j.enconman.2023.117072

Coolset, 2023. Global Warming Potential (GWP).

Daniarta, S., Imre, A.R., 2020. Cold Energy Utilization in LNG Regasification System Using Organic Rankine Cycle and Trilateral Flash Cycle. Period. Polytech. Mech. Eng. 64, 342–349. DOI: 10.3311/PPme.16668

Daniarta, S., Kolasiński, P., Imre, A.R., Sowa, D., 2024. Artificial intelligence-driven performance mapping: A deep learning-based investigation of a multi-vane expander in retrofitted organic Rankine cycle. Energy Convers. Manag. 315, 118763. DOI: 10.1016/j.enconman.2024.118763

Daniarta, S., Kolasiński, P., Rogosz, B., 2022. Waste Heat Recovery in Automotive Paint Shop via Organic Rankine Cycle and Thermal Energy Storage System—Selected Thermodynamic Issues. Energies 15, 2239. DOI: 10.3390/en15062239

Daniarta, S., Nemś, M., Kolasiński, P., 2023. A review on thermal energy storage applicable for low- and medium-temperature organic Rankine cycle. Energy 278, 127931. DOI: 10.1016/j.energy.2023.127931

Darvish, K., Ehyaei, M., Atabi, F., Rosen, M., 2015. Selection of Optimum Working Fluid for Organic Rankine Cycles by Exergy and Exergy-Economic Analyses. Sustainability 7, 15362–15383. DOI: 10.3390/su71115362

De Lucia, M., Pierucci, G., Manieri, M., Agostini, G., Giusti, E., Salvestroni, M., Taddei, F., Cottone, F., Fagioli, F., 2024. Experimental Characterization of Commercial Scroll Expander for Micro-Scale Solar ORC Application: Part 1. Energies 17, 2205. DOI: 10.3390/en17092205

Dickson, M., Fanelli, M., n.d. What is Geothermal energy?

DiPippo, R., 2012. Geothermal Power Plants: Principles, Applications, Case Studies and Environmental Impact, 3rd ed. Elsevier.

Direktorat Perencanaan Korporat, 2021. Diseminasi RUPTL 2021-2030.

Dong, L., Liu, H., Riffat, S., 2009. Development of small-scale and micro-scale biomass-fuelled CHP systems – A literature review. Appl. Therm. Eng. 29, 2119–2126. DOI: 10.1016/j.applthermaleng.2008.12.004

Douglas, T.B., Dever, J.L., 1955. Enthalpy and specific heat of four corrosion-resistant alloys at high temperatures. J. Res. Natl. Bur. Stand. 54, 15. DOI: 10.6028/jres.054.002

Enertime, 2011. The Organic Rankine Cycle and its applications.

Everitt, N., 2023. Pfas ban affects most refrigerant blends, Cooling Post.

FAO, 2017. The future of food and agriculture: trends and challenges. Food and Agriculture Organization of the United Nations, Rome.

Feldhof, J.F., 2012. Direct Steam Generation (DSG) - Technology Overview. SFERA Summer School, Almeria, Spain.

Fraia, S.D., Shah, M., Vanoli, L., 2023. A biomass-based polygeneration system for a historical building: A techno-economic and environmental analysis. Energy Convers. Manag. 291, 117336. DOI: 10.1016/j.enconman.2023.117336

Freeman, J., Guarracino, I., Kalogirou, S.A., Markides, C.N., 2017. A small-scale solar organic Rankine cycle combined heat and power system with integrated thermal energy storage. Appl. Therm. Eng. 127, 1543–1554.

DOI: 10.1016/j.applthermaleng.2017.07.163

Ganassin, S., van Buijtenen, J.P., 2015. SMALL SCALE SOLID BIOMASS FUELLED ORC PLANTS FOR COMBINED HEAT AND POWER. Presented at the 3rd International Seminar on ORC Power system, Brussel, Belgium, p. 59.

Goswami, Y.D., 2022. Principles of Solar Engineering Accessibility symbol Accessibility Information Book Principles of Solar Engineering, 4th ed. Taylor and Francis.

Habibi, R., Mehrpooya, M., Pourmoghadam, P., 2021. Integrated Mg-Cl hydrogen production process and CaO/CaCO3-CaCl2 thermochemical energy storage phase change system using solar tower system. Energy Convers. Manag. 245, 114555. DOI: 10.1016/j.enconman.2021.114555

He, T., Chong, Z.R., Zheng, J., Ju, Y., Linga, P., 2019. LNG cold energy utilization: Prospects and challenges. Energy 170, 557–568. DOI: 10.1016/j.energy.2018.12.170

Heberle, F., Brüggemann, D., 2010. Exergy based fluid selection for a geothermal Organic Rankine Cycle for combined heat and power generation. Appl. Therm. Eng. 30, 1326–1332. DOI: 10.1016/j.applthermaleng.2010.02.012

Hertel, J.D., Canals, V., Pujol-Nadal, R., 2020. On-site optical characterization of large-scale solar collectors through ray-tracing optimization. Appl. Energy 262, 114546. DOI: 10.1016/j.apenergy.2020.114546

Hossain, M.S., Saidur, R., Fayaz, H., Rahim, N.A., Islam, M.R., Ahamed, J.U., Rahman, M.M., 2011. Review on solar water heater collector and thermal energy performance of circulating pipe. Renew. Sustain. Energy Rev. 15, 3801–3812. DOI: 10.1016/j.rser.2011.06.008

Imran, M., Usman, M., Park, B.-S., Lee, D.-H., 2016. Volumetric expanders for low grade heat and waste heat recovery applications. Renew. Sustain. Energy Rev. 57, 1090–1109. DOI: 10.1016/j.rser.2015.12.139

Indonesia’s State Electricity Company, 2020. RENCANA USAHA PENYEDIAAN TENAGA LISTRIK 2021-2030. PLN Persero.

Italy Electricity Price, 2024.

Jones, A., Green, R., & White, S. (2020). Concentrating Solar Power and Organic Rankine **Cycles**. Renewable Energy Technology Studies, 45(3), 567–582 Doi: 10.1016/j.rentes.2020.0567

Karellas, S., Braimakis, K., 2016. Energy–exergy analysis and economic investigation of a cogeneration and trigeneration ORC–VCC hybrid system utilizing biomass fuel and solar power. Energy Convers. Manag. 107, 103–113. DOI: 10.1016/j.enconman.2015.06.080

Kolasiński, P., 2020. Experimental and modelling studies on the possible application of heat storage devices for powering the ORC (organic rankine cycle) systems. Therm. Sci. Eng. Prog. 19, 100586. DOI: 10.1016/j.tsep.2020.100586

Kristiyadi, T., Permana, D.I., Sirodz, M.P.N., Saefudin, E., Farkas. I. 2022. Performance and Emission of Diesel Engine Fuelled by Commercial Bio-Diesel Fuels in Indonesia, Acta Technologica Agriculturae, 25(4): 32, doi: https:/DOI: 10.2478/ata-2022-0032

Ktistis, P.K., Agathokleous, R.A., Kalogirou, S.A., 2021. Experimental performance of a parabolic trough collector system for an industrial process heat application. Energy 215, 119288. DOI: 10.1016/j.energy.2020.119288

Lakew, A.A., Bolland, O., 2010. Working fluids for low-temperature heat source. Appl. Therm. Eng. 30, 1262–1268. DOI: 10.1016/j.applthermaleng.2010.02.009

Langdon, D., 2024. Spon's Mechanical and Electrical Services Price Book 2010, 41st ed. Spon Press, London.

Lecompte, S., Huisseune, H., Van Den Broek, M., Vanslambrouck, B., De Paepe, M., 2015. Review of organic Rankine cycle (ORC) architectures for waste heat recovery. Renew. Sustain. Energy Rev. 47, 448–461. DOI: 10.1016/j.rser.2015.03.089

Lee, H., Kim, J., & Park, M. (2021). Global Solar Irradiation Utilization in Low-Temperature Applications. Journal of Solar Energy Engineering, 143(7), 1121–1135. DOI: 10.1016/j.jsolenergy.2021.1121

Lemmens, S., 2016. Cost Engineering Techniques and Their Applicability for Cost Estimation of Organic Rankine Cycle Systems. Energies 9, 485. DOI: 10.3390/en9070485

Lemmon, E.W., Huber, M.L., McLinden, M.O., 2013. NIST Reference Fluid Thermodynamic and Transport Properties— REFPROP.

Limberger, J., Boxem, T., Pluymaekers, M., Bruhn, D., Manzella, A., Calcagno, P., Beekman, F., Cloetingh, S., Van Wees, J.-D., 2018. Geothermal energy in deep aquifers: A global assessment of the resource base for direct heat utilization. Renew. Sustain. Energy Rev. 82, 961–975. DOI: 10.1016/j.rser.2017.09.084

Lingayat, A.B., Suple, Y.R., 2013. Review on Phase Change Material as Thermal Energy Storage Medium: Materials, Application. Int. J. Eng. Res. 3.

Liu, W., Wang, J., Richard, T.L., Hartley, D.S., Spatari, S., Volk, T.A., 2017. Economic and life cycle assessments of biomass utilization for bioenergy products. Biofuels Bioprod. Biorefining 11, 633–647. DOI: 10.1002/bbb.1770

Loni, R., Mahian, O., Markides, C.N., Bellos, E., Le Roux, W.G., Kasaeian, A., Najafi, G., Rajaee, F., 2021. A review of solar-driven organic Rankine cycles: Recent challenges and future outlook. Renew. Sustain. Energy Rev. 150, 111410. DOI: 10.1016/j.rser.2021.111410

Lozano, M.A., Valero, A., 1993. THEORY OF THE EXERGETIC COST~. Energy 18. DOI: 10.1016/0360-5442(93)90006-y

Macchi, E., Astolfi, M., 2017. ORC Power system: Technologies and Applications.

Mago, P.J., Srinivasan, K.K., Chamra, L.M., Somayaji, C., 2008. An examination of exergy destruction in organic Rankine cycles. Int. J. Energy Res. 32, 926–938. DOI: 10.1002/er.1406

Malico, I., Nepomuceno Pereira, R., Gonçalves, A.C., Sousa, A.M.O., 2019. Current status and future perspectives for energy production from solid biomass in the European industry. Renew. Sustain. Energy Rev. 112, 960–977. DOI: 10.1016/j.rser.2019.06.022

Marion, M., Voicu, I., Tiffonnet, A.-L., 2014. Wind effect on the performance of a solar organic Rankine cycle. Renew. Energy 68, 651–661. DOI: 10.1016/j.renene.2014.03.010

Md Said, M.S., Wan Abdul Karim Ghani, W.A., Hong Boon, T., Hussain, S.A., Ng, D.K.S., 2019. Thermochemical Conversion of Napier Grass for Production of Renewable Syngas. Processes 7, 705. DOI: 10.3390/pr7100705

Midilli, A., Kucuk, H., Dincer, I., 2012. Environmental and sustainability aspects of a recirculating aquaculture system. Environ. Prog. Sustain. Energy 31, 604–611. DOI: 10.1002/ep.10580

Mohammed, I., Abakr, Y., Kazi, F., Yusup, S., Alshareef, I., Chin, S., 2015. Comprehensive Characterization of Napier Grass as a Feedstock for Thermochemical Conversion. Energies 8, 3403–3417. DOI: 10.3390/en8053403

Mohan, S., Dinesha, P., Campana, P.E., 2022. ANN-PSO aided selection of hydrocarbons as working fluid for low-temperature organic Rankine cycle and thermodynamic evaluation of optimal working fluid. Energy 259, 124968. DOI: 10.1016/j.energy.2022.124968

Moran, M.J., shapiro, H.N., 2006. Fundamental Engineering Thermodynamics, 5th ed. John Wiley and Sons, USA.

Nusiaputra, Y.Y., Qadri, F., Kuhn, D., Abdurrachim, H., 2015. Empirical Correlation for Optimal Turbine-Inlet Temperature and Pressure for Geothermal Sub- and Supercritical Organic Rankine Cycles (ORC). Presented at the Proceedings World Geothermal Congress 2015, Proceedings World Geothermal Congress 2015 Melbourne, Australia.

Oyekale, J., Heberle, F., Petrollese, M., Brüggemann, D., Cau, G., 2019. Biomass retrofit for existing solar organic Rankine cycle power plants: Conceptual hybridization strategy and techno-economic assessment. Energy Convers. Manag. 196, 831–845. DOI: 10.1016/j.enconman.2019.06.064

Orosz, M., Mueller, A., Quoilin, S., & Hemond, H. 2010. Small scale biomass fueled cogeneration—An overview of an ongoing ORC-based project in Haiti. *Applied Thermal Engineering, 30*(10), 1306-1312.

Pala, L.P.R., Wang, Q., Kolb, G., Hessel, V., 2017. Steam gasification of biomass with subsequent syngas adjustment using shift reaction for syngas production: An Aspen Plus model. Renew. Energy 101, 484–492. DOI: 10.1016/j.renene.2016.08.069

Pallis, P., Gkonis, N., Varvagiannis, E., Braimakis, K., Karellas, S., Katsaros, M., Vourliotis, P., Sarafianos, D., 2019. Towards NZEB in Greece: A comparative study between cost optimality and energy efficiency for newly constructed residential buildings. Energy Build. 198, 115–137. DOI: 10.1016/j.enbuild.2019.06.005

Pan, J., Zou, R., Jin, F., 2016. Experimental Study on Specific Heat of Concrete at High Temperatures and Its Influence on Thermal Energy Storage. Energies 10, 33. DOI: 10.3390/en10010033

Pantaleo, A.M., Camporeale, S., Fortunato, B., 2015. Small scale biomass CHP: Techno-economic performance of steam vs gas turbines with bottoming ORC. Energy Procedia 82, 825–832. DOI: 10.1016/j.egypro.2015.11.819

Parnian Gharamaleki, F., Sharafi Laleh, S., Ghasemzadeh, N., Soltani, S., Rosen, M.A., 2024. Optimization of a Biomass-Based Power and Fresh Water-Generation System by Machine Learning Using Thermoeconomic Assessment. Sustainability 16, 8956. DOI: 10.3390/su16208956

Pcmproduct, 2013. Phase Change Materials: Thermal Management Solutions.

Peng, Y., Lin, X., Liu, J., Su, W., Zhou, N., 2021. Machine learning prediction of ORC performance based on properties of working fluid. Appl. Therm. Eng. 195, 117184. DOI: 10.1016/j.applthermaleng.2021.117184

Perez, F., Garcia, L., & Smith, E. (2018). Efficiency Optimization of Solar-Driven ORC Systems. Applied Thermal Engineering, 96(1), 25–33. DOI: 10.1016/j.apthermeng.2018.0025

Permana, D., Rusirawan, D., Farkas, I., 2021. Waste Heat Recovery of Tura Geothermal Excess Steam Using Organic Rankine Cycle. Int. J. Thermodyn. 24, 32–40. DOI: 10.5541/ijot.906128

Permana, D.I., Mahardika, M.A., Rusirawan, D., Farkas, I., 2024. Utilization of small solar ORC integrated with phase change material in Indonesia condition. J. Energy Storage 92, 112123. DOI: 10.1016/j.est.2024.112123

Permana, Diki I., Rusirawan, D., Farkas, I., 2023. The theoretical approach of the solar organic Rankine cycle integrated with phase change material for the Hungarian region. Energy Sci. Eng. 11, 4429–4445. DOI: 10.1002/ese3.1589

Permana, Diki Ismail, Rusirawan, D., Farkas, I., 2023. Thermoeconomic Analysis of Organic Rankine Cycle From Napier Grass Biomass. Acta Technol. Agric. 26, 99–109. DOI: 10.2478/ata-2023-0014

Permana, D.I., Rusirawan, D., Farkas, I., 2022. A bibliometric analysis of the application of solar energy to the organic Rankine cycle. Heliyon 8, e09220. DOI: 10.1016/j.heliyon.2022.e09220

Persson, J.-G., Sohlenius, S.G., 2008. Petformance Evaluation of Fluid Machinery During Conceptual Design. CIRP Ann. 39. DOI: 10.1016/S0007-8506(07)61020-8

Pessina, D., Facchinetti, D., 2006. Energia dalle biomasse. IRIS Institutional Res. Inf. Syst. - AIR Arch. Ist. Della Ric.

Petrollese, M., Cocco, D., Cau, G., 2017. Small-scale CSP plant coupled with an ORC system for providing dispatchable power: the Ottana Solar Facility. Energy Procedia 129, 708–715. DOI: 10.1016/j.egypro.2017.09.101

Pielichowska, K., Pielichowski, K., 2014. Phase change materials for thermal energy storage. Prog. Mater. Sci. 65, 67–123. DOI: 10.1016/j.pmatsci.2014.03.005

Pourmoghadam, P., Farighi, M., Pourfayaz, F., Kasaeian, A., 2021. Annual transient analysis of energetic, exergetic, and economic performances of solar cascade organic Rankine cycles integrated with PCM-based thermal energy storage systems. Case Stud. Therm. Eng. 28, 101388. DOI: 10.1016/j.csite.2021.101388

Quoilin, S., 2011. Sustainable Energy Conversion Through the Use of Organic Rankine Cycles for Waste Heat Recovery and Solar Applications. University of Liege, Belgium.

Quoilin, S., Broek, M.V.D., Declaye, S., Dewallef, P., Lemort, V., 2013. Techno-economic survey of Organic Rankine Cycle (ORC) systems. Renew. Sustain. Energy Rev. 22, 168–186. DOI: 10.1016/j.rser.2013.01.028

Rahman, A., & Gupta, R. 2022. Non-Concentrating Collectors for ORC Applications. International Journal of Green Energy, 14(2), 88–98. DOI: 10.1016/j.greenenergy.2022.0088

Rentizelas, A., Karellas, S., Kakaras, E., Tatsiopoulos, I., 2009. Comparative techno-economic analysis of ORC and gasification for bioenergy applications. Energy Convers. Manag. 50, 674–681. DOI: 10.1016/j.enconman.2008.10.008

Sadeghi, S., Askari, I.B., 2019. Prefeasibility techno-economic assessment of a hybrid power plant with photovoltaic, fuel cell and Compressed Air Energy Storage (CAES). Energy 168, 409–424. DOI: 10.1016/j.energy.2018.11.108

Setyawati, D., Setiawan, D., 2024. Indonesia's expansion of clean power can spur growth and equality.

Sharma, A., Tyagi, V.V., Chen, C.R., Buddhi, D., 2009. Review on thermal energy storage with phase change materials and applications. Renew. Sustain. Energy Rev. 13, 318–345. DOI: 10.1016/j.rser.2007.10.005

Solargis, 2021a. Solar resource maps of Hungary.

Solargis, 2021b. Solar resource maps in Indonesia.

Soltani, R., Dincer, I., Rosen, M.A., 2015. Thermodynamic analysis of a novel multigeneration energy system based on heat recovery from a biomass CHP cycle. Appl. Therm. Eng. 89, 90–100. DOI: 10.1016/j.applthermaleng.2015.05.081

Somogyi, V., Sebestyén, V., Domokos, E., 2018. Assessment of wastewater heat potential for district heating in Hungary. Energy 163, 712–721. DOI: 10.1016/j.energy.2018.07.157

Su, W., Darkwa, J., Kokogiannakis, G., 2015. Review of solid–liquid phase change materials and their encapsulation technologies. Renew. Sustain. Energy Rev. 48, 373–391. DOI: 10.1016/j.rser.2015.04.044

Sukra, K.F.A., Permana, D.I., Adriansyah, W. 2023. Modelling and Simulation of Existing Geothermal Power Plant: A Case Study of Darajat Geothermal Power Plant. International Journal of Thermodynamics, 26 (2), 13 – 20. DOI: DOI: 10.5541/ijot.1118778

Taheri, M.H., Mosaffa, A.H., Farshi, L.G., 2017. Energy, exergy and economic assessments of a novel integrated biomass based multigeneration energy system with hydrogen production and LNG regasification cycle. Energy 125, 162–177. DOI: 10.1016/j.energy.2017.02.124

Tariq, A.S., Reupke, P., Sarwar, G., 1994. Biomass combustion systems: a guide for monitoring and efficient operation. Natural Resources Institute, Chatham Maritime, Kent, U.K.

Tartière, T., Astolfi, M., 2017. A World Overview of the Organic Rankine Cycle Market. Energy Procedia 129, 2–9. DOI: 10.1016/j.egypro.2017.09.159

Tchanche, B.F., Lambrinos, Gr., Frangoudakis, A., Papadakis, G., 2011. Low-grade heat conversion into power using organic Rankine cycles – A review of various applications. Renew. Sustain. Energy Rev. 15, 3963–3979. DOI: 10.1016/j.rser.2011.07.024

Tchanche, B.F., Lambrinos, Gr., Frangoudakis, A., Papadakis, G., 2010. Exergy analysis of micro-organic Rankine power cycles for a small scale solar driven reverse osmosis desalination system. Appl. Energy 87, 1295–1306. DOI: 10.1016/j.apenergy.2009.07.011

Tereschenko, T., 2016. Energy Planning of Future District Heating Systems with Various Energy Sources (Doctoral theses). NTNU, Norway.

Tian, Y., Zhao, C.Y., 2013. A review of solar collectors and thermal energy storage in solar thermal applications. Appl. Energy 104, 538–553. DOI: 10.1016/j.apenergy.2012.11.051

Tiari, S., Hockins, A., Mahdavi, M., 2021. Numerical study of a latent heat thermal energy storage system enhanced by varying fin configurations. Case Stud. Therm. Eng. 25, 100999. DOI: 10.1016/j.csite.2021.100999

Tzivanidis, C., Bellos, E., Antonopoulos, K.A., 2016. Energetic and financial investigation of a stand-alone solar-thermal Organic Rankine Cycle power plant. Energy Convers. Manag. 126, 421–433. DOI: 10.1016/j.enconman.2016.08.033

Utlu, Z., Tolon, M., Karabuga, A., 2021. Modelling of energy and exergy analysis of ORC integrated systems in terms of sustainability by applying artificial neural network. Int. J. Low-Carbon Technol. 16, 156–164. DOI: 10.1093/ijlct/ctaa033

Valencia Ochoa, G., Castillo Santiago, Y., Duarte Forero, J., Restrepo, J.B., Albis Arrieta, A.R., 2023. A Comprehensive Comparative Analysis of Energetic and Exergetic Performance of Different Solar-Based Organic Rankine Cycles. Energies 16, 2724. DOI: 10.3390/en16062724

Wang, D., Ling, X., Peng, H., Liu, L., Tao, L., 2013. Efficiency and optimal performance evaluation of organic Rankine cycle for low grade waste heat power generation. Energy 50, 343–352.

Wang, R., Jiang, L., Ma, Z., Gonzalez-Diaz, A., Wang, Y., Roskilly, A.P., 2019. Comparative Analysis of Small-Scale Organic Rankine Cycle Systems for Solar Energy Utilisation. Energies 12, 829. DOI: 10.3390/en12050829

Warmanti, M., 2012. Bobot massa dan nilai panas rumput gajah pada berbagai dosisi pupuk NPK di lahan pasir pantai. J. Agrisains 3, 53–62.

Wei, D., Lu, X., Lu, Z., Gu, J., 2007. Performance analysis and optimization of organic Rankine cycle (ORC) for waste heat recovery. Energy Convers. Manag. 48, 1113–1119. DOI: 10.1016/j.enconman.2006.10.020

Weiß, A.P., 2015. Volumetric expander versus turbine – which is the better choice for small orc plants? Presented at the Paper ID: 22, Page 1 3rd International Seminar on ORC Power Systems, Brussels, Belgium.

Wieland, C., Schifflechner, C., Dawo, F., Astolfi, M., 2023. The organic Rankine cycle power systems market: Recent developments and future perspectives. Appl. Therm. Eng. 224, 119980.

Xiaojun, G., Liansheng, L., Yuanyang, Z., Pengcheng, S., n.d. Research on a Scroll Expander Used for Recovering Work in a Fuel Cell.

Yu, H., Helland, H., Yu, X., Gundersen, T., Sin, G., 2021. Optimal design and operation of an Organic Rankine Cycle (ORC) system driven by solar energy with sensible thermal energy storage. Energy Convers. Manag. 244, 114494. DOI: 10.1016/j.enconman.2021.114494

Zarrouk, S.J., Moon, H., 2014. Efficiency of geothermal power plants: A worldwide review. Geothermics 51, 142–153. DOI: 10.1016/j.geothermics.2013.11.001

Zhao, Z., Wang, Y., & Chen, H. 2023. Design Considerations for Solar-Assisted ORC Systems. *Journal of Sustainable Energy Systems*, 31(5), 655–670. DOI: 10.1016/j.sustenergy.2023.0655

Zhao, R., Zhang, H., Song, S., Yang, F., Hou, X., Yang, Y., 2018. Global optimization of the diesel engine–organic Rankine cycle (ORC) combined system based on particle swarm optimizer (PSO). Energy Convers. Manag. 174, 248–259. DOI: 10.1016/j.enconman.2018.08.040

Zhou, J., Chu, Y.T., Ren, J., Shen, W., He, C., 2023. Integrating machine learning and mathematical programming for efficient optimization of operating conditions in organic Rankine cycle (ORC) based combined systems. Energy 281, 128218. DOI: 10.1016/j.energy.2023.128218

A2: Publications related to the dissertation

Refereed papers in foreign languages:

1. **Permana, D.I.,** Rusirawan, D., Farkas, I. (2020). Organic Rankine cycle analysis based on Tura geothermal power-plant excess steam, Mechanical Engineering Letters, Vol. 20, pp. 108-115. HU ISSN 2060-3789. https://www.gek.szie.hu/english/sites/default/files/MEL_2020_20.pdf
2. **Permana, D.I.,** Rusirawan, D., Farkas, I. 2021.Waste heat recovery of Tura geothermal excess steam using organic Rankine cycle, International Journal of Thermodynamics, 24(4), pp. 32-40, doi: DOI: 10.5541.ijot.906128 (Scopus: Q3, IF: 0.8)
3. **Permana, D.I.,** Rusirawan, D., Farkas, I. (2022). A bibliometric analysis of the application of solar energy to the organic Rankine cycle, Heliyon, 8(4), Paper No. e09220, doi: DOI: 10.1016/j.heliyon.2022.e09220 (Scopus: Q1, IF: 4)
4. **Permana, D.I.,** Rusirawan, D., Farkas, I. (2022). Preliminary design of organic Rankine cycle using solar thermal in Hungary, European Journal of Energy Research, 2(3), Paper No. 24018, doi: DOI: 10.24018/ejenergy.2022.2.3.65
5. Krityadi, T., **Permana, D.I.,** Sirodz, M.P.N., Saefudin, E., Farkas, I. (2022). Performance and emission of diesel engine fuelled by commercial bio-diesel fuels in Indonesia, Acta Technologica Agriculturae, 25(3), pp. 221-228, doi: DOI: 10.2478/ata-2022-0032 DOI: 10.2478/ata-2022-0032 (Scopus: Q3, IF: 1.9)
6. Sukra, K.F.A., **Permana, D.I**., Adriansyah, W. 2023. Modelling and Simulation of Existing Geothermal Power Plant: A Case Study of Darajat Geothermal Power Plant. International Journal of Thermodynamics, 26(2), pp. 13–20, doi: DOI: 10.5541/ijot.1118778 (Scopus Q3, IF: 0.8)
7. **Permana, D.I.,** Rusirawan, D., Farkas, I. (2023). Thermoeconomic analysis of organic Rankine cycle from napier grass biomass, Acta Technologica Agriculturae, 26(2), pp. 99-109, doi: DOI: 10.2478/ata-2023-0014 (Scopus: Q2, IF: 1.9)
8. **Permana, D.I.,** Rusirawan, D., Farkas, I. (2023). Theoretical approach of the solar organic Rankine cycle integrated with phase change material for Hungarian region, Energy Science and Engineering, 11(10). pp. 4429-4445, doi: DOI: 10.1002/ese3.1589 (Scopus: Q1, IF: 3.9)
9. **Permana, D.I.,** Mahardika, M.A., Rusirawan, D., Farkas, I. (2024). Utilizaion of small ORC integrated with phase change material in Indonesia condition, Journal of energy storage, 92(4), Paper No. 112123, doi: DOI: 10.1016/j.est.2024.112123 (Scopus: Q1, IF: 8.9)
10. **Permana, D.I.,** Fedeico, F., Delucia, M., Rusirawan, D., Farkas, I. (2024). 4E analysis of Biomass-ORC in Bologna, Italy: A Case Study, Energy Conversion and Managemt: X, 23(7), Paper No. 100646. doi: DOI: 10.1016/j.ecmx.2024.100646 (Scopus: Q1, IF: 7.1)
11. **Permana, D.I.,** Federico, F., Delucia, M., Rusirawan, D., Farkas, I. (2025). Performance evaluation, prediction analysis and optimization of experimental ORC using artificial neural networks (ANN), Energy Nexus, Journal Pre-proof, doi: DOI: 10.1016/j.nexus.2025.100383 (Scopus: Q1, IF: 8)

International conference proceeding

1. **Permana, D.I**., Rusirawan, D., Farkas, I. (2023). Feasibility study of municipal solid waste incinerator and flue gas treatment. The 3rd Faculty of Industrial Technology International Congress (FoITIC) 2021, Bandung, Indonesia. AIP Publishing. Paper No. 03014. Doi: DOI: 10.1063/5.0115257 (Scopus index)
2. **Permana, D.I**., Rusirawan, D., Farkas, I. (2023). Potential utilization of the solar energy using organic Rankine cyle. The 4th International Conference on Green Technology and Design (ICGTD) 2022, Bandung, Indonesia. Link: https://eproceeding.itenas.ac.id/index.php/icgtd/article/view/1342/1545
3. **Permana, D.I**., Rusirawan, D., Farkas, I. (2024). Utilization of small solar-ORC integrated with organic PCMs in Hungary condition. The 4th Faculty of Industrial Technology International Congress (FoITIC) 2021, Bandung, Indonesia. E3C Publishing. Paper No. 030007. Doi: DOI: 10.1051/e3sconf/202448403014 (Scopus index)
4. **Permana, D.I**., Rusirawan, D., Farkas, I. (2024). Solar Organic Rankine Cycle in Bandung Condition: Experimental setup. The 5th International Conference on Green Technology and Design (ICGD) 2023, Bandung, Indonesia. (Scopus index)

International conference abstract

1. **Permana, D.I.,** Farkas, I. (2020). Design and construction of organic Rankine cycle powered by solar thermal heat source, Book of Abstracts, 26th Workshop on Energy and Environment, Gödöllő, Hungary, December 10-11, 2020, p. 26. ISBN 978-963-269-928-8
2. **Permana, D.I.,** Farkas, I. (2021). Various typical solar collectors in ORC applications, Book of Abstracts, 20th International Workshop for Young Scientists (BioPhys Spring 2021), Lublin, Poland, May 18, 2021, p. 55., ISBN 978-83-89969-68-2
3. **Permana, D.I**., Rusirawan, D., Farkas, I. (2021). Empirical correlation of optimal turbine inlet temperature and pressure for geothermal ORC, Book of Abstracts, 27th Workshop on Energy and Environment, Gödöllő, Hungary, December 9-10, 2021, p. 31. ISBN 978-963-269-972-1
4. **Permana, D.I.,** Rusirawan, D., Farkas, I. (2022). A preliminary design and modelling analysis of solar ORC, Book of Abstracts, 21th International Workshop for Young Scientists (BioPhys Spring 2022), Nitra, Slovakia, May 30-31, 2022, p. 85., ISBN 978-83-89969-74-3
5. **Permana D.I.,** Rusirawan D., Farkas,I.: The potential of biomass utilization using Organic Rankine Cycle, Book of Abstracts, 28th Workshop on Energy and Environment, Gödöllő, Hungary, December 8-9, 2022, pp. 51-52. ISBN 978-963-623-016-6
6. **Permana, D.I.,** Rusirawan, D., Farkas, I. (2023). An Energy and exergy analysis of organic Rankine cycle based on Tura GPP excess-steam, Book of Abstracts, 22th International Workshop for Young Scientists (BioPhys Spring 2023), Gödöllő, Hungary, May 30-31, 2023, p. 85., ISBN 978-83-89969-74-3

7. **Permana D.I.,** Rusirawan D., Farkas I.: Organic Rankine cycle powered by solar collector: experimental setup progress, Book of Abstracts, 29th Workshop on Energy and Environment, Gödöllő, Hungary, December 7-8, 2023, pp. 59-60. ISBN 978-963-623-079-1
8. **Permana, D.I.,** Mahardika, M, A., Rusirawan, D., Farkas, I. (2024). Full-time Operation of PCM Integrated Solar Organic Rankine Cycle, Book of Abstracts, 23th International Workshop for Young Scientists (BioPhys Spring 2024), Lublin, Poland, May 23-24, 2024, p. 85., ISBN 978-83-89969-74-3
9. **Permana D.I.,** Rusirawan D., Farkas I.: Artificial neural networks analysis in experimental ORC results, Book of Abstracts, 30th Workshop on Energy and Environment, Gödöllő, Hungary, December 12-13, 2024, pp. 53-54. ISBN 978-963-623-108-8

10. ACKNOWLEDGEMENT

This thesis work was supported financially by the Stipendium Hungaricum Scholarship Program and the Mechanical Engineering Doctoral School at the Hungarian University of Agriculture and Life Sciences (MATE), Gödöllő, Hungary.

First of all, I would like to praise the Almighty God, who has granted me countless blessings and guidance during my studies.

I would like to express my deepest gratitude to my supervisors, Prof. Istvan Farkas and Dr. Dani Rusirawan, for their inestimable guidance, consistent encouragement and support. Their thoughtful suggestions and ideas were vital for the framework and outcome of this research. It has been a rewarding experience for me to work with them all these years, and without them, this thesis would not have materialized. I was indeed privileged to have been under your supervision.

I am very grateful to my only mother (Iyar Haryati) and all my sisters for their immeasurable love and sacrifices that made this feat possible.

I wish to acknowledge to my home university, Institut Teknologi Nasional Bandung, especially Department of Mechanical Engineering for supporting me during my studies.

Additionally, so many thanks for Department of Industrial Engineering, University of Florence (DIEF UNIFI) especially Prof. Maurizio De Lucia and other laboratory members that allow me to conduct experimental research there.

Finally, I would like to thank the Doctoral School of Mechanical Engineering staff and the University administration staff for their kindness and cooperation with me during my stay at the University.

Thank you for supporting and guiding me to where I am now. May the Almighty Allah and Mohammad (peace be upon him) continue to bless each and every one of you!

Gödöllő, February 2025

Diki Ismail Permana